Characterization of nanoparticles by continuous contrast variation in small-angle X-ray scattering

vorgelegt von
M.Sc.
Raul Garcia Diez
geboren in Barcelona, Spanien

Von der Fakultät II - Mathematik und Naturwissenschaften
der Technischen Universität Berlin
zur Erlangung des akademischen Grades
Doktor der Naturwissenschaften
Dr. rer. nat.

genehmigte Dissertation

Promotionsausschuss:

Vorsitzender: Prof. Dr. Norbert Esser
Gutachter: Prof. Dr. Stefan Eisebitt
Gutachterin: Prof. Dr. Simone Raoux
Gutachter: Prof. Dr. Mathias Richter

Tag der wissenschaftlichen Aussprache: 24. Mai 2017

Berlin 2017

Abstract

In the continuously growing field of nanomedicine, nanoparticles have a pre-eminent position. The particle morphology is a defining aspect of their functionality, yet most current characterization techniques possess certain limitations. This work proposes a novel approach to contrast variation in small-angle X-ray scattering based on the constitution of a solvent density gradient in a glass capillary in order to choose *in situ* the most appropriate contrast and to acquire extensive datasets in a short time interval.

By examining the scattering curves measured at different aqueous sucrose concentrations, information about the internal structure of the nanoparticles as well as their size distribution is obtained. Additionally, the particle density can be estimated from the Guinier region of the scattering curve, as is shown for polymeric colloids across a wide spectrum of polymers. These results are successfully compared with imaging methods and other techniques such as Differential Centrifugal Sedimentation.

The continuous contrast variation technique is also employed to characterize the nanodrug Caelyx, a PEGylated liposomal formulation of doxorubicin, using iodixanol as contrast agent, an iso-osmolar suspending medium. The mean size of the nanocarrier is obtained by a model-free analysis of the scattering curves based on the position of the so-called *isoscattering point*, while the traceable determination of the particle size highlights the advantages in comparison to widespread characterization techniques as Dynamic Light Scattering and Transmission Electron Microscopy.

Furthermore, the response of the nanocarrier to increasing solvent osmolality is evaluated with sucrose contrast variation and compared to the different response of PEGylated and plain liposomes to osmotic pressure depending on their size. Therefore, the osmotic pressure necessary for the liposomal shrinkage is quantitatively studied and the morphological changes induced by this deformation are thoroughly examined.

The capabilities of the continuous contrast variation method as a sizing technique are further investigated on relevant bio-materials like human lipoproteins or polymeric nanocarriers coated with antibodies. In addition, this technique is employed to determine the density of the lipoproteins, one of the most characteristic traits of these blood plasma components.

Zusammenfassung

Im kontinuierlich wachsenden Bereich der Nanomedizin haben Nanopartikel eine herausragende Stellung. Die funktionalen Eigenschaften der Nanopartikeln werden durch ihre Morphologie beeinflusst, jedoch haben die meisten gegenwärtigen Charakterisierungstechniken gewisse Einschränkungen. Die vorliegende Arbeit schlägt einen neuartigen Ansatz zur Kontrastvariation in Röntgen-Kleinwinkel-Streuung (*Small-Angle X-ray Scattering*, SAXS) auf der Grundlage des Aufbaus eines Lösungsmitteldichtegradienten in einer Glaskapillare vor, um *in situ* den geeignetsten Kontrast zu wählen und umfangreiche Datensätze innerhalb eines kurzen Zeitraums zu sammeln.

Informationen über die innere Struktur von Nanopartikeln sowie deren Größenverteilung können durch Untersuchung der Streukurven, die bei verschiedenen Konzentrationen von Zucker in Wasser gemessen werden, erhalten werden. Zusätzlich kann die Teilchendichte bestimmt werden, indem der Guinier-Bereich der Streukurven analysiert wird, was für polymere Nanopartikel über ein breites Spektrum von Teilchendichten gezeigt wird. Diese Ergebnisse wurden erfolgreich mit mikroskopischen und anderen Techniken wie Sedimentation in einem Dichtegradient (*Differential Centrifugal Sedimentation*, DCS) verglichen.

Die Technik der kontinuierlichen Kontrastvariation wurde mit dem iso-osmolaren Kontrastmittel Iodixanol auch an dem Nano-Arzneimittel Caelyx durchgeführt, einer PEGylierten liposomalen Zubereitung des Medikaments Doxorubicin. Die mittlere Größe des Nanocarriers wird durch eine modellfreie Analyse der Streukurven basierend auf der Position der sogenannten *Isoscattering-Punkte* erhalten, während die rückführbare Bestimmung der Partikelgrößen die Vorteile im Vergleich zu weit verbreiteten Charakterisierungstechniken wie dynamischer Lichtstreuung (*Dynamic Light Scattering*, DLS) und Transmissionselektronenmikroskopie (TEM) unterstreicht.

Zusätzlich wird die Reaktion des Nanocarriers auf eine zunehmende Lösungsmittel-Osmolalität mittels Zucker-Konzentrationsvariation untersucht und die unterschiedlichen Reaktionen von PEGylierten und einfachen Liposomen auf den osmotischen Druck in Abhängigkeit ihrer Größe verglichen. Dafür wird der für die liposomale Schrumpfung benötigte osmotische Druck quantitativ analysiert und die durch diese Deformation induzierten morphologischen Veränderungen sorgfältig untersucht.

Die Möglichkeiten der kontinuierlichen Kontrastvariationmethode als Technik zur Grössenbestimmung werden weiter anhand von relevanten Biomaterialien untersucht, wie menschlichen Lipoproteinen oder polymeren Nanocarriern, die mit Antikörpern beschichtet sind. Außerdem wird diese Technik verwendet, um die Dichte von Lipoproteinen zu bestimmen, eine der Haupteigenschaften dieser Blutplasmakomponenten.

Contents

1 Introduction **1**

2 Theoretical background **7**

2.1 Interaction of X-rays and matter 7

2.1.1 Beer-Lambert law 8

2.1.2 Elastic scattering 9

2.2 Small-angle X-ray scattering 12

2.2.1 Scattering by an ensemble of particles 13

2.2.2 The scattering curve 13

2.2.3 Modelling of the scattering intensity: form factors 14

2.3 Contrast variation 16

2.3.1 Isoscattering point 16

2.3.2 Basic functions approach 18

3 Instrumentation and experimental setup for SAXS measurements **21**

3.1 Synchrotron radiation 22

3.1.1 Insertion devices 23

3.2 The BESSY II electron storage ring 24

3.3 FCM beamline 25

3.3.1 UHV X-ray reflectometer 26

3.4 SAXS setup 27

3.4.1 X-ray area detector 27

3.4.2 HZB SAXS instrument and WAXS configuration 28

3.5 Sample environment 30

3.5.1 Round capillaries 30

3.5.2 Rectangular capillaries 31

3.5.3 Cell for low-energies 32

3.6 Data reduction: the scattering curve 32

4 Continuous contrast variation in SAXS: the density gradient technique **35**

4.1 Experimental procedure 36

4.1.1 Preparation of the density gradient capillaries 36

4.1.2 Calibration of the solvent density: X-ray transmission 37
4.1.3 SAXS measurements 39
4.2 Proof of principle: application to the PS-COOH particles 40
4.3 Results and data evaluation 42
4.3.1 Core-shell form factor fit 42
4.3.2 Isoscattering point 43
4.3.3 Guinier region 45
4.3.4 Consistency of the results 47
4.4 Applicability and comparison with other contrast variation approaches . . 48
4.4.1 Other possible applications of the density gradient capillary 49

5 Simultaneous size and density determination of polymeric colloids 51

5.1 Materials and methods 52
5.1.1 Polymeric particles 52
5.1.2 Differential Centrifugal Sedimentation 53
5.2 Determination of the particle size distribution 55
5.2.1 Inter-laboratory comparison of the mean particle diameter 57
5.2.2 Particle size distribution of the PS-Plain particles 59
5.3 Considerations about scattering data evaluation 60
5.3.1 Shape scattering function formalism 60
5.3.2 Isoscattering point approach 61
5.4 Determination of the particle mass density 63
5.4.1 Mass density of the PS-Plain particles: validation with DCS 64
5.4.2 Density determination of heavier polymeric colloids 65

6 Continuous contrast variation applied to relevant bio-materials 67

6.1 Materials 68
6.2 Traceable size determination of a liposomal drug 69
6.2.1 Isoscattering point approach 71
6.2.2 Shape scattering function calculation 71
6.2.3 Average electron density 72
6.3 Osmotic effects in liposomes 73
6.3.1 Application to drug-stabilized liposomes 74
6.3.2 Does PEGylation affect the osmotic activity of liposomes? 76
6.4 Sizing of blood plasma componenents 82
6.5 Protein-coated low-density nanoparticles 85
6.5.1 Hard protein corona characterization with contrast variation 86

7 Summary 89

Bibliography 93

List of Figures

1.1 Sizing techniques. 3

2.1 Depiction of the Beer-Lambert law. 8
2.2 Contributions to the X-ray attenuation coefficient of water. 9
2.3 Schematics of a scattering process and graphical definition of $\boldsymbol{q}$. 10
2.4 The scattering curve and its relevant regions. 14
2.5 Solvent contrast variation experiment and contrast matching scheme. . . . 16
2.6 Isoscattering points and particle polydispersity. 17

3.1 Scheme of the electron storage ring BESSY II. 23
3.2 Radiant power of BESSY II. 24
3.3 Diagram of the four-crystal monochromator beamline. 25
3.4 Scheme of the four-crystal monochromator. 25
3.5 Photon flux of the FCM beamline. 26
3.6 Sample-to-detector distance calibration and scattering pattern of AgBehe at large distance. 29
3.7 Homogeneity of the rectangular capillaries. 30
3.8 X-ray transmission of a rectangular capillary half-filled with water. 31
3.9 Sample environments for SAXS experiments in vacuum. 32

4.1 Scheme of the contrast variation technique in SAXS with a density gradient capillary. 37
4.2 Calibration of the solvent electron density by X-ray transmission. 38
4.3 X-ray transmittance of the density gradient capillary at different energies. 39
4.4 Experimental scattering curves of the PS-COOH particles for different suspending medium electron densities. 40
4.5 Background subtraction of the scattering curves of the PS-COOH particles. 41
4.6 Core-shell model fit to the PS-COOH particles experimental data. 42
4.7 Isoscattering points of the PS-COOH particles. 44
4.8 Deviation from the $I(0)$ used in the evaluation of the PS-COOH particles experimental data. 45
4.9 Radius of gyration of the PS-COOH particles. 46
4.10 Zero-angle intensity of the PS-COOH particles. 47
4.11 Concentration gradient of 12 nm silica particles measured at 8000 eV. . . . 50

5.1 Scheme of the differential centrifugal sedimentation setup. 53
5.2 Scattering curve of the PS-Plain particles in buffer. 55

5.3 Continuous contrast variation experimental data of the PS-Plain particles. 56
5.4 Experimental shape scattering function of the PS-Plain particles. 57
5.5 Comparison of the PS-Plain particles average diameter with different techniques. 58
5.6 Simultaneous size and density determination of the PS-Plain particles with a DCS combined approach. 58
5.7 Number-weighted size distribution of the PS-Plain particles. 59
5.8 Diameter of the PS-Plain particles obtained from the shape scattering function as a function of the number of scattering curves. 60
5.9 Deviation of the size of the PS-Plain particles obtained with $q_1^\star$ from the nominal value. 62
5.10 Zero-angle intensity of the PS-Plain particles. 63
5.11 Mass densities of three polymeric colloids measured with SAXS and DCS. 64

6.1 Cryo-TEM micrograph and schematic representation of Caelyx. 68
6.2 Continuous contrast variation experimental data of Caelyx. 70
6.3 Shape scattering function and zero-angle intensity of Caelyx. 72
6.4 Relationship between the solvent electron density and the solvent osmolality for an aqueous sucrose solution. 73
6.5 Osmotic effects of Caelyx in an aqueous sucrose density gradient. 74
6.6 Osmotic effects in the intraliposomal doxorubicin-precipitate. 75
6.7 Isoscattering point position of Caelyx with different solvents. 76
6.8 Scattering curves of the liposomes measured in buffer. 77
6.9 Schematic representation of ULVs and MLVs. 78
6.10 Scattering curves of the liposomes measured at different solvent osmolalities. 79
6.11 Isoscattering point intensity of two different liposomes. 80
6.12 Osmotic effects in the phospholipid bilayer of the liposomes. 81
6.13 Continuous contrast variation experimental data of HDL and LDL. 82
6.14 Model free-approaches to the experimental data of HDL and LDL. 83
6.15 Squared radius of the HDL scattering data. 84
6.16 Scattering curves of the PS-COOH particles coated with IgG. 85
6.17 Isoscattering point position before and after attaching IgG. 87

List of Tables

3.1 Two different SAXS experimental setups and their accessible q-range. . . . 28

4.1 Uncertainty contributions associated to the core-shell fit. 43
4.2 Uncertainty contributions associated to the isoscattering point position. . 44
4.3 Comparison of the results obtained by different evaluation approaches to contrast variation SAXS data. 48

5.1 Parameters of the different DCS setups. 54
5.2 Isoscattering points position and their corresponding particle diameter. . . 56
5.3 Comparison of the diameters obtained by different evaluation approaches. 59

6.1 Diameter of Caelyx obtained by different methods. 71
6.2 Concentration of IgG and IgG shell thickness around the PS-COOH particles. 86

Symbols

a	Crystal lattice constant
A	Atomic mass
B	Magnetic field strength
c	Speed of light in vacuum
D	Characteristic length of an object
$d\sigma/d\Omega$	Differential scattering cross-section
$d\Sigma/d\Omega$	Differential scattering cross-section per volume
$\Delta\eta$	Scattering contrast
e	Electron charge
eV	Electronvolt
E	Photon's energy
E_c	Critical energy of the bending magnet
ϵ_0	Vacuum permittivity
η	Dynamic viscosity of a fluid
f	Scattering amplitude or form factor
f_0	Scattering amplitude at the limit $\boldsymbol{q} \to 0$
f', f''	Real and imaginary part of the anomalous scattering coefficient
g	Size distribution function
h	Planck's constant
$\hbar$	Reduced Planck's constant, defined as $\hbar = h/2\pi$
I	Scattering intensity
I_s	Shape scattering function or resonant term
$k = \lvert\boldsymbol{k}\rvert$	Photons's wavenumber
K	Deflection parameter of the insertion device
K_B	Boltzmann constant
λ	Photon's wavelength
m_e	Electron mass
μ	Attenuation coefficient
n	Refractive index
N	Number of particles
N_A	Avogadro constant
p_d	Polydispersity degree
q	Momentum transfer
$q^\star$	Isoscattering point

r_e	Classical electron radius or Thomson radius
R	Radius of the particle
R_g	Radius of gyration
$\overline{R}$	Mean radius of the particle size distribution
ρ	Mass density
ρ_0	Average electron density of the particle
ρ_e	Electron density
ρ_{solv}	Electron density of the suspending medium
σ	Attenuation cross-section
σ_R	Standard deviation of the particle size distribution
T	Temperature
2θ	Scattering angle
V	Volume
$\tilde{X}$	Intensity-weighted average of the parameter X
Z	Atomic number

Abbreviations

AFM Atomic Force Microscopy

AgBehe Silver behenate ($CH_3(CH_2)_{20}COO\cdot Ag$)

BESSY Berliner Elektronenspeicherring-Gesellschaft für Synchrotronstrahlung

COOH Carboxyl group

DCS Differential Centrifugal Sedimentation

DLS Dynamic Light Scattering

DOX Doxorubicin

DSPE 1,2-Distearoyl-sn-glycero-3-phosphoethanolamine

FCM Four-crystal Monochromator

HDL High Density Lipoprotein

HSPC Hydrogenated soy phosphatidylcholine

HZB Helmholtz-Zentrum Berlin

IgG Immunoglobulin G

LDL Low Density Lipoprotein

MAA Methacrylic acid

MLV Multilamellar vesicles

MMA Methyl methacrylate

NP Nanoparticle

NPL National Physical Laboratory

OLV Oligolamellar vesicles

PEG Polyethylene glycol

PMMA Poly(methyl methacrylate)

PS Polystyrene

PTA Particle Tracking Analysis

PTB Physikalisch-Technische Bundesanstalt

SANS Small-angle Neutron Scattering

SAXS Small-angle X-ray Scattering

SEM Scanning Electron Microscopy

SI International System of Units

SPT Sodium polytungstate ($3Na_2WO_4\cdot 9W0_3\cdot H_20$)

SSL Sterically Stabilized Liposomes

TEM Transmission Electron Microscopy

TSEM Transmission Scanning Electron Microscopy

TXM Transmission X-ray Microscopy

UHV Ultra-high Vacuum

ULV Unilamellar vesicles

UV Ultraviolet light

The most exciting phrase to hear in science,
the one that heralds new discoveries,
is not "Eureka!" but "That's funny..."

ISAAC ASIMOV

1

Introduction

In 1966, Richard Fleischer directed *Fantastic Voyage*, a film about the voyage of a miniaturized submarine used to cruise along human blood vessels and repair the damage caused to the scientist's brain by a blood clot. The idea of treating damaged cells or organs from the inside fuelled the imagination of the next generation scientists and shaped the incipient field of nanomedicine. Less than 30 years later, science fiction became science fact and Doxil was approved by the US Food and Drug Administration in 1995 as the first nano-drug commercially available (Barenholz, 2012). Although 20 years after this milestone nano-submarines are still a long way off, nanomedicine is a well-established research field and dozens of products are under clinical trials or have been approved by the relevant health agencies (Etheridge *et al.*, 2013).

The origins of the nanomedicine breakthrough can be found in the tremendous progress in nanoparticles research observed in the 60s and 70s of the last century. Nanoparticles (NPs) are objects with *one or more external dimensions in the size range from 1 nm to 100 nm* (European Commission Recommendation for nanomaterial (2011/696/EU)) and have a pre-eminent position in the continuously growing world of nanotechnology, employed as paints or cosmetic products (Guterres *et al.*, 2007). Besides, the application of NPs in the emerging field of nanomedicine opens up exciting prospects (Sahoo & Labhasetwar, 2003; Wickline & Lanza, 2003; Rosen & Abribat, 2005; Nie *et al.*, 2007; Zhou *et al.*, 2014), especially considering their possibilities as platforms for drug-delivery (Wang *et al.*, 2012) or encapsulating imaging agents (Tao *et al.*, 2011).

The development of NPs is currently focused towards tailoring nano-drug carriers with flexible surface functionalizations and controlled morphologies (Euliss *et al.*, 2006; Petros & DeSimone, 2010; Nicolas *et al.*, 2013). The morphology of NPs is typically specified by parameters like size, shape, density or chemical composition of the particle, which are fundamental and defining aspects of the particle functions and determine their suitability in real-world medical applications (Vittaz *et al.*, 1996; Canelas *et al.*, 2009). In this regard, the size of NPs is one of the most crucial physicochemical properties of nano-drugs, because it determines whether they can intrude into the biological cells or the targeted tumor sites. An accurate and reliable description of the morphological traits of the NPs is therefore of vital importance for their favourable translation into successful nanomaterials.

The term *nanometrology* refers to the science of accurate and correct measurement of relevant properties at the nanometre range. A central concept in metrology is *traceability*, which refers to the ability of relating the measured value i.e. measurand to a base unit definition of the International System of Units (SI system) by an unbroken chain of comparisons with known uncertainties. This allows an objective comparison of the results obtained by different methods based on a consistent uncertainty budget associated to the measurand. The fundamental research in the field of metrology in Germany is addressed by its national metrology institute, the Physikalisch-Technische Bundesanstalt (PTB). Founded in 1887, the PTB is devoted among other metrological activities to the new definition of units based on natural constants or the technology transfer with the industry.

At the nanoscale level, PTB is involved in the development of the dimensional nanometrology field, which studies the measurement of the physical size or distances of a given nanomaterial and traces it back to the unit *metre*. There are several available techniques which are suitable for the sizing of NPs, though not all provide a traceable measurement. A prime example is dynamic light scattering (DLS), the most widely used tool in nanomedicine (Murphy, 1997; Hallett *et al.*, 1991; Egelhaaf *et al.*, 1996; Takahashi *et al.*, 2008; Jans *et al.*, 2009; Hoo *et al.*, 2008). DLS is well-established and has indisputable advantages in the size characterization of the NPs, e.g. easy-to-use instrumentation, fast and low-cost operation, but it is not capable of a traceable size determination as there is no general relationship between the measured hydrodynamic diameter and the physical size of the NPs (Meli *et al.*, 2012).

Other ensemble techniques extensively used are differential centrifugal sedimentation (DCS) (Fielding *et al.*, 2012) and Particle Tracking Analysis (PTA), both capable of measuring the NPs in suspension. While DCS is based on the sedimentation of NPs through a density gradient, PTA is a single-particle counting method that relates the Brownian movement of the particles with the measured laser light scattering. The particle size distribution obtained with DCS is calibrated with a reference material of known size and density and requires of precise information about the NPs density for the calculation, resulting in a measurement that is hardly traceable to SI units. Similarly to DLS, the PTA measurand derives from the hydrodynamic properties of the NPs (Varga *et al.*, 2014*b*).

Microscopic tools are also frequently used for structural investigations (Joensson *et al.*, 1991; Silverstein *et al.*, 1989), and have proved to be useful techniques for solid NPs due to their SI traceability achieved by coupling the measurement table with a laser interferometer (Meli *et al.*, 2012). Nevertheless, techniques such as transmission electron microscopy (TEM), transmission scanning electron microscopy (TSEM), transmission X-ray microscopy (TXM) or atomic force microscopy (AFM) are not ensemble averaged and the statistical accuracy of non-ensemble methods is often not sufficient. Besides, the removal of the original suspending medium can be considered another drawback, as well as the possible distortion of the particle morphology during the drying process, though it can be partially overcome by cryo-TEM (Li *et al.*, 1998). A schematic representation of the available measuring range of different sizing techniques is depicted in figure 1.1.

The nanoparticles envisioned for medical use are typically in the soft matter regime and thus the characterization tools must be carefully chosen considering the measurement limitations. For example, liposomes and biodegradable NPs, e.g. polymeric colloids, are finding many medical applications, especially as drug-carriers (Kattan *et al.*, 1992; Vicent & Duncan, 2006) and are starting to undergo clinical trials (Patel *et al.*, 2012; Beija *et al.*, 2012; Cabral & Kataoka, 2014). However, the size determination of polymeric NPs with a well-known technique like AFM is rather challenging due to their elastic properties (Wu

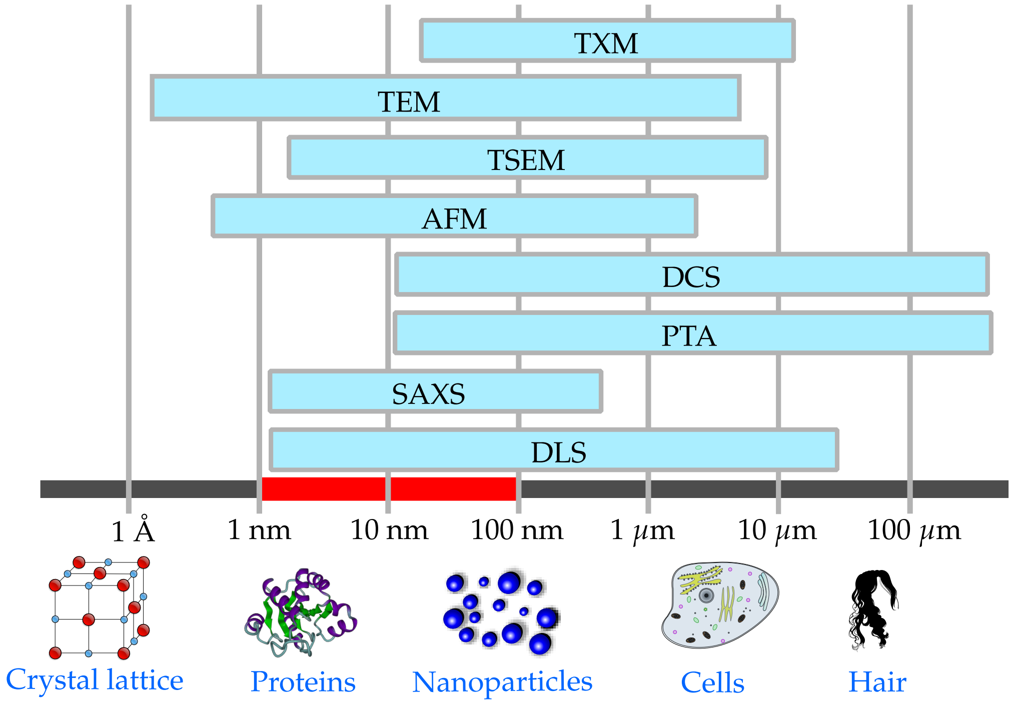

Figure 1.1 | Some available sizing techniques for nanoparticles and their measuring size range.

et al., 2014) and suggests alternative approaches.

Liposomes are spherical vesicles composed of a closed phospholipid bilayer membrane capable of encapsulating hydrophilic compounds. The importance of lipid vesicles in the progress of nanomedicine is indisputable, as the first approved nano-drug is a liposomal formulation of doxorubicin, Doxil® (Caelyx® in Europe). Nowadays, liposomes continue to be a widespread instrument for drug delivery (Pérez-Herrero & Fernández-Medarde, 2015), but their complicated internal structure requires typically more than a single characterization tool (Khorasani *et al.*, 2014). Likewise, relevant biological structures in nanomedicine possess heterogeneous morphologies which are rather difficult to detect with imaging techniques (Baumstark *et al.*, 1990; Varga *et al.*, 2010). For instance, electron microscopy is an effective tool for direct observation of the shape and size distribution of nanoparticles, but it cannot conclusively elucidate their inner composition.

The use of an ensemble-averaged and non-destructive technique such as small-angle X-ray scattering (SAXS) is revealed as an appropriate alternative (Leonard Jr *et al.*, 1952; Motzkus, 1959). This technique can discern electron density differences in the structure of NPs and offers advantages over other methods which require prior treatment of the sample and are not averaging. SAXS is based on the elastic scattering of X-ray photons by the electron density distribution of an object and is traceable down to the SI unit m for the size determination of sufficiently monodisperse NPs (Meli *et al.*, 2012). The traceability of SAXS arises from the precise determination of the oscillation period on the momentum transfer axis, which is calibrated using SI traceable values of the X-ray wavelength and the scattering angle (Krumrey *et al.*, 2011).

The first SAXS phenomena were observed in the 1930s by P. Krishnamurti and B.E. Warren (Krishnamurti, 1930*a*,*b*; Warren, 1934) while investigating colloidal suspensions and carbon black systems. The instrumental advances introduced by Kratky (1938) and Guinier (1937) sparked interest in the technique, while the seminal work of Guinier (1939) paved the way for the development of a SAXS theoretical background by scientists like Kratky, P. Debye or G. Porod (Kratky & Sekora, 1943; Debye & Bueche, 1949; Kratky & Porod, 1949; Guinier, 1950; Guinier & Fournet, 1955). Stuhrmann's new approach to the understanding of the scattered intensity (Stuhrmann & Kirste, 1965) and the appearance of dedicated synchrotron radiation sources stimulated the scientific community to employ SAXS as a characterization tool. Since then, SAXS has been extensively employed in the characterization of polymeric colloids (Dingenouts *et al.*, 1999; Chu & Hsiao, 2001; Ballauff, 2011) and its use in liposome research is also ubiquitous. For instance, it has been applied to characterize the lamellarity, bilayer thickness, area per lipid ratio (Pabst *et al.*, 2010; Bouwstra *et al.*, 1993; Brzustowicz & Brunger, 2005) and the thickness of the PEG-layer of different liposomal samples (Varga *et al.*, 2010, 2012), as well as to describe the influence of extrusion on the average number of bilayers (Jousma *et al.*, 1987) and to determine the electron density profile of liposomes (Bouwstra *et al.*, 1993; Brzustowicz & Brunger, 2005; Hirai *et al.*, 2003) and biological vesicles (Castorph *et al.*, 2010).

Despite being a highly informative method for the accurate characterization of NPs, the interpretation of the scattering curves in the reciprocal space, i.e. the uniqueness of the solution of the model fitting, is frequently intricate for complex samples (Mykhaylyk, 2012) and can affect the traceability of SAXS to SI units or increase the uncertainty associated to the result. This demands either the application of model-free approaches to the scattering data analysis or the acquisition of complementary experimental information. The solvent contrast variation approach is a noteworthy candidate due to the complementary data that can be collected at each independent contrast and the availability of extended data evaluation possibilities.

The contrast variation method in SAXS varies systematically the electron density of the suspending medium by adding a suitable contrast agent, e.g. sucrose, in order to resolve the different contributions of the particle components to the scattering. By measuring SAXS patterns as a function of the adjusted contrast, a more detailed insight into the particle morphology can be obtained in comparison to single-contrast experiments (Bolze *et al.*, 2004). For instance, the internal structure can be modelled in terms of the radial electron density (Dingenouts *et al.*, 1994*b*, 1999; Ballauff, 2011; Ballauff *et al.*, 1996) and the individual contribution of each component can be distinguished (Beyer *et al.*, 1990; Grunder *et al.*, 1991, 1993; Ottewill *et al.*, 1995; Bolze *et al.*, 1997; Dingenouts *et al.*, 1994*c*) as well as its density (Mykhaylyk *et al.*, 2007). Additionally, model-free approaches like the isoscattering point position (Kawaguchi & Hamanaka, 1992) can be applied to the evaluation of the contrast variation data sets.

This work was performed in the PTB laboratory at the electron storage ring BESSY II and proposes a novel approach to solvent contrast variation in SAXS, based on the formation of a solvent density gradient within a capillary which enables the acquisition of SAXS patterns at a continuous range of contrasts, and, as a result, collect an extensive data set of complementary scattering curves in a relatively short timespan. This original strategy averts the most problematic issues of the classic solvent contrast variation technique, namely the discrete range of available solvent electron densities and the prolonged time required for the preparation of the complementary samples and for obtaining the experimental data. Besides, the possibility to choose during the experiment the most appropriate contrast within the available range allows to tune *in situ* the performance of the contrast variation technique in SAXS without any *a priori* knowledge of the investigated nanoparticles.

The structure of this thesis builds organically around the main concept presented in this work, i.e. the contrast variation technique in SAXS by means of a solvent density gradient capillary. Following this introduction, chapter 2 is dedicated to describe the theoretical framework required to understand the contrast variation method in small-angle X-ray scattering. The instrumentation employed to obtain the experimental results presented in this thesis is thoroughly described in chapter 3. These two chapters serve as the necessary building blocks for the development of the continuous contrast variation method based on the idea of a density gradient column. The detailed review of its performance is presented in chapter 4, where the technique is used to characterize low-density nanoparticles. The metrological possibilities of the newly introduced method are further evaluated in chapter 5, mainly focusing on its ability to determine the size and density of polymeric NPs in a traceable way. Finally, the scope of the technique is investigated in chapter 6 by using the continuous contrast variation method in a myriad of relevant nanomaterials related to nanomedicine or human biology. The final chapter 7 summarizes the results presented in this thesis while adding some conclusive remarks. Extensive parts of the work presented in chapters 4 to 6 have been published in peer-reviewed journals (Minelli *et al.*, 2014; Garcia-Diez *et al.*, 2015, 2016*a*,*b*).

2

Theoretical background

In this chapter, the basic physical principles underlying the operation of small-angle X-ray scattering are presented, focusing principally on the interaction between X-rays and matter and the elastic scattering of X-rays by an ensemble of electrons. The fundamental theoretical background of SAXS is also introduced, jointly with the analytical expressions of the form factors used in this work. An entire section is devoted to the theoretical framework used in contrast variation experiments in SAXS, where concepts such as the isoscattering point and the basic functions approach are introduced.

2.1 Interaction of X-rays and matter

X-rays are electromagnetic waves which propagate in vacuum along the direction of the wavevector $\boldsymbol{k}$. The incident X-ray radiation can be described by the wave function of a monochromatic plane wave:

$$\Psi_0\left(\boldsymbol{r}\right) = A_0 e^{i\boldsymbol{k}\boldsymbol{r}} \tag{2.1}$$

where the wavenumber $k = |\boldsymbol{k}|$ is related to the X-ray wavelength λ by $k = {}^{2\pi}/_{\lambda}$. Conventionally, X-ray wavelengths range between 0.01 and a few nanometres, although SAXS experiments are conducted normally at the hard X-ray range, e.g. at wavelenghts between 0.02 and 0.8 nm. Due to the wave-particle duality of electromagnetic radiation, X-rays possess a particle nature as well, represented by the quantization of light into an ensemble of photons with an energy $\hbar\omega$. The photon energy is related to the X-ray wavelength by (Als-Nielsen & McMorrow, 2011)

$$\lambda = \frac{hc}{E_{ph}} \tag{2.2}$$

where h is the Planck's constant and c is the speed of light in vacuum. The photon energies employed typically in SAXS experiments stretch between the silicon K-edge at 1.7 keV and some dozens of keV, including the classic copper K_{α} emission line at 8 keV.

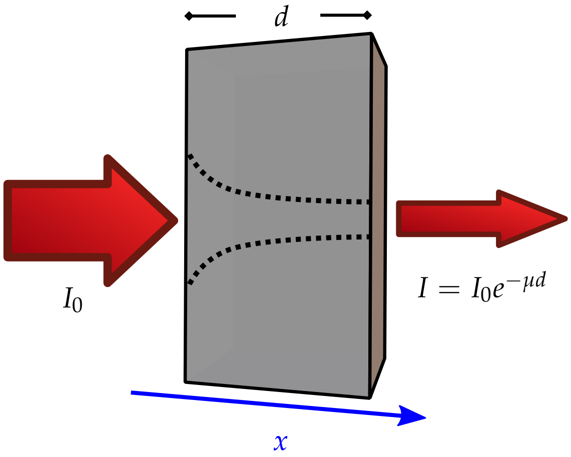

Figure 2.1 | The Beer-Lambert law is schematically depicted: The attenuation of X-rays through a medium of thickness d and attenuation coefficient μ behaves accordingly to the expression 2.3.

2.1.1 Beer-Lambert law

The interaction of X-ray photons and matter produce an attenuation of the incident radiation intensity I_0 which is related to the properties and volume of the material. The decrease of the intensity through a medium is schematically depicted in figure 2.1 and described by the Beer-Lambert law (Als-Nielsen & McMorrow, 2011):

$$I\left(x\right) = I_0 e^{-\mu x} \tag{2.3}$$

where μ is the linear attenuation coefficient and x is the radiation path length. The attenuation coefficient is dependent on the material composition and the photon energy and is directly related to the extinction coefficient β, e.g. the imaginary part of the refraction index n, by (Marr, 1987)

$$\mu(E) = \frac{4\pi}{hc} E\beta(E) \tag{2.4}$$

Considering that the refractive index is expressed generally by $n = 1 - \delta + i\beta$ and $\delta < 10^{-3}$ in the X-ray regime (Henke *et al.*, 1993), refraction effects can be neglected in scattering experiments because $\Re(n)$ is very close but smaller than unity.

When the attenuating medium is composed of different atomic species, μ can be expressed as the summation of each component attenuation coefficient μ_i:

$$\mu = \sum_i \mu^i = \sum_i \rho_e^i \sigma^i = N_A \sum_i \frac{Z^i}{A^i} \rho^i \sigma^i \tag{2.5}$$

where N_A is the Avogadro constant, σ is the attenuation cross-section and ρ_e is the number density of absorbing centres. The cross-section σ is defined as the effective area in which photon-matter events occur. In the X-ray regime, photons interact principally with the atomic electrons, thus ρ_e is the electron density and is directly proportional to the atomic number Z, the atomic mass number A and the mass density ρ of the component i.

In fact, the attenuation cross-section σ is dependent upon the several different mechanisms in which a X-ray photon interacts with the atomic electrons. The 3 most relevant effects are the photoelectron absorption, the coherent scattering and the incoherent scattering, which sum up to the total attenuation coefficient:

$$\mu = \rho_e(\tau_{\text{abs}} + \sigma_{\text{scat, coh}} + \sigma_{\text{scat, incoh}}) \tag{2.6}$$

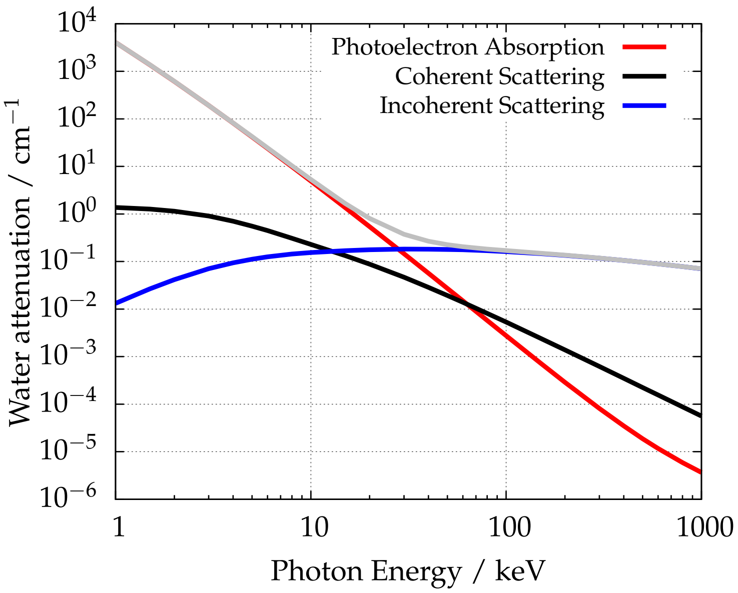

Figure 2.2 | The different contributions to the attenuation of water at room temperature are depicted as a function of the photon energy (Henke *et al.*, 1993) and the total attenuation is the summation of all the other contributions. The pair production in nuclear and electron field can be neglected at the displayed photon energies.

When the X-ray photon is completely absorbed by the atom, the event is called photoelectron absorption because a photoelectron with the excess energy is expelled from an inner atomic shell, leaving the atom ionized. The created core-hole is consequently filled by an electron from an outer shell either by a radiative process, i.e. *fluorescence*, or by a non-radiative mechanism emitting a secondary electron, i.e. *Auger effect*. The photoelectric effect is the predominant contribution to the attenuation cross-section principally at low X-ray energies and the ultraviolet regime, as shown in figure 2.2.

The other relevant contributions in the X-ray range are related to scattering processes. In an inelastic scattering event, the energy of the incident photon is partially transfered to a loosely bound electron resulting in a scattered photon with a longer wavelength, according to the Compton relation $\Delta\lambda = {}^{h}/_{m_e c}\,(1 - \cos 2\theta)$ (Als-Nielsen & McMorrow, 2011), where 2θ is the scattering angle. The Compton scattering is incoherent and contributes generally less than the elastic scattering at energies below 10 keV, as observed in figure 2.2. Besides, the coherent scattering signal is the summation of the constructive interferences of the electromagnetic wave, which produces a higher scattering intensity than the inelastic scattering. In fact, the elastic scattering of X-rays, typically coherent, is the main process used in material investigations and the physical principle behind SAXS.

2.1.2 Elastic scattering

When the wavelength of the scattered wave is the same than that of the incident one, the proccess is named elastic scattering or coherent scattering and the resulting intensity is the absolute square of the sum of the scattering amplitudes. In the following sections, the elastic scattering theory will be presented for the classical case and for an ensemble of electrons.

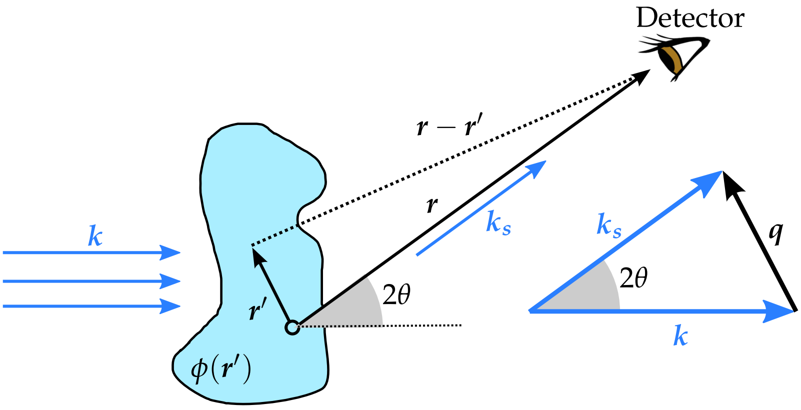

Figure 2.3 | Scheme of an scattering event by an object with a potential function $\phi(\boldsymbol{r}')$ at a distance $|\boldsymbol{r}| = r$. A geometrical definition of the momentum transfer vector $\boldsymbol{q}$ is depicted on the right hand side, where $\boldsymbol{k}$ and $\boldsymbol{k}_s$ are the incident and scattered wavevector respectively.

Thomson scattering

Classically, the elastic scattering of a photon by a free electron is described by the conservation of the photon energy, i.e. the wavenumber of the scattered wave is the same than the incident one ($|\boldsymbol{k}_s| = |\boldsymbol{k}|$). Consequently for unpolarized incident radiation, the intensity of the scattered wave at a distance r and with a scattering angle 2θ is defined by (Warren, 1969):

$$I_{\text{scat}}(r,\theta) = I_0 \left(\frac{r_e}{r}\right)^2 \left(\frac{1+\cos^2 2\theta}{2}\right) \tag{2.7}$$

where $r_e = e^2/4\pi\epsilon_0 m_e c^2 = 2.82 \cdot 10^{-15}$ m is the Thomson or classical electron radius. A relevant quantity in scattering processes is the differential scattering cross-section $d\sigma/d\Omega$, which is directly proportional to the scattering intensity I_{scat}. It is defined as the the number of scattered photons per time and per solid angle over the incident intensity per time and per area (Als-Nielsen & McMorrow, 2011):

$$\frac{d\sigma}{d\Omega} = \frac{I_{\text{scat}} \cdot \left(r^2 \Delta\Omega\right)}{I_0 \Delta\Omega} = r_e^2 \left(\frac{1+\cos^2 2\theta}{2}\right) \tag{2.8}$$

where $r^2\Delta\Omega$ is the detector surface in the plane of the impact parameter. The total Thomson scattering cross-section is $\sigma = 8\pi r_0^2/3 = 0.665 \cdot 10^{-24}$ cm^2 and similarly to $d\sigma/d\Omega$ is proportional to r_e^2 and independent from the photon energy if the photon wavelength is distant of an X-ray absorption edge.

Scattering by an ensemble of electrons

The scattering of a photon by an ensemble of weakly bound electrons can be studied by considering the interaction of particles with a three-dimensional weak potential $V(\boldsymbol{r}) = V_0 \cdot \phi(\boldsymbol{r})$, where V_0 is the strength of the potential and $\phi(\boldsymbol{r})$ is the so-called *potential function*. The resulting wave can be expressed as a linear combination of the incident plane wave (see equation 2.1) and the scattered spherical wave at the position $\boldsymbol{r}$:

$$\Psi(\boldsymbol{r}) = \Psi_0(\boldsymbol{r}) + \Psi_{\text{scat}}(\boldsymbol{r}) \tag{2.9}$$

Inserting this expression at the time-independent Schrödinger equation and considering the scattering wave as a perturbation produced by the scattering potential function $\phi(\boldsymbol{r})$ (Cowley, 1995), it can be derived that

$$\Psi_{\text{scat}}\left(\boldsymbol{r}\right) = C\int \frac{e^{ik\left|\boldsymbol{r}-\boldsymbol{r}'\right|}}{\left|\boldsymbol{r}-\boldsymbol{r}'\right|}\phi(\boldsymbol{r}')\Psi\left(\boldsymbol{r}'\right)d\boldsymbol{r}'^{3} \tag{2.10}$$

where C is the so-called *scattering length.* If the detection position $\boldsymbol{r}$ is at distance much larger than the scattering object size, as outlined in figure 2.3, the Fraunhofer approximation applies and $\left|\boldsymbol{r}-\boldsymbol{r}'\right| \simeq r$ (Feigin & Svergun, 1987), resulting in

$$\Psi_{\text{scat}}\left(\boldsymbol{r}\right) = C\frac{e^{ikr}}{r}\int e^{-ikr'}\phi(\boldsymbol{r}')\Psi\left(\boldsymbol{r}'\right)d\boldsymbol{r}'^{3} \tag{2.11}$$

Assuming that there are no multiple scattering events due to the low concentration of scatterers and that the interaction potential is weak, the first Born approximation can be employed ($\Psi\left(\boldsymbol{r}\right) \simeq \Psi_0\left(\boldsymbol{r}\right)$) (Cowley, 1995), leading to

$$\Psi_{\text{scat}}\left(\boldsymbol{r}\right) = CA_0\frac{e^{ikr}}{r}\int e^{iqr'}\phi(\boldsymbol{r}')d\boldsymbol{r}'^{3} \tag{2.12}$$

where $\boldsymbol{q} = \boldsymbol{k_s} - \boldsymbol{k}$ is the momentum transfer vector and $\boldsymbol{k_s}$ the scattered wavevector. Analogously to equation 2.8, the differential scattering cross-section is:

$$\frac{d\sigma}{d\Omega} = \frac{\left|\Psi_{\text{scat}}\right|^2\cdot\left(r^2\Delta\Omega\right)}{\left|\Psi_0\right|^2\Delta\Omega} = r_e^2\left|f(\boldsymbol{q})\right|^2 = r_e^2\,I(\boldsymbol{q}) \tag{2.13}$$

where $f(\boldsymbol{q}) = \int e^{iqr'}\phi(\boldsymbol{r}')d\boldsymbol{r}'^{3}$ is the scattering amplitude, $I(\boldsymbol{q}) = \left|f(\boldsymbol{q})\right|^2$ is the scattering intensity and the scattering length is the classical electron radius r_e. The scattering amplitude $f(\boldsymbol{q})$ is simply the Fourier transform of the scattering potential function $\phi(\boldsymbol{r})$.

This type of scattering mechanism is named Rayleigh-Gans-Debye when the refractive index of the object n_{obj} is close to unity and the condition $2\pi/\lambda \cdot D \cdot \left|n_{\text{med}} - n_{\text{obj}}\right| \ll 1$ is fulfilled, being D the size of the object and n_{med} the refractive index of the suspending medium. For X-ray photons with wavelenghts λ around 0.1 nm and nanoscaled objects, this approximation can be applied and it can be safely assumed that the same electromagnetic wave impinges each part of the object (van de Hulst, 1957; Barber & Wang, 1978). In the case of optical radiation scattered by colloids, the Mie scattering framework is used, while the Rayleigh scattering corresponds to light wavelengths much larger than the scattering object.

Anomalous scattering

In X-ray scattering experiments, the scattering centres are the electrons of the atom and the scattering potential function is the electron charge density about the nucleous, so $\phi(\boldsymbol{r}) = \rho_e(\boldsymbol{r})$. The electron density is related to the atomic properties as introduced in equation 2.5 and therefore the scattering amplitude increases with the atomic number Z as can be shown by calculating equation 2.13 at the limit $\boldsymbol{q} \to 0$

$$f(\boldsymbol{q} \to 0) = \int \rho_e(\boldsymbol{r}')d\boldsymbol{r}'^{3} = Z \tag{2.14}$$

This is valid when the incident photon energy is much larger than the energy corresponding to a resonant excitation. When the X-ray energy is close to an absorption edge, the anomalous dispersion becomes relevant and the scattering amplitude depends on the energy of the X-ray by adding the anomalous corrections (Als-Nielsen & McMorrow, 2011):

$$f(E) = f_0 + f'(E) + if''(E) \tag{2.15}$$

where the imaginary part f'' is related to the attenuation coefficient μ by (Feigin & Svergun, 1987)

$$f''(E) = \frac{A\rho}{2N_A r_e hc} E\mu(E) \tag{2.16}$$

where A is the atomic mass of the resonant atom and ρ its mass density. The term f' is related to the imaginary anomalous coefficient by the Kramers-Kronig relationship (de L. Kronig, 1926; Kramers, 1927):

$$f'(E) = \frac{2}{\pi} \int_0^\infty \frac{E' f''(E') dE'}{E^2 - E'^2} \tag{2.17}$$

The values of the anomalous scattering amplitude $f(E)$ are usually calculated using the experimentally measured attenuation coefficient $\mu(E)$.

2.2 Small-angle X-ray scattering

Small-angle X-ray scattering is a powerful technique that can elucidate the structural features of particles with sizes ranging from a few nanometres up to some hundreds of nanometres. By investigating the photons elastically scattered by the electron density distribution of the particle $\rho_e(\boldsymbol{r})$, the resulting patterns can be analysed employing equation 2.13 to obtain information about the particle size, shape and composition. Two fundamental quantities in a SAXS experiment are the scattering intensity $I(\boldsymbol{q})$, proportional to $d\sigma/d\Omega$, and the scattering amplitude or *form factor* $f(\boldsymbol{q})$. The latter is expressed for objects with spherical symmetry where $\rho_e(\boldsymbol{r}) = \rho_e(r)$ by

$$f(q) = 4\pi \int_0^\infty r'^2 \rho_e(r') \frac{\sin(qr')}{qr'} dr' \tag{2.18}$$

where the modulus of the momentum transfer vector is defined by $q = |\boldsymbol{q}| = |\boldsymbol{k}_s - \boldsymbol{k}|$. Considering that SAXS is an elastic scattering process ($|\boldsymbol{k}_s| = |\boldsymbol{k}| = 2\pi/\lambda$), the momentum transfer is expressed as

$$q = \frac{4\pi}{\lambda} \sin\theta = \frac{4\pi E}{hc} \sin\theta, \tag{2.19}$$

where θ is half of the scattering angle as depicted in figure 2.3, h is the Planck constant and c is the speed of light.

The systems studied by SAXS in this work consist of particles suspended in a uniform medium, e.g. water or buffer, with a different electron density ρ_{medium} than the studied particle. In fact, the measured scattering amplitude is the addition of the medium and the particle contributions. Therefore, the scattering of the studied object is expressed in terms of the *contrast*, $\Delta\eta(\boldsymbol{r}) = \rho_e(\boldsymbol{r}) - \rho_{\text{medium}}$, the electron density difference between the particle and the embedded matrix or surrounding medium. This leads to a slight modification of equation 2.18, where $\rho_e(r)$ can be substituted by the contrast $\Delta\eta(r)$ to distinguish the contribution of the investigated particle from that of the medium.

2.2.1 Scattering by an ensemble of particles

For diluted systems with low particle concentration, the wave scattered by a particle does not interfere coherently with the neighboring particles, hence the scattering intensity can be expressed as a sum of the scattering of the individual particles, i.e. the structure factor contribution can be neglected because $S(q) = 1$ (Feigin & Svergun, 1987). Assuming this premise, the scattering intensity of an ensemble of randomly oriented spherically symmetric nanoparticles in a diluted suspension can be expressed as

$$I(q) = N \int_0^\infty g(R) \left|f(q,R)\right|^2 dR, \tag{2.20}$$

where N is the number of scatterers i.e particles, $g(R)$ is their size distribution function and $f(q,R)$ is the particle form factor, which depends on the radial structure of the particle as determined in equation 2.18. Generally, the particles in suspension are not monodisperse and show a certain size distribution which is often related with their chemical preparation. For systems of relatively low size polydispersity, a gaussian size distribution is typically a good choice, which is expressed by:

$$g_{\text{Gauss}}(R) = \frac{1}{\sigma_R\sqrt{2\pi}} e^{-\frac{\left(R-\overline{R}\right)^2}{2\sigma_R^2}} \tag{2.21}$$

where $\overline{R}$ is the mean radius of the particles and σ_R is the standard deviation of the size distribution. For smaller particles or higher polydispersity degrees, a log-normal distribution is preferred, defined as

$$g_{\text{LN}}(R) = \frac{1}{R\sigma_R\sqrt{2\pi}} e^{-\frac{\left(\ln(R)-\ln(\overline{R})\right)^2}{2\sigma_R^2}} \tag{2.22}$$

whose mean radius is given by $\overline{R}e^{\frac{\sigma_R^2}{2}}$ and the variance is $\overline{R}^2 e^{\sigma_R^2}(e^{\sigma_R^2} - 1)$. Other approaches to the size distribution of particles in solution are based in numerical techniques, like the Monte-Carlo approach to form-free particle size distributions (Pauw *et al.*, 2013).

A useful parameter for comparative purposes between samples is the polydispersity degree p_d, which is defined as the full width at half maximum (FWHM) of the number-weighted particle size distribution divided by its average value. For a normal size distribution, the FWHM is simply $2\sqrt{2\ln 2}$ times its standard deviation σ_R.

2.2.2 The scattering curve

The differential scattering cross-section $d\sigma/d\Omega$ is the fundamental measurand in a SAXS experiment, as described in section 2.1.2. Nevertheless, some comparability challenges arise from this quantity as it depends on the sample volume V used in the experiment. This can be solved by introducing the differential scattering cross-section per volume, historically given in cm^{-1}. The expression of this quantity is derived from equations 2.13 and 2.20 and leads to:

$$\frac{d\Sigma}{d\Omega}(q) = \frac{d\sigma/d\Omega(q)}{V} = \frac{r_e^2\, I(q)}{V} = r_e^2 \cdot \frac{N}{V} \cdot \int_0^\infty g(R)\left|f(q,R)\right|^2 dR \tag{2.23}$$

where N/V is the concentration of scatterers, i.e. particles.

For isotropically scattering samples, the scattering patterns consist of concentric rings, as shown in figure 2.4a. By azimuthally averaging the scattering pattern, the data is reduced

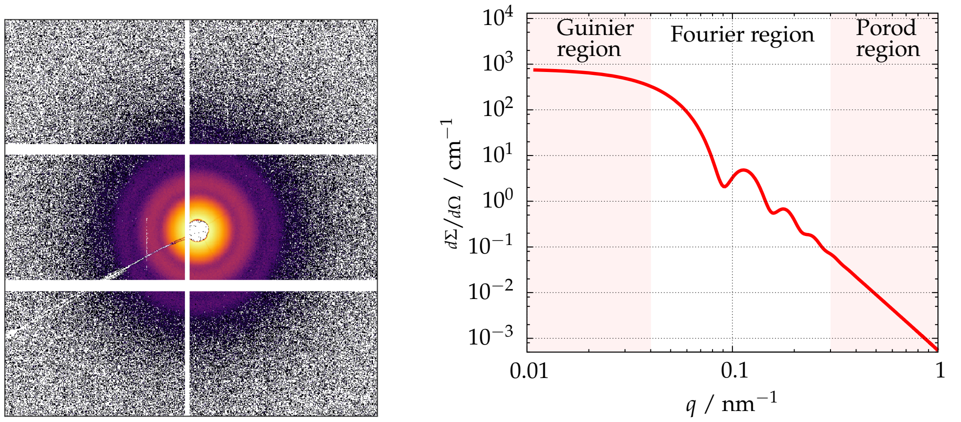

(a) The scattering pattern **(b)** The scattering curve and its relevant regions

Figure 2.4 | a) Radially symmetric scattering pattern of a nanoparticle ensemble in suspension with radius 50 nm and a polydispersity degree of 25 %. b) The scattering curve is the azimuthal integration of the 2D image. The three different regions of the scattering curve discussed in the text are highlighted in the figure as well.

from 2D images to 1D scattering curves. The scattering curve is the typical form to present the experimental data, which displays the differential scattering cross-section per volume $d\Sigma/d\Omega$ versus the momentum transfer q in a log–log graph as depicted in figure 2.4b for an ensemble of spherical particles with radius 50 nm and polydispersity degree 25 %. Three different regions can be distinguished in a scattering curve (Schnablegger & Singh, 2006):

- The **Guinier region** comprises the low-q region where $qD < 1.3$ (Feigin & Svergun, 1987), being D the characteristic length of the investigated object. This region provides principally information about the size of the particle.

- The high-q region is called the **Porod region**, where information about the surface-to-volume ratio of the particles can be derived. For a smooth particle surface, the scattering intensity decays as q^{-4}, while for rough or fractal surfaces the slope is a function of q^{-b} with $2 < b < 4$ (Glatter & Kratky, 1982).

- For sufficiently monodisperse particle suspensions, the **Fourier region** or middle-q region of the scattering curve shows pronounced minima that characterize the particle structure, size and shape.

2.2.3 Modelling of the scattering intensity: form factors

Besides the information obtained about the size distribution of the particle ensemble, the scattering intensity $I(q)$ provides information about the shape and composition of the particles, accessible by modelling the form factor. In the simple case of a solid sphere with uniform density ρ_0, the radial electron density profile is described by $\rho_e(r > R) = 0$ and $\rho_e(r < R) = \rho_0$, whilst the integral of expression 2.18 is limited only to the radius of the particle R. The form factor of a homogeneous solid sphere is

$$f_{\text{sph}}(q,R) = \frac{4}{3}\pi R^3 \left(\rho_0 - \rho_{\text{medium}}\right) \left(3\frac{\sin(qR) - qR\cos(qR)}{(qR)^3}\right) = \Delta\eta \cdot F_{\text{sph}}(q,R) \quad (2.24)$$

where $\Delta\eta = \rho_0 - \rho_{\text{medium}}$ is the contrast and $F_{\text{sph}}(q, R)$ is defined for convenience. When the shape of the particle deviates from a sphere, the assumptions made in equation 2.18 are not applicable and the scattering intensity must be integrated over all available angles numerically. For a homogeneous ellipsoid of revolution with two equal semi-axes of length R and a semi-principal axis of length νR, the square of the form factor is expressed as:

$$\left|f_{\text{ellip}}(q, R)\right|^2 = \Delta\eta^2 \int_0^1 \left|F_{\text{sph}}\left(q, R\sqrt{u^2\left(\nu^2 - 1\right) + 1}\right)\right|^2 du \tag{2.25}$$

where ν is the ellipticity, $u = \cos\alpha$ and $\alpha \in [0, \pi/2]$. If $\nu > 1$, the expression defines a prolate spheroid, whilst $\nu < 1$ defines an oblate spheroid.

Frequently, nanoparticles show an internal heterogeneity, leading to an inner electron density distribution. If the components are radially distinguishable, the form factor corresponding to a morphology defined by sharp interfaces between the radial symmetric components of the particle with radius R_i is

$$f\left(q, R\right) = \Delta\eta F_{\text{sph}}(q, R) + \sum_{i=1}^{n-1} \Delta\rho_i \left(F_{\text{sph}}(q, R_{i+1}) - F_{\text{sph}}(q, R_i)\right), \tag{2.26}$$

where R is the external radius of the particle and n is the number of concentric shells. The excess of electron density of each component is $\Delta\rho_i = \rho_i - \rho_{\text{core}}$ and the contrast is defined in this case as $\Delta\eta = \rho_{\text{core}} - \rho_{\text{medium}}$ in order to isolate the electron density of the surrounding medium in one term.

The simplest case of expression 2.26 arises for core-shell particles in suspension. This model represents a radially symmetric particle with a sharp interface between the outer shell and the inner core. The form factor is described by

$$f_{\text{CS}}(q, R) = \Delta\eta F_{\text{sph}}(q, R) + \Delta\rho\left(F_{\text{sph}}(q, R) - F_{\text{sph}}(q, R_{\text{core}})\right), \tag{2.27}$$

where R and R_{core} are the outer shell and inner core radii respectively, the excess of electron density is $\Delta\rho = \rho_{\text{shell}} - \rho_{\text{core}}$ and the contrast is expressed as $\Delta\eta = \rho_{\text{core}} - \rho_{\text{solv}}$, where ρ_{solv} is the electron density of the suspending medium.

Depending on the synthesis of the particles, the interface between the different phases might show a linear electron density gradient between the particle's components. Analogously to expression 2.26, the form factor of a multicomponent spherical particle with a linear gradient interface is

$$f\left(q, R\right) = \sum_{i=0}^{n-1}\left[m_i\left(F_{\text{lin}}(q, R_{i+1}) - F_{\text{lin}}(q, R_i)\right) + b_i\left(F_{\text{sph}}(q, R_{i+1}) - F_{\text{sph}}(q, R_i)\right)\right] \tag{2.28}$$

where $m_i = {(\rho_{i+1} - \rho_i)}/{(R_{i+1} - R_i)}$ and $b_i = \left(\rho_i - \rho_{\text{solv}}\right) - R_i m_i$ and the linear form factor is defined by

$$F_{\text{lin}}(q, R) = 4\pi\frac{\left(2qR\sin(qR) + 2\cos(qR) - (qR)^2\cos(qR)\right)}{q^4} \tag{2.29}$$

The presented form factors are the models used in this work to analyse the experimental SAXS data of nanoparticles in suspension which will be discussed in chapters 4, 5 and 6.

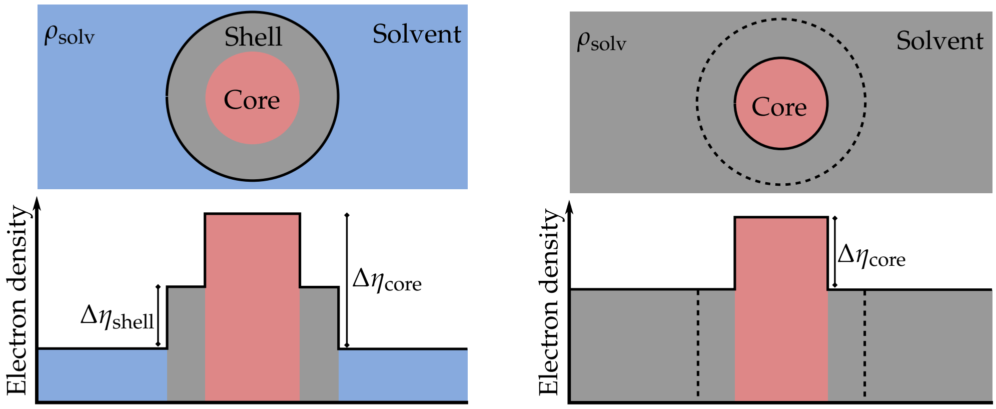

(a) Core-shell particle in solvent **(b)** Contrast matching of the shell

Figure 2.5 | Variation of the solvent electron density represented by the electron density profile of a spherical core-shell particle: a) The contrast of both core and shell components is high ($\Delta\eta_{\text{core}} > \Delta\eta_{\text{shell}} > 0$), while in figure b) the solvent electron density is increased to match the shell's ($\Delta\eta_{\text{shell}} = 0$). In this case, the only contribution to the scattering intensity will arise from the core.

2.3 Contrast variation

In the contrast variation method, the electron density of the particle or the surrounding medium is systematically altered in order to obtain independent scattering curves with different contrasts $\Delta\eta(r)$. This technique is useful to characterize the different components of heterogeneous particles, due to the complementary data that can be collected at each contrast. The work presented in this thesis is focused in the *solvent contrast variation* method, where only the electron density of the suspending medium is varied.

By means of the solvent contrast variation approach, the electron density of a single phase of the investigated particle can be matched (i.e. *match point*), resulting in a increased scattering amplitude of the other components of the object, as depicted in figures 2.5a and 2.5b. This effect enables a much more detailed study of the different contributions of the particle's components to the scattering intensity, which can be isolated by choosing the solvent electron density appropriately. In the following paragraphs, the theoretical framework required to interpret a SAXS contrast variation experiment will be presented, focusing mainly on the effects produced by the variation of the solvent electron density ρ_{solv}.

2.3.1 Isoscattering point

One of the best known features appearing in a contrast variation experiment with heterogeneous nanoparticles is the existence of *isoscattering points*, first formulated by Kawaguchi *et al.* (1983). At these specific q-values, the scattering intensity is independent of the adjusted solvent contrast, i.e. all scattering curves intersect in the isoscattering points regardless of the contrast. The isoscattering points $q^\star$ are particularly interesting because they emerge for any spherical particle with an inner structure and a sufficiently narrow size distribution. From the contrast-depending part of equation (2.26), a model-free expression can be derived which relates the position of the isoscattering points $q_i^\star$ with the external radius of the particle R, independent of its radial structure (Kawaguchi *et al.*, 1983; Kawaguchi & Hamanaka, 1992):

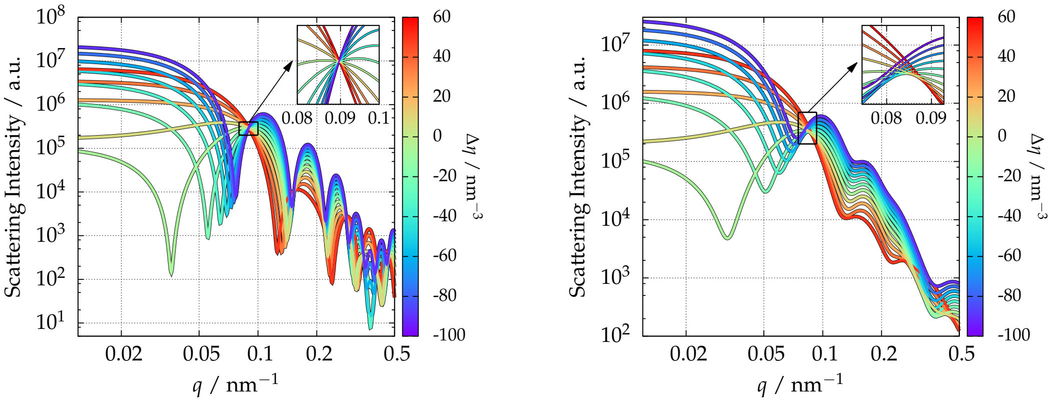

(a) Monodisperse nanoparticles

(b) Polydisperse ensemble: $p_d = 30$ %

Figure 2.6 | A isoscattering point is the q-value where all the scattering curves measured at different contrasts $\Delta\eta$ intersect. a) In the monodisperse case, the first isoscattering point is well-defined as depicted in the inset, while the inset of b) shows how the high polydispersity of the ensemble produces a diffuse isoscattering point and the intersection point is smeared out.

$$\tan(q_i^\star R) = q_i^\star R \tag{2.30}$$

The solutions for this equation fulfill $q^\star R = 4.493, 7.725, 10.904, ...$, where the positions of the isoscattering points correspond to the minima positions of the scattering intensity of a compact spherical particle with radius R. This expression relates in a simple way the position of $q^\star$ to the size of the particle inaccessible to the suspending medium and, thus, a good method to determine the diameter of the colloid.

Although this expression is derived for the monodisperse case, it can still be applied up to a moderate degree of polydispersity, if care is taken regarding the shift of the minima position due to polydispersity (van Beurten & Vrij, 1981). For size distributions with p_d larger than ≈ 30 %, the isoscattering point is not well defined and the intersection point of the curves is smeared out, showing a diffuseness in the isoscattering point position (Kawaguchi & Hamanaka, 1992). The effect of polydispersity in the isoscattering point is illustrated by simulating a 100 nm core-shell particle for the ideal case of a monodisperse ensemble (figure 2.6a) and with a degree of polydispersity of 30 % (figure 2.6b). The shift of the isoscatterig point position to smaller q-values and the diffuseness of the intersection point due to the high p_d are clearly evident in the inset of figure 2.6b.

Similarly, any deviation from the spherical shape produces a diffuseness in the $q^\star$ position. Unfortunately, this effect cannot be distinguished from the smearing produced by the size polydispersity and the investigation of the particle shape needs to be performed by other means.

2.3.2 Basic functions approach

When analysing contrast variation data, a widespread theoretical approach is based on the non-interacting model proposed by Stuhrmann & Kirste (1965; 1967) for monodisperse particles. The so-called *basic functions* formulation differentiates, independently of the particle inner structure, the contributions which depend on the varying solvent density or contrast ($\Delta\eta$) and on the excess of electron density of each component of the particle.

Deriving from this approach, the scattering intensity can be expressed as the combination of contributions corresponding to different features of the particles:

$$I(q) = I_c(q) + \Delta\eta I_{sc}(q) + (\Delta\eta)^2 I_s(q) \tag{2.31}$$

The I_c function contains the contributions from the density fluctuations inside the particle, the contribution I_s is the so-called *shape scattering function* and I_{sc} is the cross-term function.

Shape scattering function

The $I_s(q)$ function corresponds to the scattering contributions from particles with homogeneous density and a size equivalent to the volume inaccessible to the solvent, typically the external size of the nanoparticle. By modelling the shape scattering function, the shape and size distribution of the particles can be determined independently of their inner structure. The functions $I_{sc}(q)$ and $I_c(q)$ are more rarely employed due to their complex interpretation. $I_c(q)$ contains the electron density deviations in the particle from the average electron density, while $I_{sc}(q)$ includes crossed contributions from both $I_c(q)$ and $I_s(q)$.

In a system measured at N different solvent electron densities i.e. contrasts, the shape scattering function I_s at each q-value can be calculated by solving the following matrix equation:

$$\begin{pmatrix} I_1(q) \\ \vdots \\ I_N(q) \end{pmatrix} = \begin{pmatrix} 1 & \Delta\eta_1 & (\Delta\eta_1)^2 \\ \vdots & \vdots & \vdots \\ 1 & \Delta\eta_N & (\Delta\eta_N)^2 \end{pmatrix} \begin{pmatrix} I_c(q) \\ I_{sc}(q) \\ I_s(q) \end{pmatrix} \tag{2.32}$$

where $I_i(q)$ is the measured scattering intensity at each solvent electron density and $\Delta\eta_i$ is the contrast corresponding to each suspending medium density. A minimum of 3 independent scattering curves measured at different contrasts are required to solve this system of equations, while an accurate determination of the suspending medium electron density is also necessary for the calculation of the different $\Delta\eta_i$.

Guinier approximation

The radius of gyration of a particle about its centre of mass R_g is defined as the second moment of the electron density distribution and can be calculated by

$$R_g^2 = \frac{\int \rho_e(r) r^2 dr}{\int \rho_e(r) dr} \tag{2.33}$$

The radius of gyration is systematically employed in small-angle scattering as an evaluation tool, due to its applicability to a large diversity of samples, e.g. proteins, colloids, suprastructures (Mertens & Svergun, 2010; Sim *et al.*, 2012). If the object is spherical, the gyration radius is directly related with its external radius by $R_g^2 = 3/5 R^2$.

In SAXS, R_g can be calculated using the Guinier approximation (Guinier, 1939; Guinier & Fournet, 1955), which assumes that the scattering intensity behaves in the limit of small q as

$$I(q) \simeq I(0) \exp\left(-\frac{R_g^2}{3} q^2\right), \tag{2.34}$$

where $I(0)$ is known as forward scattering or intensity at zero angle. Using the basic functions approach, the radius of gyration of a monodisperse, heterogeneous particle can be expressed as a function of the solvent electron density ρ_{solv} and the average electron density of the particle ρ_0 (Feigin & Svergun, 1987)

$$R_g^2 = R_{g,c}^2 + \frac{\alpha}{\rho_0 - \rho_{\text{solv}}} - \frac{\beta}{(\rho_0 - \rho_{\text{solv}})^2}, \tag{2.35}$$

where $R_{g,c}$ is the radius of gyration of the particle shape corresponding to the volume inaccessible for the solvent V_c, α characterizes the distribution of different phases inside the particle and $\beta > 0$ considers the eccentricity of the different scattering contributions (Stuhrmann, 2008). Particle aggregation influences the scattering curves especially in the Guinier region and must be explicitly avoided.

Avdeev (2007) proposed an extended version to equation (2.35) for the case of a polydisperse particle ensemble by introducing the *effective* values $\tilde{R}_{g,c}^2$, $\tilde{\alpha}$ and $\tilde{\beta}$, which are the intensity-weighted averages of the corresponding parameters over the polydispersity. The observed average electron density is not affected by the polydispersity ($\tilde{\rho}_0 = \rho_0$) if the volume ratio between the different particle components is constant for all particles in the ensemble.

Assuming the premise of a constant average electron density for all the particles, the intensity at zero angle for a polydisperse system can be expressed as

$$I(0) \propto N \left(\rho_0 - \rho_{\text{solv}}\right)^2, \tag{2.36}$$

with a minimum of the parabolic function at $\rho_{\text{solv}} = \rho_0$. Therefore, by analysing the Guinier region of the scattering curves in a contrast variation experiment, the average electron density of the particle can be obtained without assuming an *a priori* inner structure.

Using the models presented above, it is possible to obtain by independent means the external radius and the average electron density of the particles in suspension.

3

Instrumentation and experimental setup for SAXS measurements

Since the appearance of third generation synchrotron radiation facilities devoted to dedicated insertion devices and optimized for brightness, synchrotron radiation sources have become of importance in Small-angle X-ray Scattering experiments due to their high brilliance and collimation, favoring the application of SAXS in a wide variety of scientific fields. The most relevant instrumentation required in a small-angle X-ray scattering experiment are the X-ray source, a sample environment and an area detector which collects the elastically scattered photons.

The first part of this chapter (section 3.1) reviews the fundamentals of synchrotron radiation, while section 3.2 describes the synchrotron radiation source, the electron storage ring BESSY II. After these introductory sections, the four-crystal monochromator (FCM) beamline operated in the PTB laboratory at BESSY II is introduced (section 3.3), where all the reported results were measured. Following this, the area detector mounted on the HZB-SAXS instrument is reviewed (section 3.4), highlighting the newly developed *in-vacuum* Pilatus X-ray detector and the low uncertainty associated to the sample-detector distance that can be achieved with this setup. Finally, section 3.5 presents a detailed insight into the different sample environments needed for the nanoparticles in suspension studied in this work. A brief overview of the data reduction is given in section 3.6, emphasizing the *a posteriori* corrections required by the scattering curve.

3.1 Synchrotron radiation

Synchrotron radiation is the electromagnetic dipole radiation which is emitted by ultra-relativistic charged particles when they are circularly accelerated by an external magnetic field. The kinetic energy loss of the charged particles (typically electrons) due to the Bremsstrahlung process (Blumenthal & Gould, 1970) is tangentially radiated in form of a light cone with high brilliance and a wide photon energy range.

The total radiant power emitted by a single ultra-relativistic electron accelerated radially ($\vec{a} \perp \vec{v}$) by a homogeneous magnetic field is described by:

$$P_{\text{sync}} = \frac{e^2 c}{6\pi\epsilon_0 R^2} \left(\frac{E}{m_e c^2} \right)^4 \propto E^4 m_e^{-4} R^{-2} \tag{3.1}$$

where m_e and E are the rest mass and energy of the electron, respectively. R is the radius of the electron trajectory in the circular storage ring and is related to the external magnetic field strength of the bending magnet (B) by $R = \frac{E}{ecB}$. The use of light particles (electrons or positrons) in storage rings such as BESSY II is explained by the production of a radiative power $\sim 10^{13}$ times larger than heavier particles like protons due to the large proton-to-electron mass ratio ($({}^{m_p}/_{m_e}) > 1800$).

Synchrotron radiation sources generating X-rays photons have arisen as an important tool in many scientific fields like physical chemistry, life science or physics. The broad spectral range and the high brilliance open new experimental possibilities in materials science as well as in metrology. For instance, the synchrotron radiation can be employed as a primary calibration standard for electromagnetic radiation (Thornagel *et al.*, 2001) by means of the Schwinger equation (Schwinger, 1949), which describes the radiant power emitted by an electron as a function of the photon energy, and the determination of the number of electrons, the electron energy and the magnetic field of the bending magnet.

The two most characteristic features of a synchrotron radiation source are the brilliance and the critical energy or critical wavelength. The spectral brilliance is defined as the number of photons per second, per electron beam source cross section, per angular divergence and per 0.1 % bandwidth at a certain wavelength λ (Marr, 1987). The critical energy E_C is defined by (Schwinger, 1949):

$$E_C = \frac{3hc}{4\pi R} \left(\frac{E}{m_e c^2} \right)^3 \tag{3.2}$$

The critical energy E_C divides the spectral range into two parts with equal radiant power (Marr, 1987).

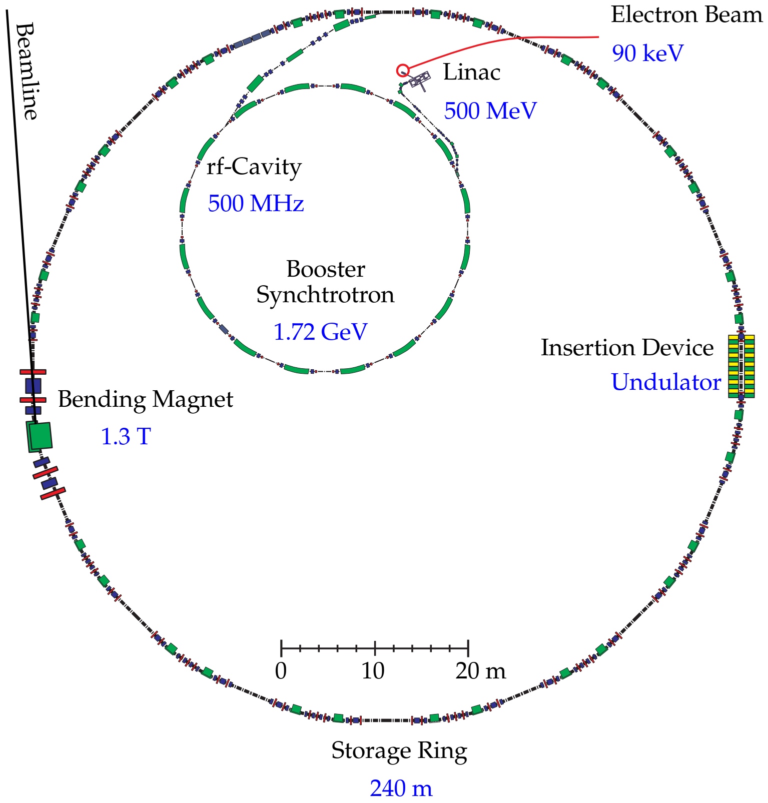

Figure 3.1 | Scheme of the electron storage ring BESSY II. The different components involved in the creation of X-rays are depicted.

3.1.1 Insertion devices

The synchrotron radiation sources of the third generation are designed with the goal of optimizing the insertion devices and, therefore, enhance the spectral brightness (Robinson, 2015). The employment of insertion devices, such as wigglers or undulators, on the straight sections of the storage ring improves the brilliance in comparison to the bending magnets or produces light polarizations different from that produced by bending magnets.

Both insertion devices consist on the same principle: a large number ($N \sim 100$) of equally spaced alternately polarised dipole magnets stimulate the emission of synchrotron radiation on the experiment direction, due to the coherent addition of the contributions from the passage of a single electron. By this approach, the photon flux can be increased in a factor N, the number of magnets separated with a spatial field period λ_0 in the range of cm. The distinguishable property between wigglers and undulators is their deflection parameter K, defined by (Marr, 1987):

$$K = \frac{e}{m_e 2\pi c} B_0 \lambda_0 \tag{3.3}$$

where B_0 is the magnetic field amplitude of the dipole magnet. Normally, K can be modified by varying the space between the dipole magnets (*gap*) and, thus, whether the insertion device is called a wiggler or an undulator depends on its particular configuration.

The value of K is rather large in the case of wigglers, emitting radiation in a broad spectral range and increasing the E_C of the storage ring. On the other hand, undulator devices have $K \leq 1$, emitting an almost monochromatic and highly intense photon beam. The sharp harmonic peaks observed in the undulator spectrum are produced by the

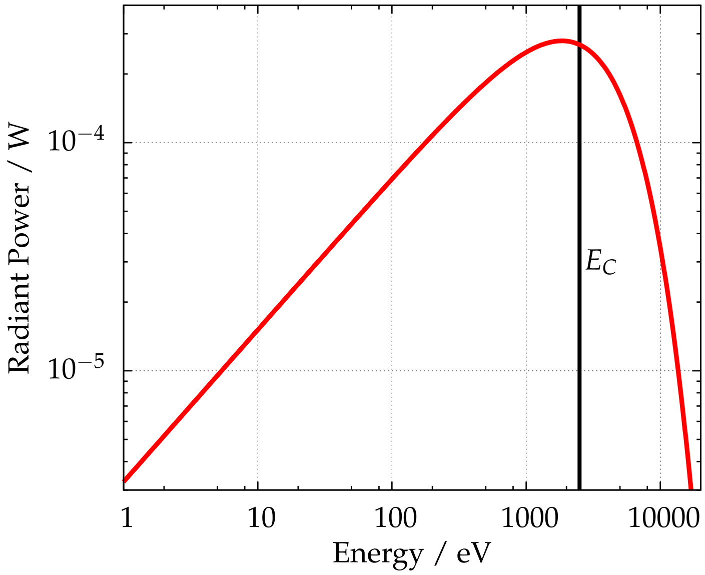

Figure 3.2 | Radiant power of the bending magnets at BESSY II under standard operation (300 mA) through an aperture of 10 x 10 mm^2 situated at 30 m of the source calculated using the Schwinger equation. The critical energy E_C is 2.5 keV and divides the spectrum into two parts with equal power.

coherent constructive interference of the radiation from the different dipole magnets.

3.2 The BESSY II electron storage ring

The facility BESSY II situated in Berlin (Germany) is a synchrotron X-ray and UV light source of the third generation. The electrons are accelerated to 1.72 GeV in a booster synchrotron and injected into a storage ring with 240 m circumference and an electron current of approximately 300 mA in the TopUp Mode (Couprie & Filhol, 2008). The following paragraphs describe the creation of X-rays from the acceleration of the electron beam until the emission of synchrotron radiation on the bending magnets situated along the storage ring (Bakker *et al.*, 1998; Bakker, 1999).

The creation of the free electrons on the electron beam is the first step, as depicted schematically in figure 3.1. A standard DC grid cathode emits electrons which are accelerated with a high voltage to the anode up to a 90 keV energy. These electrons are the source of a 50 MeV Linac, which brings the electron beam to relativistic velocities. The 0.4 nC charged electrons bunches are further transported to a 10 Hz booster synchrotron by a long Injection Line. The acceleration process in the rapid-cycling synchrotron takes about 50 ms and is achieved by the disposition of a set of magnets and 500 MHz rf-cavities coupled with the magnets in linear paths that ramp the electron beam to its final operation energy of 1.72 GeV.

At this point the electrons are injected into the storage ring, where 32 bending magnets with a magnetic field strength of 1.3 T and a bending radius of 4.35 m (Klein *et al.*, 2014) are equipped to maintain the circular trajectory of the electron beam at 1.25 MHz revolution frequency. Figure 3.2 depicts the calculated radiant power of the bending magnets at BESSY II as a function of the photon energy, where the critical energy E_C of 2.5 keV is shown.

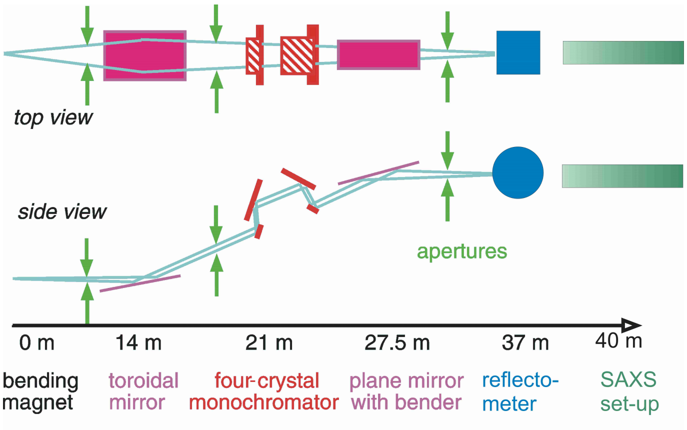

Figure 3.3 | A scheme of the FCM beamline in the PTB laboratory at BESSY II. The distance of each component to the bending magnet is shown (Krumrey, 1998).

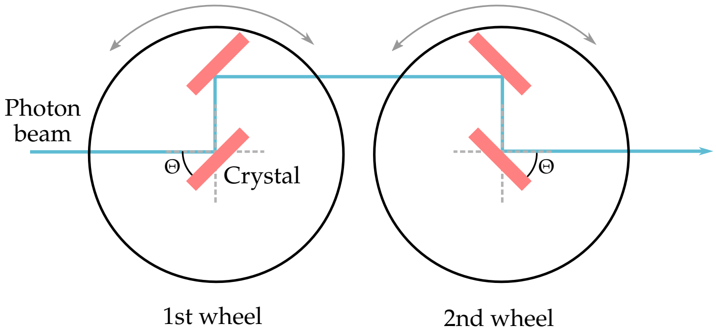

Figure 3.4 | Scheme of the four-crystal monochromator: The rotation angle of the wheel Θ defines the Bragg angle on the crystal. The outgoing photon beam is parallel to the incoming radiation due to the geometrical disposition of the 4 crystals.

3.3 FCM beamline

The four-crystal monochromator bending magnet beamline operating in the PTB laboratory at BESSY II (Krumrey, 1998; Krumrey & Ulm, 2001) provides a monochromatic beam in the 1.75 to 10 keV energy range at a fixed sample position with very high photon flux reproducibility and high energy resolving power. A schematic depiction of the beamline and its components is shown in figure 3.3.

At 14 m from the bending magnet, a Pt-coated toroidal mirror is located to focus the beam in the horizontal direction and to collimate it in the vertical direction. The radiation coming from the bending magnet is monochromatised further downstream by a set of 4 single crystals which reflect the light according to the Bragg's law for the (1 1 1) reflection as schematically depicted in figure 3.4. As the 4 crystals are mounted on two wheels (one on the rotation centre and one parallelly aligned), the rotation angle of the wheel Θ defines the energy of the outgoing photon beam by $E = \frac{\sqrt{3}hc}{2a \sin\Theta}$, where a is the lattice constant of the crystal.

Two types of exchangeable crystal sets, Si ($a = 0.543$ nm) and InSb ($a = 0.648$ nm) (Kittel, 2004), are available to cover the energy range from 1.75 keV to 10 keV. The convolution of the 4 Bragg reflections provides a very high energy resolving power ($E/\Delta E = 10^4$) through the full energy range. Besides, the geometric disposition of the crystals fixes the position of the outgoing radiation. The monochromator is operated under a 10^{-8} mbar vacuum.

The energy is traced back to the well-known lattice constant of Si (Kittel, 2004). The back-reflection of a silicon crystal at different lattice planes is measured at distinct energies and the energy is calibrated to the dips positions appearing when the Bragg condition is fulfilled (Krumrey & Ulm, 2001). This approach was employed at the sensitive surface

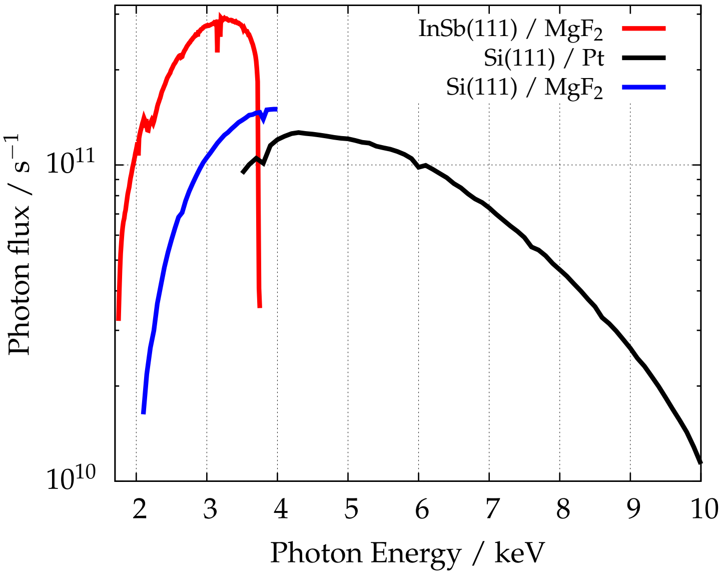

Figure 3.5 | Photon flux of the FCM beamline using different crystals (InSb(111) and Si(111)) and mirror coatings (MgF_2 and Pt) at standard operation (300 mA).

of the X-ray detector introduced in section 3.4.1 for an energy range between 4 keV and 10 keV (Gollwitzer & Krumrey, 2014). To check the accuracy of the energy calibration for daily measurements, a transmission scan around the K-edge of a copper foil (8980.5 eV) is measured.

About 10 m before the sample chamber, a bendable plane mirror focuses the beam in the vertical direction. The mirror is coated with two different materials in separated areas. The Pt-coating is employed to maximize the reflectivity at energies above 4 keV, while the MgF_2 suppresses the higher orders at energies below 4 keV. The photon flux achieved with the different configurations available at the FCM beamline is shown in figure 3.5, although it can vary depending on the precise disposition of the different apertures along the beam path.

The first slit behind the bending magnet is used to limit the acceptance angle of the radiation into the monochromator. Two moveable slits more are employed downstream to block the parasitic scattering. A germanium 520 μm circular pinhole (Scatex, Incoatec, Geesthacht, Germany) situated before the sample chamber shapes the photon beam into a circular spot on the sample and strongly reduces the parasitic radiation. A 8 μm thick silicon photodiode diode is installed behind these components and can monitor continuously the incoming photon flux for energies above 3 keV.

3.3.1 UHV X-ray reflectometer

The sample chamber is situated 37 m away from the dipole i.e. bending magnet, right behind the flux monitor diode. The UHV X-ray reflectometer disposes of a large volume (60 cm diameter and 70 cm length) which is fully evacuated to reach pressures of approximately 10^{-7} mbar. High vacuum is needed to perform experiments at the low energies accessible at the FCM beamline, as the attenuation length of air at energies below 2 keV is less than 1 cm. A smaller lock chamber connected to the sample chamber by a 200 mm diameter flange is used to exchange samples without breaking the vacuum of the larger UHV X-ray reflectometer.

The motors of the sample holder can be moved linearly in three mutually perpendicular directions with very high precision and reproducibility. The broad range of the x-motor perpendicular to the incoming beam (160 mm) permits the measurement of different sample capillaries (ca. 20) at once without venting the chamber for exchanging the sample.

The large volume of the reflectometer provides enough space to allocate other components close to the sample holder. For example, about 10 cm before the sample position, a 1 mm circular guard pinhole (Incoatec, Geesthacht, Germany) is installed to remove the parasitic scattering resulting from the collimating system. Behind the sample, the transmitted radiation is measured with a (10 x 10) mm^2 silicon photodiode. The thick Can500C diode (Canberra, Meriden, USA) is capable of measuring through the entire beamline energy range, from 1.75 keV to 10 keV, and is calibrated against a cryogenic electric substitution radiometer with a relative uncertainty of 1 % (Krumrey & Ulm, 2001).

3.4 SAXS setup

The intensity scattered by the sample is recorded at a certain distance behind the sample (sample-detector distance) with an area X-ray detector mounted on the HZB SAXS instrument and connected to the sample chamber. Typically, long sample-detector distances are required to access the small angles employed in SAXS experiments.

3.4.1 X-ray area detector

The scattered X-ray photons are collected by a large-area hybrid pixel detector. The Pilatus 1M (Dectris Ltd, Baden, Switzerland) has a sensitive surface of (179 x 169) mm^2 and consists of a silicon pixel matrix with a pixel size of $d = (172.1 \pm 0.2)$ μm which operates in single-photon counting mode, providing very low darkcount rates, very good signal-to-noise ratios and a high dynamic range. For instance, the detector quantum efficiency is about 97 % at 8 keV using the ultra-high gain mode and almost 86 % at 4 keV (Wernecke *et al.*, 2014).

Besides, the Pilatus 1M detector was modified to operate under vacuum to cover the full energetic range available at the beamline, down to 1.75 keV. The windowless detector is directly connected to the sample chamber with an evacuated bellow and cooled down at 5 to 10 °C. The narrow point-spread function of the detector and the available low energies increase the momentum transfer resolution and the accessible q-range.

A moveable beamstop mounted at thin wires is installed just in front of the detector to block the intense transmitted photon beam, avoiding saturation effects in the central pixels. The beamstop is constructed within a funnel-like cavity ($\oslash$ 5 mm) to reduce geometrically the reflections on the beamstop surface, which are damped by the cavity. Since April 2016, a silicon photodiode with a sensitive area of (2.5 x 2.5) mm^2 (S10356-01, Hamamatsu, Shizuoka, Japan) covers the beamstop to monitor the sample transmission during the experiment, revealing the possible radiation damage of the sample.

Table 3.1 | Two different experimental setups which span the accessible q-range for almost 3 decades. The overall maximum and minimum accessible q-values are highlighted in bold letters.

	SAXS	**WAXS**
Distance (mm)	4540	760
Energy (eV)	4000	10000
q_{min} (nm^{-1})	**0.015**	0.2
q_{max} (nm^{-1})	0.56	**7**

3.4.2 HZB SAXS instrument and WAXS configuration

The in-vacuum Pilatus 1M detector is mounted on the SAXS instrument of the Helmholtz-Zentrum Berlin (HZB) (Gleber *et al.*, 2010), which is connected via a $\oslash$100 mm flange to the UHV X-ray Reflectometer. The HZB-SAXS apparatus is equipped with a large below system and a motorized stage that can vary the sample-detector distance continuously between 2.3 m and 4.6 m in vacuum (about 10^{-4} mbar) with an uncertainty of 20 μm.

Complementary to the HZB-SAXS instrument, the sample-detector distance can be reduced down to about 760 mm by attaching the X-ray detector directly to the sample chamber, increasing the scattering angles to around 8°. This short-distance setup, or Wide-angle X-ray Scattering (WAXS) configuration, is used for the study of nanoparticles with diameters below 10 nm, whose characteristic features appear beyond 1 nm^{-1}. The accessible q-range of this setup is summarized in table 3.1 for the high-energy case, which provides the highest q-value available. Similarly, the table shows the limit q-values achieved with the HZB-SAXS apparatus at low-energy.

Calibration of the sample-detector distance

In small-angle scattering experiments, it is crucial to know precisely the distance between the irradiated sample and the detector, in order to calibrate the momentum transfer q. Typically, a calibration standard material with a previously measured crystal lattice parameter is employed, which produces well-defined diffraction rings in the low-angle region. A material extensively used is dry rat-tail tendon collagen, with a d-spacing of 65 nm (Amenitsch *et al.*, 1997), corresponding to $q = 0.097\ \mathrm{nm}^{-1}$. The degradation of this material upon prolonged radiation suggested the use of harder calibrants such as silver behenate ($CH_3(CH_2)_{20}COO{\cdot}Ag$) (Huang *et al.*, 1993).

AgBehe has a very narrow diffraction ring at $q = 1.0763\ \mathrm{nm}^{-1}$, arising from a long-period spacing (d_{001}) value of 5.84 nm (Blanton *et al.*, 1995), although this value depends slightly on the synthesis. A deviation of 0.5 % in the diffraction peak position could be observed for different sample preparations. In order to increase the accuracy of the calibration, the sample-detector distance was determined by the detection of the scattering pattern of AgBehe at different positions of the HZB SAXS instrument, measured with the built-in 3 m long Heidenhain optical encoder. By triangulating the radius of the diffraction ring to the source point, as depicted in figure 3.6a, the sample-detector distance is obtained in a traceable way.

By measuring the AgBehe pattern along a distance range of 2200 mm with 100 mm steps at 8000 eV, the relative uncertainty associated to the linear fitting is 0.03 %, corresponding to 1.5 mm. As observed in the residuals of the fitting in figure 3.6a, the deviation increases for long distances, due to the relatively small d-spacing of AgBehe, disabling the use of distances larger than $\sim$ 3600 mm. In figure 3.6b, it is visible how the diffraction ring surpasses the surface of the detector at a distance of 3638.2 mm and, thus, diminishes the

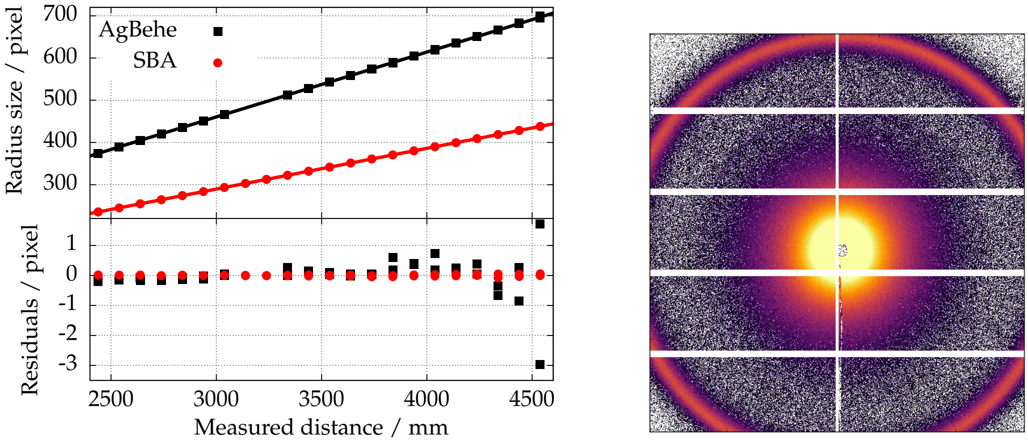

(a) Distance Calibration

(b) AgBehe at large distance

Figure 3.6 | Sample-to-detector distance calibration: a) Radius of the diffraction ring of AgBehe and SBA-15 as a function of the sample-detector distance. A linear function is fitted to obtain the source point distance. The residuals of the fitting are shown in the bottom plot. b) Scattering pattern of AgBehe measured at a distance of 3638.2 mm. At such long sample-to-detector distances, the diffraction rings exceeds the detector area and the associated uncertainty increases.

accuracy of the peak determination.

By using a material with lower q-value, such as the templated mesoporous silica SBA-15 with $q = 0.681\ \mathrm{nm}^{-1}$ (Zhao *et al.*, 1998), this limitation can be mitigated as shown in figure 3.6a, where the residuals of SBA are minimal for the entire distance range. By using SBA (kindly provided by R. Schmack (Technische Universität Berlin, Germany)) and increasing the accessible distance range, the relative uncertainty of the fit decreases in a factor 5, reaching an uncertainty of 0.004 % (0.2 mm) when measuring with 50 mm steps. This improvement is also related with the narrower diffraction peak of SBA-15 (FWHM/$q = 2.6$ %) in comparison to AgBehe (5.5 %).

Although the fit uncertainty is smaller in the SBA case, the position and shape of diffraction peak depend strongly on the sample preparation (e.g. template pore size). For the same polymer template, the q-value of the ring can vary until 1 % for different thermal treatments and radiation damage effects are visible for short calcination times. On the other side, prolonged beam exposure of AgBehe can damage the sample as well and create small silver nanoparticles, which increase the scattering background (Liu *et al.*, 2006). The choice of the calibration standard depends strictly on the needs of the experiment. Besides, the largest contributions to the sample-detector distance uncertainty come from the thickness of the sample (ca. 0.5 mm) and from the difference between the calibration with AgBehe and SBA-15 (also 0.5 mm). Normally the relative uncertainty associated with the distance calibration is 10^{-4}, similar to the energy resolving power described in section 3.3.

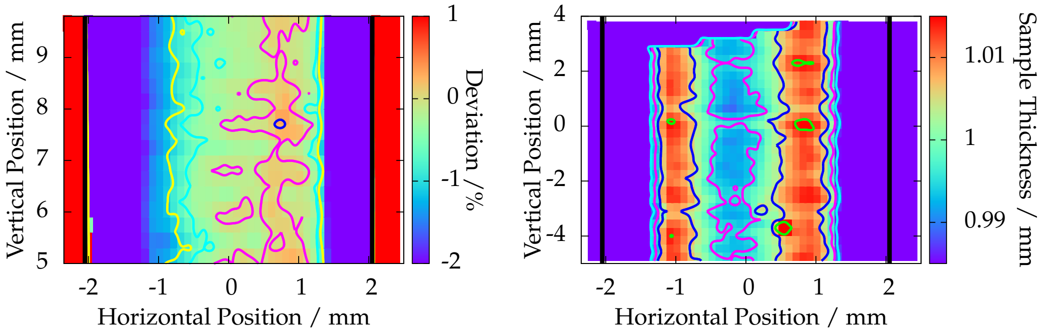

(a) Glass thickness **(b)** Sample thickness

Figure 3.7 | Homogeneity of the rectangular capillaries: a) Deviation of the empty capillary tranmission, i.e. glass wall thickness, b) Sample thickness calculated from the water transmission of a filled capillary.

3.5 Sample environment

The sample consists normally of a few microliters of nanoparticles in solution which are measured in a vacuum-proof container positioned inside the reflectometer. The sample environment must fulfill some requirements:

- The container's material should minimize the unnecessary absorption of the X-ray photon flux by the sample environment.
- The container volume should be small enough to enable the measurement of valuable, limited samples.
- The optimal sample thickness for a transmission diffraction experiment is the inverse of its attenuation coefficient $\mu(E)$, which reduces the incoming intensity to ~ 37 %. For example, the optimal thickness of water at 8000 eV is around 1 mm.

Typically, the samples are introduced in thin glass capillaries which maintain the temperature and pressure of the sample close to the ambient conditions. However, there are different sample environments which can be used depending on the requirements of the experiment. In this work, only nanoparticles suspended in aqueous media have been employed, allowing the use of a similar attenuation coefficient for almost all experiments.

3.5.1 Round capillaries

For single-contrast SAXS measurements, borosilicate glass round capillaries of 100 mm length were used. They were purchased at WJM Glass (Berlin, Germany) and had a nominal inner diameter of 1 mm and a wall thickness of 10 μm. The sample is filled into the capillary with a long syringe (Sterican® 21 x 4 3/4", Braun, Melsungen, Germany), avoiding the contact of the needle with the capillary walls. The top end of the capillary is closed by welding.

The very narrow glass walls (with a density of about 2.23 g cm^{-3}) absorb only 14 % of the incoming flux at 8000 eV and produce very low scattering background. Therefore, these capillaries are suitable for standard SAXS measurements. Unfortunately, the capillaries

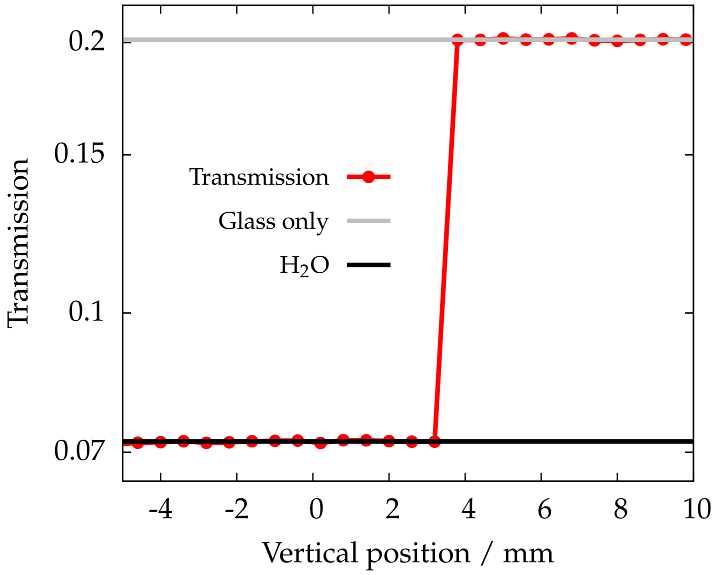

Figure 3.8 | X-ray transmission of a rectangular capillary half-filled with water along the main vertical axis situated at $x = -0.15$ mm.

sample thickness shows a significant deviation along the vertical axis and are inappropriate for measurements at different capillary heights, as needed for the continuous contrast variation technique.

3.5.2 Rectangular capillaries

The capillaries used for the contrast variation experiments are vacuum-proof borosilicate glass capillaries from Hilgenberg (Malsfeld, Germany) with a nominal rectangular cross section with outer dimensions of (4.2 $\pm$ 0.2) x (1.25 $\pm$ 0.05) mm^2, a length of (80 $\pm$ 0.5) mm and a wall thickness of ca. 120 μm. The thicker glass walls reduce the transmitted intensity to about 80 % at 8000 eV, but in contrast both the glass and sample thicknesses are very homogeneous for the entire capillary.

The transmission of an empty capillary is mapped in figure 3.7a, where it can be observed that the deviation of the glass wall thickness is less than 2 % for an horizontal range of 2.5 mm (of a total width of 4.2 mm). This range is at least 5 times larger than the typical beam diameter, avoiding the convolution of different thicknesses in the measurement. Similarly, figure 3.7b depicts the sample thickness in the capillary, calculated from a capillary filled with water using the Beer-Lambert law, the glass transmission and the mass attenuation coefficient of water at 8000 eV, 10.37 cm^2 g^{-1} (Hubbell *et al.*, 1996). The thickness of the sample introduced in the capillary is homogeneous within 2 % for a width range of ca. 2.5 mm.

From these figures, it is clear that the homogeneity of the sample environment is even better along the main vertical axis of the capillary. Figure 3.8 shows the measured X-ray transmission of a half-filled capillary along its vertical axis (at the horizontal position -0.15 mm). For example, the glass transmission within a 6 mm vertical range is 20.1 %, with an associated relative uncertainty of $\delta_r T = 0.6$ %. By calculating $\delta_r d = \frac{\delta_r T}{log(T)}$ where T is the glass transmission, the relative uncertainty of the glass thickness is $\delta_r d = 0.4$ %. Analogously, the uncertainty of the water transmission is 0.9 % and the sample thickness has an uncertainty of 0.9 % along the vertical axis.

These rectangular capillaries are a very suitable sample environment for measurements which require a high homogeneity along the vertical axis of the capillary. The thickness of

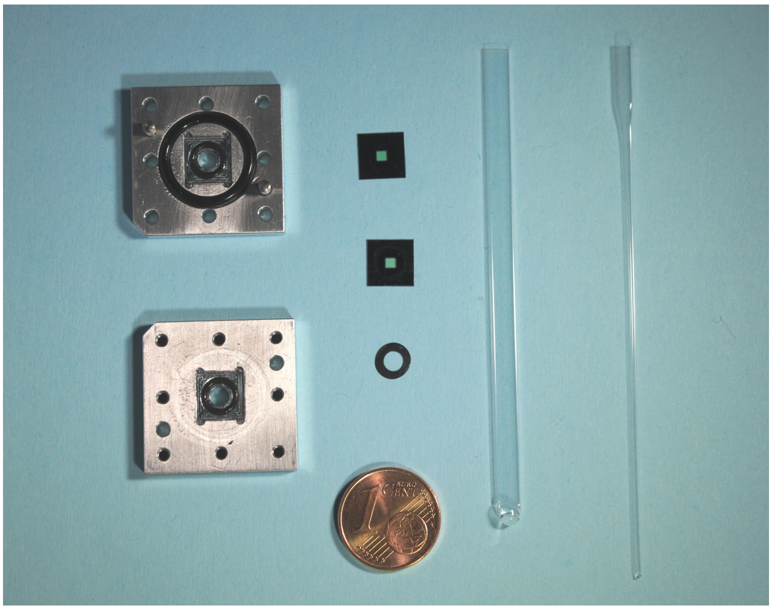

Figure 3.9 | Different sample environments: On the left side, the disassembled low-energy cell with the two silicon-nitride windows, the polymeric ring spacer and the two parts of the metallic holder. On the right side, the round and rectangular capillaries.

the wall varies only by 0.4 % and the sample thickness less than 0.9 %, although the thick glass walls reduce considerably the transmitted intensity and produce larger background scattering than the round capillaries.

3.5.3 Cell for low-energies

Samples with larger structures require the measurement of scattering curves at lower q-values. To extend the measurable q-range, one possibility is to reduce the photon energy, though this involves reducing the sample thickness, due to the short penetration length of X-rays at low energies. Therefore, a custom-made sample holder is used utilizing silicon-nitride windows (NX7150E, Norcada Inc., Edmonton, Canada). The 500 nm thickness windows produce very low scattering and have a negligible absorbance (< 5 %) for energies above 4000 eV.

A polymeric 100 μm ring cut with a microtome is used as spacer between the 2 windows, in order to achieve the desired 120 μm sample thickness which optimizes the intensity attenuation at 4000 eV. The access to smaller q-values using this cell is shown in Varga *et al.* (2014*b*), where a value of $q = 0.015$ nm^{-1} is achieved. The different components of the cell are shown in figure 3.9.

3.6 Data reduction: the scattering curve

In the case of nanoparticles in suspension and other isotropically scattering samples, the scattering patterns collected in the area detector consist of concentric rings whose centre is the transmitted beam. The dimensionality of the data can be reduced by performing a radial integration of the measured pattern, converting the 2D images into 1D scattering curves. This reduction step is based on the q-binning: the grouping of pixels with similar scattering angle q irrespective of their azimuthal angle on the detector (Pauw, 2013). By averaging the scattered intensity of the pixels within the same q-bin ($I(q)$), the uncertainty of the data decreases in the scattering curve. The size of the bins depends on the requirements of the data evaluation while the bins are typically spaced uniformly, although logarithmic distributions are also extensively used. The difference in solid angle for each pixel due to the spherical projection of the scattering on a flat detector is also considered in this step.

The uncertainty associated to the intensity $I(q)$ is calculated as the standard deviation between each pixel intensity in the q-bin, which gives a better estimate than the uncertainty associated to the photon-counting Poisson statistics (Pauw, 2013). The pixels discarded (or *masked out*) for the weighted average of the nth q-bin (q_n) are those whose intensity is not comprised within the range

$$\left[\frac{\left|I_{\text{med}}\left(q_{n-1}\right)-I_{\text{med}}\left(q_{n}\right)\right|}{2}-3\sigma,\frac{\left|I_{\text{med}}\left(q_{n+1}\right)-I_{\text{med}}\left(q_{n}\right)\right|}{2}+3\sigma\right], \tag{3.4}$$

where $I_{\text{med}}\left(q_n\right)$ is the median intensity of the pixels prior to this *masking procedure* and σ is the standard deviation. With a confidence level of 99.7 %, the pixels excluded of the reduction process are those pixels whose intensity lies clearly out of the radial average, such as *hot pixels*, anisotropic scattering from the glass capillary or undesired reflexes without radial simmetry.

The position of the centre of the scattering pattern is of vital importance for the radial integration step. A standard calibrant with very narrow diffraction rings such as AgBehe can be used to locate the centre with high precision. Nevertheless, the masking process previously described can be used as well to determine the centre position by minimizing the number of masked pixels and the standard deviation uncertainty of the q-bins. The accuracy of the centre determination is sub-pixel using both approaches, but the masking procedure does not require a calibration standard material.

The scattering curve obtained by radial integration still requires of some data correction. For instance, $I_{\text{meas}}(q)$ (photon counts) must be normalized to the exposure time Δt, the solid angle $\Delta\Omega$, the incident photon flux Φ_0, measured by the flux monitor described in section 3.3, and the measured transmittance of the sample T, which implicitly contains information about the density and chemical composition of the sample. In order to present the scattering cross section $d\sigma/d\Omega$ per volume V ($d\Sigma/d\Omega$) in absolute units (cm^{-1}), the measured intensity must be normalized to the sample thickness t and the quantum efficiencies of the X-ray detector and the silicon diodes η_{QE}:

$$\frac{d\Sigma}{d\Omega}\left(q\right)=\frac{\frac{d\sigma}{d\Omega}\left(q\right)}{V}=\frac{I_{\text{meas}}\left(q\right)}{\Phi_0\cdot T\cdot\Delta\Omega\cdot\Delta t\cdot\eta_{QE}\cdot t} \tag{3.5}$$

By using the monitor diode on the beamstop as described in section 3.4.1, T and Φ_0 can be measured simultaneously during the experiment, without the necessity of the flux monitor diode.

Alternatively a standard material like lupolen (Kratky *et al.*, 1966; Shaffer & Hendricks, 1974) or glassy carbon (Perret & Ruland, 1972) can be employed to scale the measured scattering intensity to the known values of these materials.

The normalized scattering curve requires an accurate background correction. The scattering of the pure suspending medium and the sample environment can affect the evaluation of the data, specially for low-scatterers, and, therefore, the normalized scattering background must be subtracted to obtain a usable scattering curve.

4

Continuous contrast variation in SAXS: the density gradient technique

The contrast variation method in Small Angle X-ray Scattering (SAXS) experiments consists in systematically varying the electron density of the dispersing media to study the different contributions to the scattering intensity in greater detail as compared to measurements at a single contrast, as described in chapter 2. It emerges as an ideally suited technique to elucidate the structure of particles with a complicated inner composition and has been repeatedly employed to investigate the radial structure of nanoparticles in suspension, e.g. latex particles suspended in an aqueous medium (Dingenouts *et al.*, 1999; Ballauff, 2011). In Small Angle Neutron Scattering (SANS) the contrast variation technique is widely used by mixing water and deuterium oxide, but the use of deuterated chemicals and the incoherent contribution to the background as well as the limited access to neutrons restrict the application of this technique. Other methods for structural investigation (e.g. transmission electron microscopy (Joensson *et al.*, 1991; Silverstein *et al.*, 1989)) require prior treatment of the sample and are not ensemble averaged.

In SAXS, the solvent contrast variation technique is achieved by adding a suitable contrast agent to the suspending medium (e.g. sucrose) and recording the scattering data as a function of the adjusted solvent electron density ρ_{solv} (Ballauff, 2001; Bolze *et al.*, 2003). In order to resolve small changes of the radial structure, the average electron density of the colloidal particles must be close to the dispersant's, i.e., the *match point* should be approached, where the average contrast of the particle vanishes. In the case of polymeric latexes with electron densities ranging from 335 to 390 nm^{-3}, an aqueous sucrose solution is very well suited as the suspension medium, due to the easy realization of concentrated solutions with electron densities of up to 400 nm^{-3}. Previous studies on globular solutes (Kawaguchi & Hamanaka, 1992) and the influence of the sucrose on the size distribution of vesicles (Kiselev *et al.*, 2001*a*) show the feasibility of this technique, while further studies have investigated the effect of the penetration of the solvent into the particles (Kawaguchi, 1993).

The preparation of a number of different sucrose solutions has been a major inconvenience in solvent contrast variation experiments, due to the tedious, time-consuming process, possible inaccuracy in the sucrose concentration and the discrete range of available solvent electron densities. In this chapter, a novel approach using a density gradient column is introduced, which allows the tuning of the solvent contrast within the provided density range, resulting in a virtually continuous solvent contrast variation. By filling the bottom part of the capillary with a particle dispersion in a concentrated sucrose solution and the top part with an aqueous solution of the same particle concentration, a solvent density gradient is initiated with a constant concentration of nanoparticles along the capillary. Density gradient columns are extensively used in fields like marine biology (Coombs, 1981) or biochemistry together with centrifugation (Hinton & Dobrota, 1978), to create a continuously graded aqueous sucrose solution by diffusion of the sucrose molecules. By measuring the density gradient column at different points in time during the diffusion process of the sucrose, it is possible to choose *in situ* the most appropriate solvent densities to perform measurements close to the contrast match point. Combining this approach with SAXS, a very extensive dataset with a virtually continuous variation in the suspending medium density can be acquired in a short interval of time.

The experimental details of the proposed approach are shown in section 4.1, followed by the example of the continuous contrast variation technique applied to polymeric nanoparticles in section 4.2. The evaluation of the SAXS data using different methods is reviewed in section 4.3, jointly with the discussion of the experimental measurements and a summary of the obtained results. Finally in section 4.4 the applicability of the solvent contrast variation technique in SAXS is discussed and compared to other contrast variation techniques. Parts of this chapter have been adapted from an article published previously (Garcia-Diez *et al.*, 2015).

4.1 Experimental procedure

4.1.1 Preparation of the density gradient capillaries

The solvent density gradient is prepared in the rectangular glass capillaries presented in section 3.5, which are extraordinary homogeneous and show very uniform sample thickness within 0.9 % and glass thickness within 0.4 %. The bottom end of the capillary is closed by welding and the lower section, up to a height of ca. 1 cm, is filled with Galden® PFPE SV90 from Solvay Plastics (Brussels, Belgium). This fluid has an exceptionally high density of 1.69 g cm^{-3}, low viscosity and is immiscible with aqueous solutions. Consequently, a uniform interface with the particle suspension is formed at the bottom, which is employed as reference position for the X-ray transmittance measurements.

The studied nanoparticles in suspension are mixed with a high sucrose concentration (Sigma-Aldrich, Missouri, USA) and diluted in an aqueous solution, creating two mixtures with different solvent densities but equal particle concentrations. Directly above the Galden fluid, the denser of these two mixtures is filled into the capillary using a syringe up to a height of about 1 cm. The lighter aqueous dilution is then filled on top of the aqueous sucrose solution along ca. 1 cm. By the time the two components come into contact, the density gradient is initiated and the sucrose starts diffusing along the ca. 20 mm length of the filled capillary.

The calculated diffusion time constant of the solvent density gradient is ca. 10 minutes, considering that the diffusion coefficient of sucrose in water at 25 °C is $D = 5.2 \cdot 10^{-10}\ \mathrm{m^2\,s^{-1}}$ (Uedaira & Uedaira, 1985; Ribeiro *et al.*, 2006) and assuming that convection effects are negligible due to the small length-scale of the capillary (Berberan-Santos *et al.*,

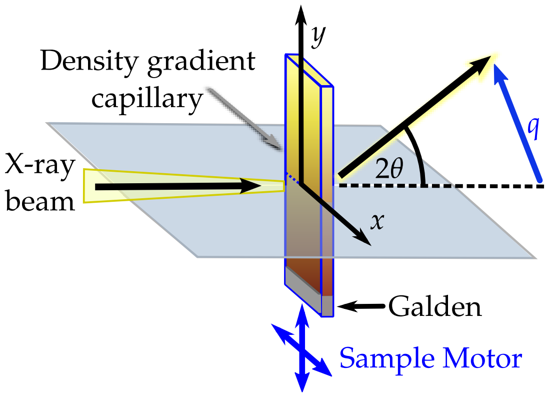

Figure 4.1 | The rectangular density gradient capillary is placed in the X-ray beam and can be moved by sample motors in both directions perpendicular to the incoming beam.

1997). The time needed for the transfer of the sample into the UHV sample chamber amounts to ca. 1 hour. Within this time duration, the simulations of the sucrose diffusion show that the deviation of the solvent density at both ends of the gradient from the initial value can be estimated with an uncertainty below 0.5 %.

4.1.2 Calibration of the solvent density: X-ray transmission

The rectangular capillary is placed in the sample holder inside the UHV reflectometer described in section 3.3 which allows the movement with micrometer precision in the directions perpendicular to the incoming beam, as depicted in figure 4.1. In order to determine the central vertical capillary axis, a horizontal X-ray transmission scan is performed at two different vertical positions of the capillary spaced by 20 mm. The central vertical axis can be drawn from the centres of both measurements and the sample can be moved along this axis by the simultaneous operation of the vertical and horizontal motors.

The transmitted intensity through the sample is recorded at a photon energy of $E = (5500.0 \pm 0.5)$ eV for 10 seconds at each position. The measurement points are spaced 0.5 mm along the central vertical axis of the capillary, starting at the bottom reference interface with Galden® PFPE SV90. The overall X-ray transmission measurement requires approximately 5 minutes, which is within the calculated diffusion timescale of the aqueous sucrose solution. This transmission measurement is performed both immediately before and after recording the scattering patterns, which should not take much longer than the sucrose diffusion timescale (15 to 20 min). The transmittance values used for the density calibration are then linearly interpolated between both data sets taking into account the time-dependence.

These values can be converted to solvent electron densities via the Beer-Lambert law introduced in section 2.1.1, which relates the density of the solution with the transmitted intensity:

$$\rho_e(z) = A \ln\left(\frac{I_0}{I(z)}\right) \tag{4.1}$$

Here ρ_e is the electron density of the suspending medium, I and I_0 are the transmitted and incoming intensities respectively and A is a factor determined by the reference values of the solvent electron density at the vertical limits of the capillary at the initial time. The sucrose concentration in solution expressed as the mass fraction M at these reference points

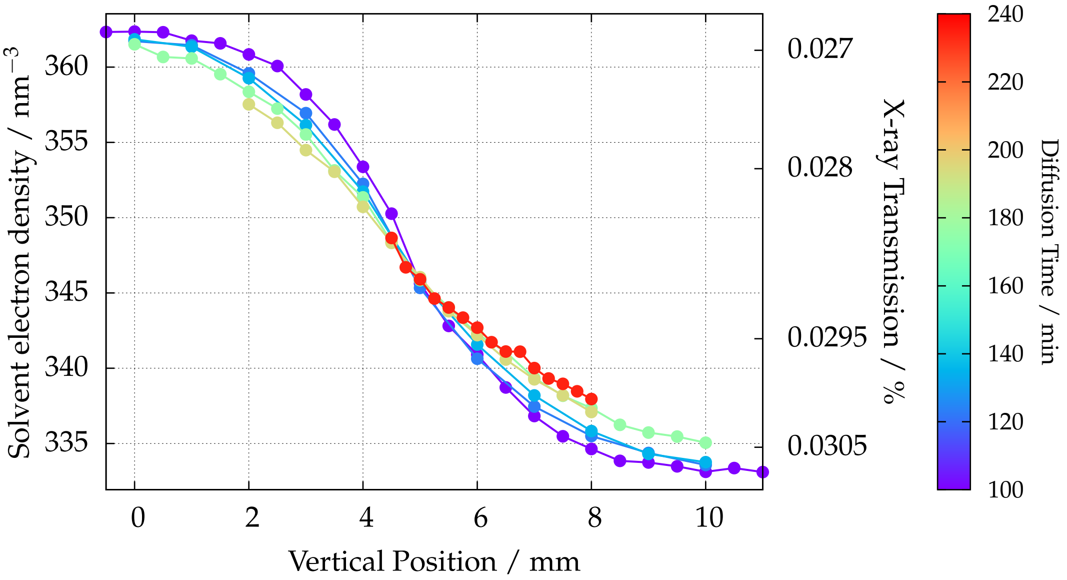

Figure 4.2 | Solvent density along the gradient capillary vertical axis at different diffusion times, calculated from the transmission measurements at 5500 eV of an aqueous solution with a maximum sucrose mass fraction of 23.5 % at the bottom of the capillary. The corresponding X-ray transmission is shown on the right axis, revealing the low transmittances of the filled capillary at low energies.

can be converted to electron densities with the empirical formula $\rho_e = 1.2681M + 333.19$ nm^{-3}, which relates the experimentally measured density of aqueous sucrose with its concentration (Haynes, 2012). The solvent electron density profile within the density gradient capillary derived from this measurement is depicted in figure 4.2 at different diffusion times for an aqueous solution with a maximum sucrose mass fraction of 23.5 % at the bottom of the capillary.

The focused X-ray beam has a vertical size at the capillary of around 0.5 mm which convolutes all the available sucrose concentrations within the illuminated sample volume and produces a scattering curve with an averaged suspending medium electron density. The largest averaging effect occurs at the interface between the two mixtures, where the steepest density variation is found. Although the uncertainty contribution of the beam size has typically a maximum value of 1 nm^{-3}, the uncertainty associated to the suspending medium electron density depends on the experimental conditions, e.g. diffusion time, sucrose concentration. In the results shown in section 4.2, a maximum uncertainty of 1.5 nm^{-3} was estimated.

The X-ray transmission measurements are performed at a low incident photon energy of $E = 5500$ eV to increase the transmittance differences for the less absorbing sucrose solution. In figure 4.3a, the calculated transmittances of a 65 % concentrated sucrose mixture and water (0 %) are depicted, along with the ratio between both transmissions. This ratio strongly decreases for high energies, suppressing the transmission differences between both components of the density gradient column. This fact is revealed in figure 4.3b, where the X-ray transmittance of an aqueous sucrose density gradient measured at 5500 eV shows a better signal-to-noise ratio than the same measurement at 10000 eV.

The calculated transmission of the empty rectangular capillary is less than 1 % below 6000 eV as shown in figure 4.3a and the filled capillary just transmits 0.03 % of the incoming photon flux at 5500 eV, as observed in figure 4.2. Therefore, a compromise between the absorbance ratio and the capillary transmittance was taken at a photon energy of 5500 eV.

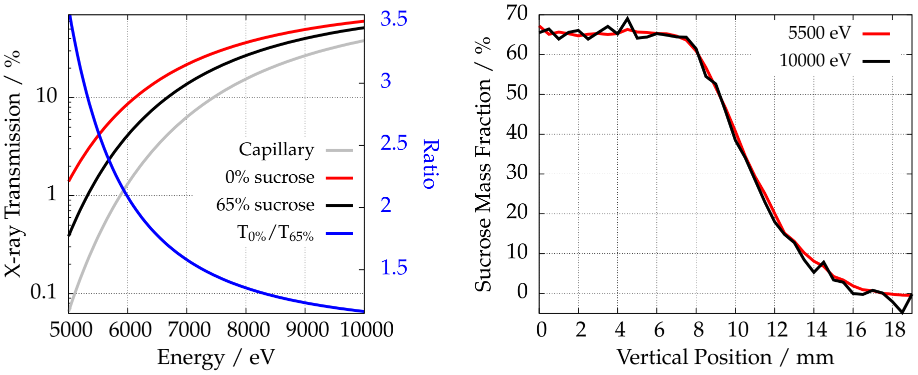

(a) Calculated transmittance **(b)** Calibrated sucrose concentration

Figure 4.3 | X-ray transmittance as a function of the photon energy. a) Calculated transmittances (Henke *et al.*, 1993) of an empty capillary, water and an aqueous sucrose mixture with 65 % mass fraction assuming a 1 mm sample thickness and the nominal specifications of the glass capillary. The ratio between the water and the sucrose mixture transmittances is shown in the right axis. b) Sucrose mass fraction derived from an experimental transmittance measurement of a 65 % sucrose density gradient measured at two different energies under similar experimental conditions. The absorbance differences are smaller for the higher energy.

4.1.3 SAXS measurements

In order to collect the scattering patterns, the sample is moved in steps of 0.5 mm along the central vertical capillary axis and exposed at each position for about 1 minute. The acquisition time depends notably on the experimental parameters (e.g. sample concentration, scattering power of the material...), though it is strictly limited by the diffusion time of the contrast agent. At these positions, the solution transmittances were previously measured and the suspending medium electron density calibrated, as described previously. Due to a vertical beam size of about 0.5 mm, the measured scattering curve is an average over a range of solvent electron densities, specially relevant at the height where the density gradient is steeper.

As a consequence of the observations from figure 4.3a, the incident photon energy $E = (8000.0 \pm 0.8)$ eV was chosen to be higher than the photon energy employed for the transmission measurements to improve the recorded statistics, due to a ca. 200 higher transmission (Henke *et al.*, 1993). On the other hand, the decreasing photon flux at the FCM beamline for high energies as depicted in figure 3.5, suggest the utilization of photon energies below 9 keV in scattering experiments.

The dimensions of the investigated particle defines the required q-range of the experiment, which is delimited by the photon energy and the sample-detector distance, as discussed in section 3.4. The photon energy is generally limited by the needs of the sample environment, but the distance can be adjusted with the HZB-SAXS instrument to the nanoparticle requirements and can compensate the energy restriction. For sizes typically ranging from 10 to 200 nm, the sample-detector distance is fixed at 4500 mm and enables q-values between 0.03 and 1.1 nm^{-1} at 8000 eV.

Since the installation in April 2016 of the monitor diode on the beamstop presented in section 3.4.1, the sample transmittance can be recorded simultaneously with the scattering patterns. The longer integration times required for the scattering experiments (around 60 s) increase by a factor 6 the statistics of the simultaneous X-ray transmission measurement, improving the quality of the transmittance data. The possibility to collect the

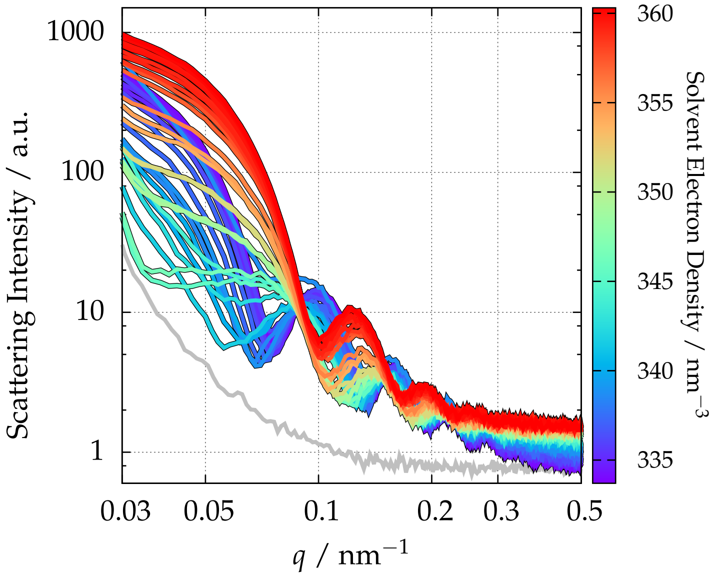

Figure 4.4 | Experimental scattering curves of the PS-COOH nanoparticles for different suspending medium electron densities measured between 78 and 93 minutes after the inception of the density gradient. The gray line shows the experimental background, containing scattering contributions from the capillary and the pure solvent.

scattering data at the same photon energy that the solution transmittances improves the normalization of the scattering curve and the calibration of the solvent electron densities. However, all the results presented in this work were recorded before the commissioning of the beamstop diode.

4.2 Proof of principle: application to the PS-COOH particles

In order to demonstrate the proposed continuous contrast variation technique, carboxylated polystyrene nanoparticles with a nominal size of 105 nm suspended in water (Kisker, Steinfurt, Germany) were measured following the procedure described previously in this chapter. The particles have a narrow size distribution and consist of a spherical polystyrene (PS) core enclosed by a thin shell of a denser polymer, most likely poly(methyl methacrylate) (PMMA). The synthesis by multi-addition emulsion polymerization is responsible of the core-shell structure found in these PS-COOH particles and suggests that all the particles have the same average density independent on their size.

The density gradient capillary was built according to the description in section 4.1.1 using two aqueous mixtures with a particle concentration of 12.6 mg ml^{-1} according to the producer's specification. The dense aqueous solution was prepared with 21.23 % sucrose mass fraction with a mass density of $\rho_1 = 1.088$ g cm^{-3}, whereas a lighter one was produced without sucrose ($\rho_2 = 0.997$ g cm^{-3}). In total, 40 scattering curves with different solvent electron densities were measured at two different times t_1 =78 min and t_2 =156 min after filling the capillaries.

The measured scattering curves of the PS-COOH particles are displayed in figure 4.4. In the region for q from 0.03 nm^{-1} to 0.5 nm^{-1} it is possible to observe the variation of the curve features corresponding to the particle form factor through the increase of the solvent electron density from 333.7 nm^{-3} at the top edge of the density gradient to 360.3 nm^{-3} at the maximum sucrose concentration. In this region, the experimental background is composed mainly by the contribution of the capillary scattering at the low q-region and the uniform scattering of the suspending medium. The experimental background scattering varies for different sucrose concentrations, but their variations are small and the

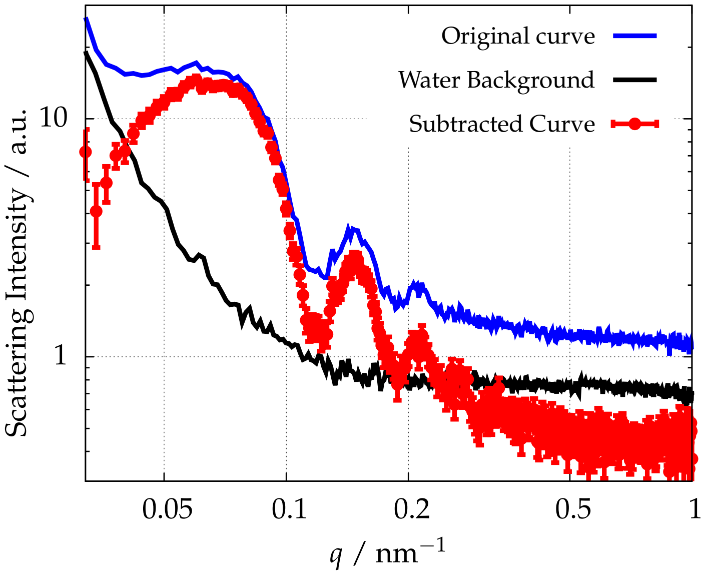

Figure 4.5 | The thick blue line shows the scattering curve measured at $\rho_{\mathrm{solv}} = 345.4\ \mathrm{nm}^{-3}$, close to the match point, and the black line displays the experimental background. The red symbols with errorbars show the background corrected scattering curve.

background remains one order of magnitude below the sample scattering in the relevant Fourier region.

Upon increasing the solvent density, the position of the first minimum shifts from $0.07\ \mathrm{nm}^{-1}$ towards smaller q-values until it vanishes when the solvent electron density matches the average electron density of the measured particle. In the Fourier region of the scattering curves, several minima are observed which shift towards smaller q-values when increasing the solvent electron density. Upon subtracting the experimental background from the scattering curve, a decrease of the scattering intensity towards $q = 0$ is observed only for the solvent electron density closest to the match point as depicted in figure 4.5. Therefore, background corrections can be neglected for systems with relatively high scattering power like in this study. For low-scatterers, an accurate background correction by measuring the pure suspending medium at different sucrose concentrations might be required. The behaviour at low q-values will be further discussed in section 4.3.3 when evaluating the zero-angle intensity.

The presence of the clearly visible isoscattering point around $q = 0.09\ \mathrm{nm}^{-1}$ confirms the existence of an inner structure. This heterogeneous composition was previously reported for the same colloids by Minelli *et al.* (2014), who observed methacrylic acid (MAA) and methylmethacrylate (MMA) at the particle surface, both monomer precursors of PMMA polymerization. A more detailed insight into the radial morphology is presented subsequently, using the theoretical framework introduced in chapter 2.

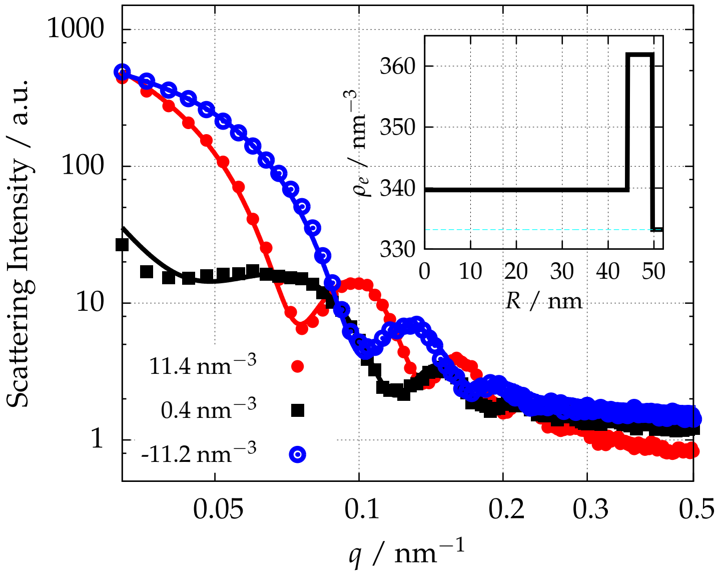

Figure 4.6 | The simulated scattering curves from the core-shell model fit at three selected contrasts $\rho_0 - \rho_{\mathrm{solv}}$ are shown as lines together with the experimental data points. In the inset, the electron density profile corresponding to the fitted core-shell form factor is displayed.

4.3 Results and data evaluation

The scattering curves of the PS-COOH nanoparticles measured at several contrasts can be analysed using different, complementary evaluation methods. In this section, both a model-free theoretical framework as well as a core-shell model fit are applied and, in combination, deliver a detailed insight into the inner structure of particles.

4.3.1 Core-shell form factor fit

A core-shell model fit to the scattering curves is displayed in figure 4.6 for three representative contrasts, which employs the form factor described by expression 2.27. The simultaneous fitting of the form factor to the 40 measured scattering curves was performed by means of the method of least squares in the Fourier region (Pedersen, 1997). The calculated scattered intensity was modelled as the sum of the particle contributions and a two-component background $I_{\mathrm{BG}} = C_0 + C_4 q^{-\gamma}$. The parameters ρ_{core}, ρ_{shell}, R, R_{core} and γ were fitted simultaneously for all curves, whilst C_0 and C_4 were adjusted independently for each solvent density. A Gaussian size distribution was assumed. For the suspending medium electron density ρ_{solv} appearing in the contrast $\Delta\eta$, the value determined from the transmission measurement was used for each curve.

The obtained results are $R = (49.7 \pm 2.8)$ nm, $R_{\mathrm{core}} = (44.2 \pm 0.9)$ nm, $\rho_{\mathrm{core}} = (339.7 \pm 0.1)$ nm^{-3} and $\rho_{\mathrm{shell}} = (361.9 \pm 2.0)$ nm^{-3}, which represent the radial structure of a dense, thin shell surrounding a lighter core, as seen in the inset of figure 4.6. The resulting average electron density of the particle is $\rho_0 = (345.9 \pm 1.5)$ nm^{-3} and the polydispersity degree, $p_d = (22.8 \pm 6.0)$ %. The best fitting background corresponds to a value of $\gamma = 4.3 \pm 0.5$, close to the case $\gamma = 4$ originating from large impurities or precipitates (Pedersen, 1994). The fit uncertainty was calculated with a confidence interval of one standard deviation.

The different contributions to the uncertainty associated to the external radius of the particle R are detailed in table 4.1, where the uncertainties given are standard uncertainties ($k = 1$). Besides the fit uncertainty, the table summarizes the contributions from the energy resolution of the photon beam (Krumrey & Ulm, 2001), the accuracy of the distance between the irradiated sample and the scattering detector, the detector pixel size

Input quantity	u_I	u_r	**Contribution**
Photon energy	0.9 eV	10^{-4}	0.005 nm
Sample-detector distance	5 mm	10^{-3}	0.05 nm
Pixel size	0.2 mm	10^{-3}	0.05 nm
Centre determination	2 pixels	n.a.	0.5 nm
Core-shell fitting	2.8 nm	$6 \cdot 10^{-2}$	2.8 nm
Combined standard uncertainty			**2.8 nm**

Table 4.1 | Uncertainty contributions associated to the PS-COOH radius R determined by a a core-shell model fit, where u_I and u_r correspond to the input uncertainty and relative uncertainty respectively.

(Wernecke *et al.*, 2014) and the determination of the scattering centre. As in this case and in the examples appearing in chapter 5, the uncertainty is typically dominated by the contribution arising from the fitting procedure.

Besides, it is noticeable that the calculated electron density of the core coincides exactly with the theoretical polystyrene electron density, although the electron density of the shell is remarkably lower than the theoretical value of 383.4 nm^{-3} for PMMA (Ballauff, 2001). This might arise from the lower density of the monomers used in the particle synthesis (MAA and MMA), which could have mixed with the styrene monomers resulting in a less dense material than PMMA. This model might present some differences with the real colloid system, as a diffusive interfacial layer could be expected between polymer phases in colloids (Dingenouts *et al.*, 1994*a*), especially for incompatible polymers such as PMMA and PS. On the other hand, the large quantity of scattering curves used for the fitting process and, accordingly, the decreased uncertainty suggests that the chosen sharp core-shell model has a great resemblance to the real particle.

4.3.2 Isoscattering point

Although the first isoscattering point is clearly visible in figure 4.4, a model-free approach like the isoscattering point requires of a more precise determination of the position and a quantitative evaluation. For this purpose, the relative standard deviation σ_r of the 40 measured curves at each q is calculated according to

$$\sigma_r(q) = \frac{1}{\bar{I}(q)} \sqrt{\frac{\sum_{i=1}^{M} (I_i(q) - \bar{I}(q))^2}{M-1}}, \tag{4.2}$$

where $\bar{I}(q)$ is the mean value of the intensity at q and M is the number of scattering curves. This value becomes minimal at an isoscattering point. In order to reduce the influence of outliers, a truncated mean value was utilized, disregarding the 10 % most dispersed data points. In figure 4.7a, the relative standard deviation is plotted as a function of the momentum transfer q, which shows several distinguishable minima corresponding to isoscattering points.

A precise determination of the isoscattering point positions is performed by fitting Lorentzian functions to the minima in the relative standard deviation plot, which allows the calculation of the model-free external radius of the particle by means of equation 2.30. The results are presented in table 4.7b together with their associated uncertainties calculated according to the uncertainty budget presented in table 4.2. The sources contributing to the uncertainty associated to the position of $q^\star$ are similar to those reviewed in table 4.1 for the core-shell fit. In addition, the chosen q-bin size and the correction of the background contributions from the solvent are also considered. The diffuseness of the isoscattering point is quantified by computing the width of the momentum transfer (Δq)

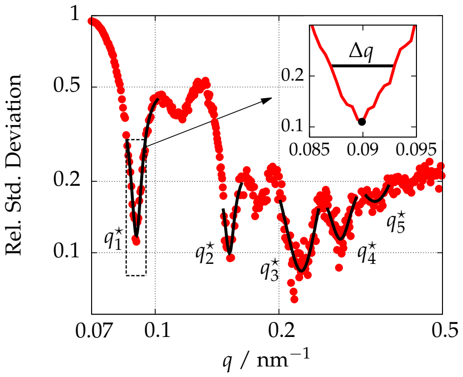

(a) Relative standard deviation

*Δq at $2\sigma_{\text{rel}}(q^\star)$ can not be computed.

	$q^\star$ (nm^{-1})	R (nm)	u_c (nm)
$q_1^\star$	0.090 ± 0.006	49.9	3.3
$q_2^\star$	0.152 ± 0.013	51.0	4.4
$q_3^\star$	0.23 ± 0.05	48.1	9.5
$q_4^\star$	0.28 ± 0.07	49.9	12.4
$q_5^\star$	0.34	50.3	*

(b) Isoscattering point positions

Figure 4.7 | Isoscattering points of the PS-COOH particles: a) Relative standard deviation of the scattering curves as a function of the momentum transfer. The labelled minima correspond to the first five isoscattering point positions calculated by fitting a Lorentzian function (black line). In the inset, the width Δq of the first minimum at a value of $2\sigma_{\text{rel}}(q^\star) = 0.22$ is depicted, which quantifies the diffuseness of $q_1^\star$ due to polydispersity effects or deviations from the spherical shape. b) Experimentally determined position of the first five isoscattering points and the corresponding external particle radius R. The combined standard uncertainty u_c associated to the radius is calculated according to table 4.2, where the diffuseness of $q^\star$ provides the larger contribution.

at a relative standard deviation value two times larger than the value at the minimum ($\sigma_{\text{rel}}(q^\star)$), as depicted in the inset of figure 4.7a. The width Δq gives an estimation of the uncertainty associated to the diffuseness of $q^\star$ introduced in section 2.3.1 related to the non-ideality of the particles, i.e. their polydispersity or the deviation of the particle shape from the spherical model. As observed in the uncertainty calculation associated to the $q_1^\star$ position in table 4.2, the diffuseness of $q^\star$ is the largest contribution to the combined standard uncertainty.

The obtained particle radii displayed in table 4.7b vary in the range from 48.1 nm to 51.0 nm, although as predicted by Kawaguchi & Hamanaka (1992) for a polydisperse system, the isoscattering points get smeared out for larger q-values and the precision decreases, simultaneously with the increase of the solvent background at higher q-values. This can be directly observed in the quality of the experimental data, as the first two minima are

Table 4.2 | Uncertainty contributions associated to the first isoscattering point $q_1^\star$ position. The main contribution arises from the diffuseness of $q^\star$ which is quantified by calculating the width Δq at a value of $2\sigma_{\text{rel}}(q^\star)$. The uncertainty associated to R is derived from the expression 2.30, which preserves the relative uncertainty of $q^\star$ and R.

Input quantity	u_I	u_r	**Contribution**
Photon energy	0.9 eV	10^{-4}	0.000009 nm^{-1}
Sample-detector distance	5 mm	10^{-3}	0.00009 nm^{-1}
Pixel size	0.2 mm	10^{-3}	0.00009 nm^{-1}
Centre determination	2 pixels	n.a.	0.0009 nm^{-1}
q-bin size	0.0017 nm^{-1}	$2 \cdot 10^{-2}$	0.0017 nm^{-1}
Solvent background	0.0015 nm^{-1}	$2 \cdot 10^{-2}$	0.0015 nm^{-1}
Diffuseness of $q^\star$ (Δq)	0.006 nm^{-1}	$7 \cdot 10^{-2}$	0.006 nm^{-1}
Combined standard uncertainty of $q^\star$		$7 \cdot 10^{-2}$	**0.006 nm^{-1}**
Combined standard uncertainty of R		$7 \cdot 10^{-2}$	**3.3 nm**

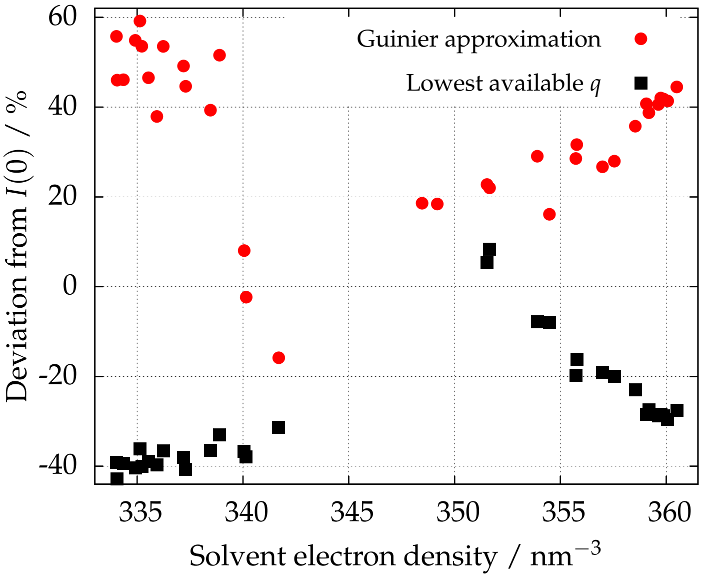

Figure 4.8 | Deviation from the $I(0)$ values used in the data evaluation: The Guinier approximation overestimates the experimental values, while the intensity at $q = 0.03$ nm^{-1} underestimates the zero-angle intensity.

clearly more pronounced and have smaller uncertainties than the subsequent minima, which appear smeared out. For instance, the isoscattering point $q_5^\star$ is already too weak for an accurate evaluation and the third minimum shows two remarkably close smaller minima which might affect the shape of the function. Therefore, $q_1^\star$ and $q_2^\star$ yield the most reliable values for evaluating the external radius of the particles. The weighted average value derived from the first two isoscattering points $R = (50.3 \pm 2.8)$ nm differs by only 1.2 % from the radius calculated from the model fit in the previous section.

Due to the existance of the isoscattering point diffuseness, a quantitative determination of the polydispersity of the suspended nanoparticles by means of the Lorentzian profile is rather challenging. Nevertheless, the narrow size distribution of the sample becomes clear by comparing the relative standard deviation values of the observed minima in figure 4.7a with a simulation using the structural parameters obtained in section 4.3.1. The value $\sigma_r(q_1^\star) = 0.11$ corresponds to a calculated ensemble polydispersity of 24 %. This value serves as an upper p_d limit due to the possible overestimation caused by the scattering contribution of the suspending medium.

4.3.3 Guinier region

By analysing the low q-region of the scattering curves, the so-called Guinier region, two important parameters can be obtained: the radius of gyration R_g related to the size of particle and the average electron density ρ_0 derived from the intensity at zero angle $I(0)$. According to Feigin & Svergun (1987), the fit of equation 2.34 to the Guinier region is mainly valid up to $qR_g < 1.3$. In this restricted q-range, too few data points are available for a reliable data analysis. Therefore, an extrapolation using the spherical form factor $F_{\text{sph}}(q, R)$ over the range available before the first minimum has been employed instead to obtain R_g and $I(0)$. This arises as a good choice because the Guinier approximation overestimates the values of the zero-angle intensity due to its limitation to monodisperse systems (Feigin & Svergun, 1987), as observed in figure 4.8. On the other hand, a more primitive approach, e.g. the intensity of the lowest accessible q-value ($q_{\text{min}} = 0.03$ nm^{-1}), underestimates the $I(0)$ values, because it neglects the extrapolation to $q \to 0$, as shown also in figure 4.8.

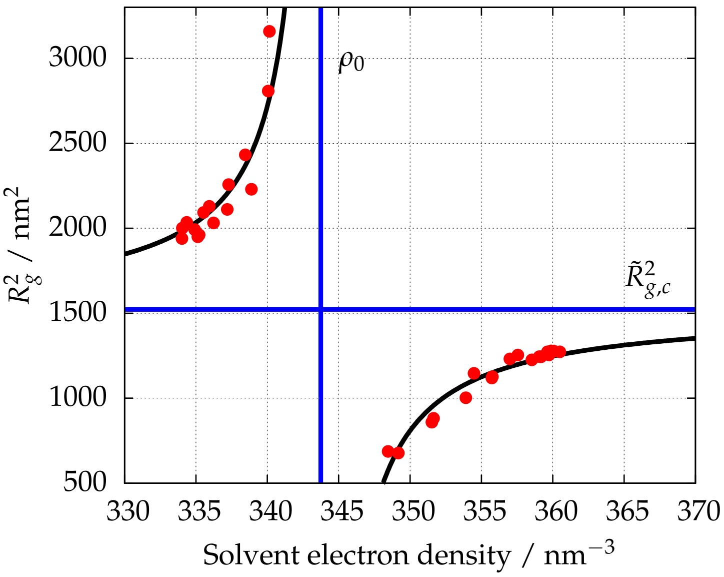

Figure 4.9 | Experimental squared radius of gyration as a function of the solvent electron density. Equation 2.35 is fitted to the data and shown as a thick line. The vertical and horizontal asymptotes correspond to ρ_0 and $\tilde{R}^2_{g,c}$ respectively.

As described in section 2.3.2, the radius of gyration of a heterogeneous particle in a contrast variation experiment should behave according to equation 2.35. In figure 4.9, the experimental squared radius of gyration is displayed as a function of the suspending medium electron density. The best fit to the measured data with values $\rho_0 = (343.7 \pm 1.5)$ nm^{-3}, $\tilde{R}_{g,c} = (39.0 \pm 5.2)$ nm, $\tilde{\alpha} = 4470$ nm^{-1} and $\tilde{\beta} = 0$ nm^{-4} is shown by the solid line. The uncertainty associated to the average electron density of the particle ρ_0 originates mainly from the beam size, as described in section 4.1.2. On the other hand, the uncertainty resulting from the fit of equation 2.34 is the dominant contribution to the radius uncertainty.

The positive value of $\tilde{\alpha}$ validates the hypothesis that a more dense polymer like PMMA surrounds a lighter core (PS) (Stuhrmann, 2008). The calculated average electron density of the particle ρ_0 suggests a very thin layer of PMMA shell around the PS core, due to the proximity of its value to the polystyrene electron density (339.7 nm^{-3}). The value of $\tilde{\beta} = 0$ proves a concentric model, where core and shell share the same centre. Using the same polydispersity value of 22.8 % obtained in the fitting process, the value for the particle shape radius of gyration results in $R_{g,c} = (36.9 \pm 4.9)$ nm and the external radius of the particle can be calculated assuming the particle as a spherical object. This calculation gives $R = (47.6 \pm 6.4)$ nm, which is only 2.1 nm smaller than the external radius $R = (49.7 \pm 2.8)$ nm calculated with the core-shell model fit, though it might be underestimated due to the choice of a possibly inflated polydispersity.

Average electron density

Using the same set of 40 scattering curves, the behaviour of the zero-angle intensity under the contrast variation is also investigated by fitting equation 2.36 to the experimental $I(0)$, as depicted in figure 4.10. A minimum in the curve is observed at $\rho_{\text{solv}} = (346.0 \pm 1.5)$ nm^{-3}, which corresponds to the value of the average electron density of the particle. This value is in very good agreement with the result obtained by fitting the core-shell form factor of $\rho_0 = (345.9 \pm 1.5)$ nm^{-3}. It is also noticeable that the minimum intensity is approximately 0, which means that the effective average density of the ensemble $\tilde{\rho}_0$ is equal to the average density of the particle ρ_0 (Avdeev, 2007). This result further

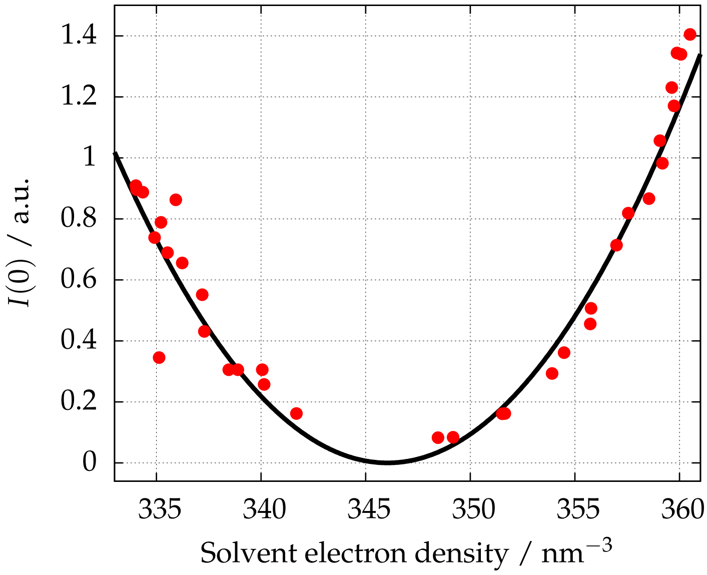

Figure 4.10 | Experimental zero-angle intensity as a function of the solvent electron density. The function corresponding to equation 2.36 is fitted to the data and shown as a thick line. The minimum in the parabola corresponds to $\rho_{\text{solv}} = \rho_0$.

legitimates the assumption made previously in section 4.2 about the PS-COOH particles that the ratio between the particle components' volumes is constant independent of the polydispersity and hence $\tilde{\rho}_0 = \rho_0$, i.e. the average density of the particle is not altered by the size polydispersity.

4.3.4 Consistency of the results

Table 4.3 summarizes the results of all three presented methods. From the first two isoscattering points, a value for the external radius of (50.3 ± 2.8) nm and an upper bound to the polydispersity degree have been derived. Focusing on the Guinier region of the scattering curves, a value for the average electron density of the particles ρ_0 is found using the radius of gyration ((343.7 ± 1.5) nm^{-3}) as well as the zero-angle intensity ((346.0 ± 1.5) nm^{-3}), the values of which differ by 2.3 nm^{-3} and lie within their confidence intervals. By fitting a core-shell model, an external radius of $R = (49.7 \pm 2.8)$ nm and an average electron density $\rho_0 = (345.9 \pm 1.5)$ nm^{-3} have been obtained, which are in considerable agreement with the previous results. In fact, the values of R and ρ_0 determined by different methods agree with each other within their stated confidence ranges.

From the results presented in table 4.3, the radius of gyration interpretation produces the most deviant values and the largest uncertainties. This might be founded in the complicated function fitted to the data and the reduced availability of q-range employed to obtain R_g. The resulting polydispersity degree of the measured particles from the model fit is in agreement with the upper limit obtained with the radii of gyration. Nevertheless the polydispersity is the parameter determined with the largest uncertainty in the fitting process and therefore this result must be considered with care.

It can be concluded that the different approaches show consistent and complementary results about the size distribution of nanoparticles with radial inner structure, especially for the external radius of the particle and its average electron density. A precise value for the polydispersity degree could not be obtained as explained previously, although a credible upper limit to the polydispersity degree of 24 % could be given.

Table 4.3 | Comparison of the results obtained by the different approaches presented in section 4.3 to evaluate contrast variation SAXS data.

	R (nm)	ρ_0 (nm^{-3})	p_d (%)
Core-shell fitting	49.7±2.8	345.9±1.5	22.8±6.0
Isoscattering point	50.3±2.8*	-	< 24
Radius of gyration	47.6±6.4**	343.7±1.5	-
Zero-angle intensity	-	346.0±1.5	-

*Weighted average value of $q_1^\star$ and $q_2^\star$

**Using the polydispersity degree from the core-shell model fitting

4.4 Applicability and comparison with other contrast variation approaches

The accessible electron density range defines the possible applications of the proposed technique and is consequently the most decisive factor to choose the contrast agent. With saccharides like sucrose or fructose, high concentrated mixtures with low viscosity can be achieved, reaching electron densities up to 400 nm^{-3}. Sugars are suitable for contrast variation experiments with bio-materials and polymeric nanoparticles, whose densities typically range between 0.9 and 1.4 g cm^{-3} (from 300 to 450 nm^{-3}). On the other hand, contrast agents like ethanol can reduce the electron density of the suspending medium until 270 nm^{-3} and, besides, is perfectly miscible with water. A wide variety of biological particles exist within the available density range achieved between ethanol and sugar.

More dense solutions prepared with heavy salts (e.g. sodium polytungstate (SPT)) could be an alternative for heavier particles e.g. silica, similarly to the application in sink-float analysis and density gradient centrifugation (Rhodes & Miles, 1991; Mitchell & Heckert, 2010). Nevertheless, the salt can compromise the stability of the particles inducing aggregation and lead to more complicated handling of the sample due to a decreased diffusion timescale. The chemical stability of the suspension is a crucial parameter that depends specifically on the investigated sample, but in general neutral contrast agents like sugars are preferred to salts.

Another relevant characteristic of the contrast agents is its scattering contribution to the background. Generally, the background scattering of the suspending medium is directly proportional to the contrast agent concentration and can affect notably the scattering data at the Fourier region, as observed in this chapter. Besides, the size of the diffusing molecule relates to the background intensity, where larger molecules like sucrose (ca. 342 g mol^{-1}) have a higher scattering power than smaller ones like fructose (180 g mol^{-1}) at the same mass fraction. Therefore, a compromise is required between the size of the contrast agent molecule, its solubility in an aqueous medium and the diffusion timescale of the solute.

In addition to solvent contrast variation in SAXS, other possible methods that vary the contrast of a single medium have already been proposed. Contrast variation in SANS is the most widespread technique (Ballauff, 2011, 2001), reaching high contrasts between sample and medium through the opportune substitution of hydrogen atoms by deuterium atoms. Typically, the scattering length density of the medium is changed by the appropriate mixture of water and deuterated water, although the scattering density of polymeric particles can also be modified by substituting a polymeric species by its deuterated equivalent (Rosenfeldt *et al.*, 2002). The contrast range achieved with this technique is much broader than that possible with SAXS, but the intrinsic experimental difficulties of neutron scattering experiments limit its usage to specific sample systems.

Other approaches to contrast variation in X-ray scattering are based on the anomalous behaviour of the atomic scattering amplitude near an absorption edge of an element contained in the sample or in the medium. Anomalous SAXS (ASAXS) has been a well-known technique in material science since its introduction by Stuhrmann in 1985 (Stuhrmann, 1985) and has been applied to a variety of colloids and polyelectrolytes at the hard X-ray region (Goerigk *et al.*, 2003; Stuhrmann, 2007; Lages *et al.*, 2013). The recently introduced Resonant Soft X-ray Scattering (RSoXS) method aims for absorption edges at much lower energies than ASAXS, like the so-called *water window* below 530 eV. By focusing the photon beam into a micrometric spot, the polymeric components of latex nanoparticles could be characterized due to their different chemical bond sensitivity near the carbon K-edge (around 285 eV) (Mitchell *et al.*, 2006; Araki *et al.*, 2006). The application of these techniques require of a sample system specially tailored for the experimental needs, where the probed atomic element is found in high concentrations. Besides, technical difficulties are also present, like the need for very thin sample thicknesses in RSoXS or the high monochromacy of the hard X-ray photon beam required in ASAXS.

Although the contrast variation approach presented in this work presents certain limitations, it shows evident advantages with respect to the other existing contrast variation techniques. For instance, solvent contrast variation is not element specific and the photon energy can be selected more freely, within the restrictions arising from the sample attenuation described previously. Moreover, the investigated particles can be used without any chemical treatment, unlike deuteration in SANS or atomic labelling in ASAXS. On the other side, the accessible density range of the contrast agent reduces the employment of the technique to relatively low density particles.

4.4.1 Other possible applications of the density gradient capillary

The diffusion time of a particle depends mainly on its size, as described by the Stokes-Einstein expression of the diffusion constant (Einstein, 1905):

$$D = \frac{K_B T}{6\pi\eta}\frac{1}{R} \tag{4.3}$$

where K_B is the Boltzmann constant, T is the solvent temperature, η is the dynamic viscosity and R is the radius of the particle. For example, the small size of ions (below 200 pm) decreases the diffusion timescale in a factor 5 in comparison with a disaccharide molecule like sucrose. On the opposite side, colloids can be considered diffusive agents which multiply the diffusion time up to 100 times.

In figure 4.11, the calibrated transmittance of a density gradient capillary of aqueous 12 nm silica nanoparticles (Ludox HS40, Sigma-Aldrich, Missouri, USA) is depicted, where the particle concentration is a function of the capillary height. The slower evolution of the concentration gradient compared with sucrose in figure 4.2 and the large density difference between water and the high concentrated particle suspension (ca. 1.3 g cm^{-3}) can improve the quality of the X-ray transmission data and provide an alternative application of the *density gradient* technique in SAXS, where the diffusive agent is the investigated object. Moreover, table-top X-ray sources can be an alternative to high photon flux synchrotron radiation sources due to the extended experimental timescale achieved when

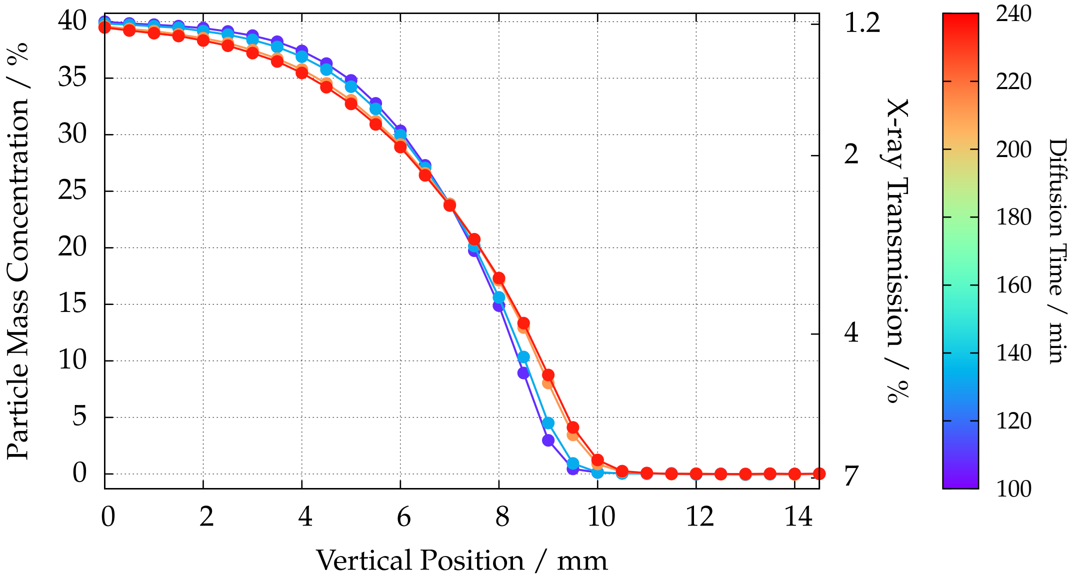

Figure 4.11 | Concentration gradient of 12 nm silica particles measured at 8000 eV. The large size of the colloids in comparison to a saccharide molecule provides a longer diffusion time than a typical contrast agent like sucrose.

using colloids as diffusing agent.

A colloidal concentration gradient as presented in figure 4.11 can be used to study the effects of concentration on the diffusion constant of the particles or investigate the type of inter-particle interactions as a function of the colloidal concentration. For example, standard dilution series can be performed *in situ* with this approach or examine the crystallization of the particles under gravitational forces (Hellsing *et al.*, 2012).

5

Simultaneous size and density determination of polymeric colloids

The current advances in nanomaterial development for medical applications are focused towards tailoring polymeric nano-drug carriers with flexible surface functionalisation and controlled morphologies (Euliss *et al.*, 2006; Yang *et al.*, 2005). Size and shape, combined with the choice of polymer and the mechanical properties, are fundamental and defining aspects of the particle functions, e.g. their *in-vivo* biodistribution (Vittaz *et al.*, 1996; Mitragotri & Lahann, 2009; Doshi & Mitragotri, 2009) or their drug-delivery efficacy (Powers *et al.*, 2006). Therefore, a full and consistent characterization of all properties of nanoparticles is of crucial importance and must be carefully adressed, especially for polymeric NPs due to their typical complicate internal structure.

This chapter demonstrates the simultaneous size and density determination using continuous contrast variation technique in SAXS with 3 polymeric particles of different sizes and polymeric species. By means of an aqueous sucrose density gradient, the measurements were achieved along a large range of suspending medium densities, from water density to that of poly(methyl methacrylate)'s, highlighting the relevance of the technique across a wide spectrum of polymers.

The applicability of this method for the traceable size determination of these colloids is discussed in this chapter, where a high-resolution size distribution of the particles is presented. Focusing on a low-density colloid, different evaluation approaches to SAXS contrast variation experiments are discussed and the advantages and drawbacks of a model-free formulation like the isoscattering point position are discussed, together with the accuracy of the shape scattering function. In addition, a form factor model is fitted to the scattering curves to obtain decisive information about the internal morphology of the particle, which is not directly available by other techniques such as transmission scanning electron microscopy (TSEM), differential centrifugal sedimentation (DCS) (Fielding *et al.*, 2012) or atomic force microscopy (AFM).

Besides, the ability of this technique to determine the density of polymeric colloids in suspension is also discussed. Normally, the density of the suspended particles can not be compared to the bulk density of the dry material. Such a complex question has been addressed by different methods, though with evident limitations. For example, the density of polymeric beads has been measured previously with field-flow fractionation (FFF) with high-accuracy but at the expense of *a priori* assumptions about the morphology of the particle (Giddings *et al.*, 1981; Yang *et al.*, 1983; Caldwell *et al.*, 1986). Another method which requires of previous knowledge about the size of the particle is isopycnic centrifugation, widely used in biology (Vauthier *et al.*, 1999). Assuming the Stokes' diameter as the actual size of the colloid, recent advances in analytical ultracentrifugation allow the complementary characterization of the size, density and molecular weight of gold nanoparticles (Carney *et al.*, 2011).

The density of the 3 polymeric colloids was also analysed by DCS and the results compared and discussed with those obtained by SAXS. DCS uses the sedimentation of particles through a density gradient to measure high resolution particle size distributions (Minelli *et al.*, 2014). Its accuracy typically depends on the knowledge of the density of the particles. When the size of the particle is known, DCS can alternatively be used to measure average particle's density.

In this study, the size and density of low-density particles is independently determined by performing DCS measurements with two different discs using the sedimentation and flotation respectively of the particles through a density gradient and solving the relative Stokes' equations. A similar approach to DCS which combines the results of two independent measurements has been investigated previously. For example, Neumann *et al.* (2013) used two sucrose gradients resulting in different viscosities and densities, where the altered settling velocity combined with linear regression analysis was used for the calculation of the size and density of silica nanoparticles and viruses. Bell *et al.* (2012) adopted a two gradient method based on the variation of the sucrose concentration to determine the density of the Stöber silica and the calibration standards used in DCS. Parts of this chapter have been adapted from an article published previously (Garcia-Diez *et al.*, 2016*b*).

5.1 Materials and methods

In this section, a detailed description of the polymeric nanoparticles employed in the experiments is presented. The experimental procedure of the continuous contrast variation technique is thoroughly discussed already in chapter 4, thus the focus of the section lies only on the DCS technique. Special interest is put on the description of the combined DCS approach based on the floating-sedimentation principle.

5.1.1 Polymeric particles

The experiments were performed using 3 different types of polymeric nanoparticles, whose diameters range from 100 nm to around 187 nm. Carboxylated poly(methyl methacrylate) colloids (PMMA-COOH) with a nominal diameter of 187 nm and plain polystyrene particles (PS-Plain) polymerized with < 1 wt% of a surface-active co-monomer with a nominal diameter of 147 nm were purchased from Microparticles (Berlin, Germany). The PS-COOH particles are described in detail in chapter 4 and are composed of a PS core surrounded by a PMMA shell. The phyisical densities of the NPs range from that of PS (1.05 g cm^{-3}) until PMMA's, which has a density of ca. 1.18 g cm^{-3}.

For the preparation of the high density aqueous sucrose solutions employed in the density gradient capillaries, the suspended colloids were mixed with a sucrose mass

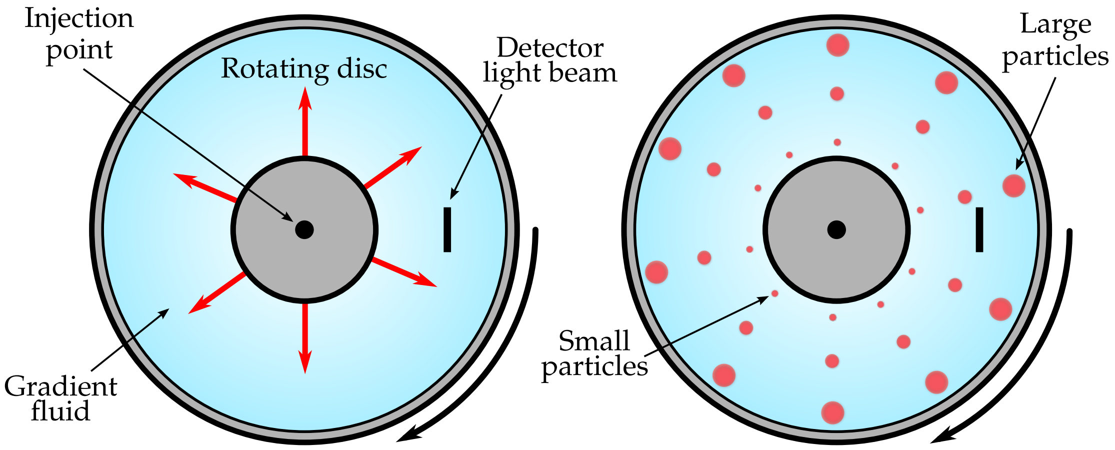

(a) DCS setup at the initial time **(b)** Size fractionation after a time t

Figure 5.1 | Scheme of the differential centrifugal sedimentation technique. a) A DCS setup consists of a disc rotating with a speed Ω filled with a gradient liquid with average density ρ_f. At a certain distance of the point where the particles are injected, the attenuation of the light beam is measured. b) After a time t, the particles are separated due to the centrifugal force depending on their size, where larger particles are detected earlier than smaller ones.

fraction of 21.2 %, 42.5 % and 13.4 % for the PS-COOH, PMMA-COOH and PS-Plain particles respectively.

5.1.2 Differential Centrifugal Sedimentation

The Differential Centrifugal Sedimentation (DCS) technique is based on the fractionation of particles in suspension by centrifugal sedimentation within a rotating, optically clear disc containing a liquid medium with a density gradient, as depicted in figure 5.1a. The time needed by the particles to reach the detector light beam at the edge of the disc depends on their properties (e.g. size and shape) and can be converted into a particle size distribution, as schematically presented in figure 5.1b. Particles with densities lower or similar to water's can be measured in a more dense liquid medium within the centrifuge by focusing on their buoyancy and observing how they float toward the fluid surface.

DCS measurements were performed by the National Physical Laboratory (NPL, Teddington, UK) with a CPS DC20000 instrument (CPS Instruments, Prairieville, LA, USA) upgraded to DC24000 for the PS-Plain particles measurements. The radial position of the detector was measured by injecting 100 μL aliquots of water into the spinning disc initially empty until the accumulation of water produced a response in the detector. For the density gradient formation, the disc was filled with 14.4 mL of a sucrose (Amresco LLC, OH, USA) solution topped with 0.5 mL of dodecane to prevent evaporation. The detailed information of the gradients is summarised in table 5.1. Measurements of the PS-COOH and PMMA-COOH particles at 0.05 % w/v concentration were performed in triplicate. The measurements of the PS-Plain particles were repeated seven times for each setup. Injection volumes were 100 μL.

The measured attenuation at 405 nm was converted to the number of particles for each measured diameter by treating the particles as spherical Mie scatterers with no optical absorbance at the incident wavelength. Three different types of calibration particles were used: poly(vinyl chloride) colloids in water with density of 1.385 g cm^{-3} and nominal size

Table 5.1 | Parameters of the different DCS setups: composition of the sucrose gradients, average density of the gradients ρ_f, rotation speed of the centrifuge Ω and type of calibrant.

	Sucrose concentration (w/w)	ρ_f (g cm^{-3})	Ω (rpm)	Calibrant
PS-COOH	from 2 % to 8 % in H_20	1.013	$2.0{\cdot}10^4$	A
PMMA-COOH	from 4 % to 12 % in H_20	1.025	$2.0{\cdot}10^4$	B
PS-Plain	from 2 % to 8 % in H_20	1.013	$2.4{\cdot}10^4$	B
PS-Plain*	from 4 % to 12 % in D_20	1.140	$2.4{\cdot}10^4$	C

*Low density disc

of (223 ± 5) nm (calibrant A) and (239 ± 5) nm (calibrant B) and polybutadiene colloids in 16 % sucrose mass fraction in heavy water with nominal size of (510 ± 20) nm and density of 0.91 g cm^{-3} (calibrant C).

A standard disc configuration where the particles sediment through a lower density gradient was used and additionally, a more recently developed setup which makes use of a disc where colloids float through a higher density gradient was also used for the PS-Plain colloids due to their low density (Fitzpatrick, 1998). Typically, the DCS diameter D_p or density ρ_p of a spherical particle is derived from the Stokes' law:

$$D_p = \sqrt{\frac{18\eta \ln {}^{R_f}/_{R_i}}{\left(\rho_p - \rho_{\text{fluid}}\right) \omega^2 t_p}} \tag{5.1}$$

where t_p is the sedimentation time between radii of rotation R_f and R_i of the particle, η and ρ_f are the viscosity and the density of the fluid respectively and ω is the disc angular frequency. If a calibrant of known diameter D_c and density ρ_c is measured with the same setup, the investigated particle diameter can be expressed as:

$$D_p = D_c \sqrt{\frac{\left(\rho_c - \rho_{\text{fluid}}\right) t_c}{\left(\rho_p - \rho_{\text{fluid}}\right) t_p}} \tag{5.2}$$

By using the combination of DCS measurements performed in two different fluids, one with density ρ_L and one with higher density ρ_H, the values of D_p and ρ_p can be independently found by solving analytically the following system of equations:

$$\boldsymbol{D_p} = D_{cH} \sqrt{\frac{\left(\rho_{cH} - \rho_H\right) t_{cH}}{\left(\boldsymbol{\rho_p} - \rho_H\right) t_{pH}}} = D_{cL} \sqrt{\frac{\left(\rho_{cL} - \rho_L\right) t_{cL}}{\left(\boldsymbol{\rho_p} - \rho_L\right) t_{pL}}} \tag{5.3}$$

where cH and cL denote the calibrants used with high and low density fluids respectively and t_{pH} and t_{pL} are the sedimentation times of the particles measured in the high and low density fluids respectively. The measurement uncertanties given in the text include both statistical and systematic uncertainty propagated from Stokes' equations.

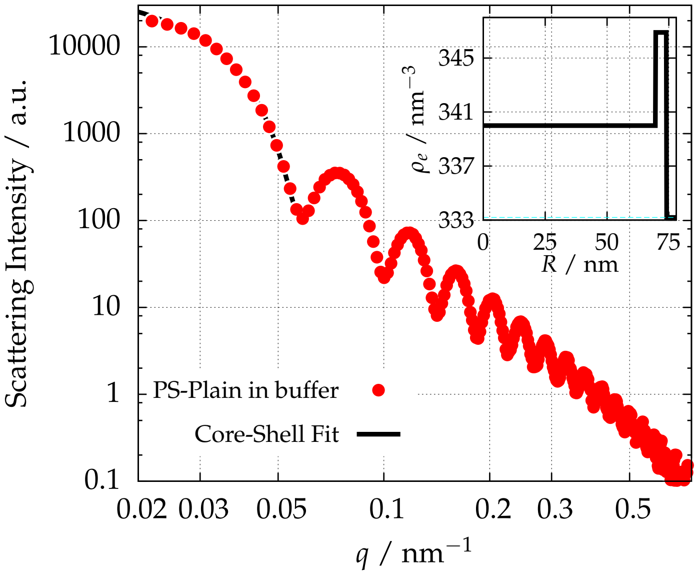

Figure 5.2 | Scattering curve of the PS-Plain particles in buffer: A core–shell fit to the experimental scattering curve is presented. In the inset, the electron density radial profile of this fit is shown, assuming the core is polystyrene with a density of 339.7 nm^{-3}.

5.2 Determination of the particle size distribution

In figure 5.2, the SAXS curve of the PS-Plain particles in buffer at a single-contrast is shown. The large number of minima observed in the curve is remarkable and indicates the high monodispersity of the sample, which allows a traceable size determination of these colloids.

Upon trying different form factor fits detailed in section 2.2, a simple core-shell structure with a sharp interface (eq. 2.27) was found to be the most suitable, suggesting a heterogeneous structure which is eluded by other characterization techniques, e.g. microscopy. The obtained particle diameter was (147.0 ± 4.7) nm, where the fit uncertainty was calculated with a confidence level of one standard deviation ($k = 1$) by examining the change in χ^2 when varying the diameter. The radial electron density profile of the core-shell fit is shown in the inset of figure 5.2, where a thin shell with high density surrounds a lighter core. This structure is likely due to the non-reacted monomers in the main matrix or the highly hydrophilic behaviour of the co-monomer, segregating polystyrene to the core.

The fit of the form factor 2.26 with 7 shells with a linear electron density gradient is in very good agreement with the experimental data as well and presents a χ^2 value 20 times lower than the compact spheres model fit. Although the calculated χ^2 value is very similar to that of the core-shell model and the radial electron density profile coincides qualitatively as well, the uniquess of the solution can be debated due to the large number of fit parameters (14). In case of coinciding results, the simpler core-shell model might solve the overfitting problem and appears as the best solution.

The morphology of the PS-Plain particles was further studied using the density gradient contrast variation technique described in chapter 4 by varying the suspending medium electron density from 333.2 to 350.2 nm^{-3}. By increasing the solvent contrast, the changes of the features in the scattering curves presented in figure 5.3a and the appearance of isoscattering points prove the multi-component composition of this colloid.

From the 40 experimental scattering curves shown in figure 5.3a, a model-free size determination can be performed by locating the isoscattering points I_i. This is achieved by calculating the relative standard deviation, as shown in figure 5.3b, where the minima

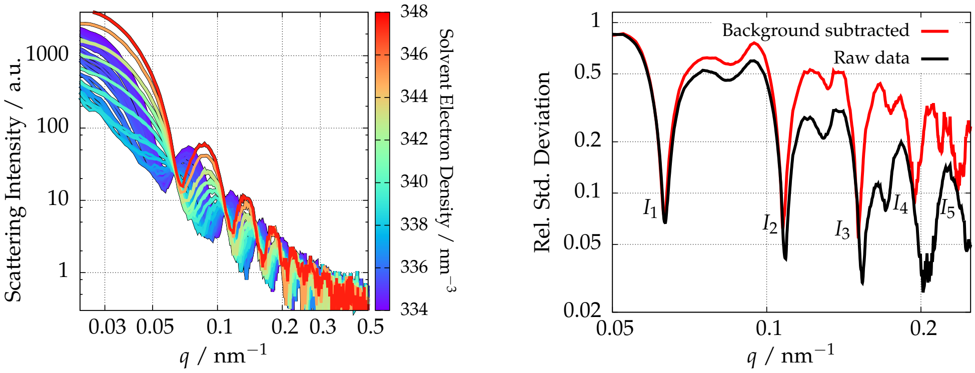

(a) Scattering curves **(b)** Isoscattering point positions

Figure 5.3 | Continuous contrast variation on the PS-Plain particles: a) SAXS curves of the PS-Plain particles obtained by density gradient contrast variation after solvent background subtraction. b) The relative standard deviation of each q calculated across all the measured scattering curves, where the minima correspond to the isoscattering points I_i. The background subtraction shifts the position of I_i, especially for high q-values.

Table 5.2 | Isoscattering points position and the corresponding particle diameter for the scattering curves before and after background correction. The diameter deviation between both values is also shown, with larger deviation for higher q-values. The uncertainty associated to the diameter is calculated as described in chapter 4.

	Raw data		Corrected data		Deviation
	$q^\star$ (nm^{-1})	Diameter (nm)	$q^\star$ (nm^{-1})	Diameter (nm)	nm
$q_1^\star$	0.063 ± 0.002	142.0 ± 5.4	0.063 ± 0.002	142.4 ± 5.6	0.4
$q_2^\star$	0.109 ± 0.003	142.0 ± 4.2	0.108 ± 0.003	143.6 ± 4.1	1.6
$q_3^\star$	0.154 ± 0.005	141.9 ± 4.6	0.151 ± 0.004	144.4 ± 3.7	2.5
$q_4^\star$	0.206 ± 0.016	136.6 ± 10.6	0.195 ± 0.011	144.3 ± 7.9	7.7

correspond to the fulfillment of the isoscattering condition expressed by equation 2.30.

Table 5.2 summarizes the particle diameters obtained from the first 4 isoscattering points (I_1 to I_4), which range between 142.4 and 144.4 nm after background correction. The precision of the isoscattering point determination decreases for increasing q as described by Kawaguchi & Hamanaka (1992) and it is exemplified by the broadening of the minima for higher q and the increase of the associated uncertainties, as discussed previously in chapter 4. As observed in figure 5.3b, the effect of the solvent background is relevant principally at high q-values as well. These effects are studied in more detail in section 5.3.2.

The data can also be analysed by using the *shape scattering function* described in section 2.3.2. The shape scattering function describes the external shape of the particle independently of its inner structure and is an appropriate approach for the PS-Plain colloid, because it enables the size distribution determination of the particles avoiding any *a priori* consideration about the particle composition.

The experimental shape scattering function is calculated from the measured scattering curves presented in figure 5.3a. The result is depicted in figure 5.4 together with the spherical model fitted to the data, which employs a simple form factor that ignores the internal structure (eq. 2.24) and a gaussian size distribution expressed by equation 2.21. From this fit, a mean particle size of (146.8 ± 1.3) nm was determined. The associated

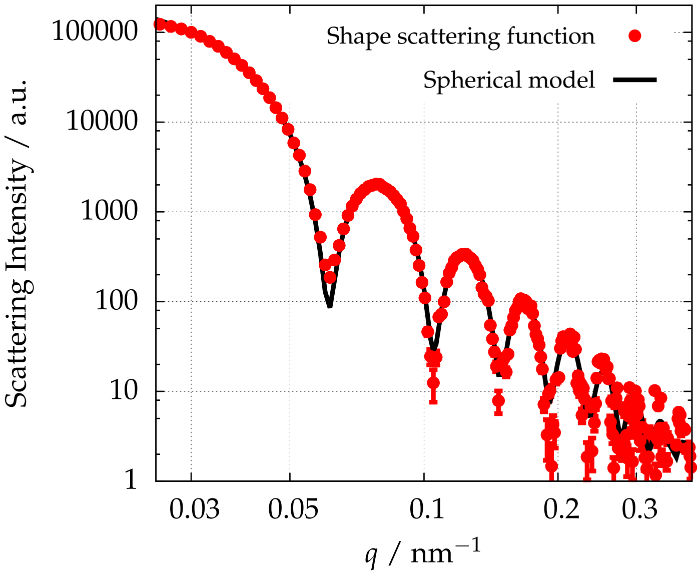

Figure 5.4 | Experimental shape scattering function of the PS-Plain particles calculated from 40 scattering curves and the spherical form factor fitted to the calculated shape scattering function.

uncertainty calculated with this approach is 3.5 times smaller than the one obtained with the single-contrast SAXS experiment. By fitting the ellipsoid model given by expression 2.25 to the shape scattering function, a sphericity of 98 % was obtained.

5.2.1 Inter-laboratory comparison of the mean particle diameter

The improvement in the size accuracy with the shape scattering function approach is summarized in figure 5.5, where the diameter of the PS-Plain particles determined by different techniques in an inter-laboratory study is also presented (Nicolet *et al.*, 2016).

The figure compares the PS-Plain diameter measured by the ensemble techniques SAXS and DCS and the imaging methods AFM and TSEM and presents the weighted mean value of all the results as a grey line, which corresponds to a diameter of 145.0 nm with an associated expanded uncertainty ($k = 2$) of 1.6 nm. The SAXS results tend to larger values when modelling the scattering form factor, whilst the diameter obtained from the isoscattering points positions I_i present values slightly smaller than the calculated mean value. However, the maximum deviation from the weighted mean is less than 2 %.

The DCS result is obtained by a combined analysis of two complementary centrifuge configurations as detailed in section 5.1.2, where figure 5.6 depicts the dependency of the measured particle diameter on the density values for the two setups. The two setups measure the same diameter and density at the crossing point of the data, which occurs for a diameter of (138.8 ± 5.8) nm and a density of (1.052 ± 0.010) g cm^{-3}. The measured diameter fits within its uncertainty in the confidence interval of one standard deviation of the inter-laboratory comparison.

All the techniques are in very good agreement, even considering that they are based on different physical principles. The improvement in accuracy for the size determination with SAXS by using the shape scattering function approach is further sustained by this comparison.

This improvement was confirmed by employing the same approach with the PS-COOH colloids. The diameter obtained from the core-shell model fit in chapter 4 is (99.4 ± 5.6) nm, while the value obtained from the shape scattering function calculation is (101.4 ± 2.4)

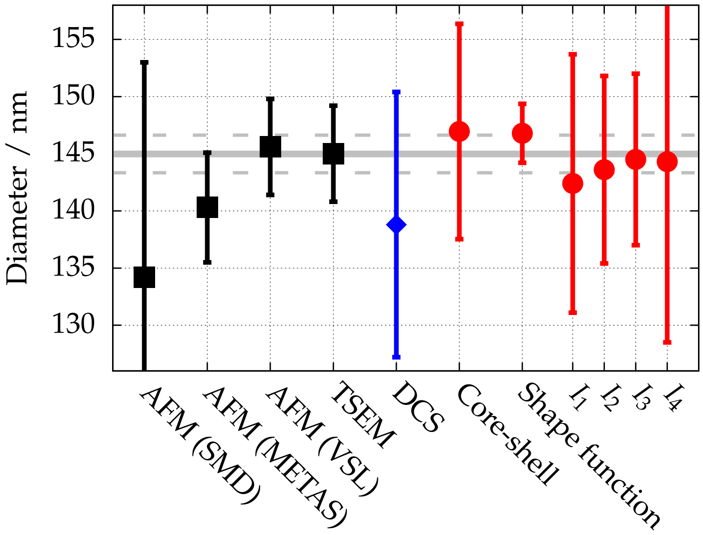

Figure 5.5 | Comparison of the PS-Plain average diameter obtained with different techniques, where the errorbars correspond to the expanded uncertainty ($k = 2$). The circles correspond to results obtained with SAXS in the FCM beamline and the diamond to combined DCS measurements performed by NPL. The gray line defines the weighted average value of all the results. The microscopy values are obtained from Belgian Service Métrologie-Metrologische Dienst (SMD), Swiss Federal Institute of Metrology (METAS) and Dutch Metrology Institute (VSL).

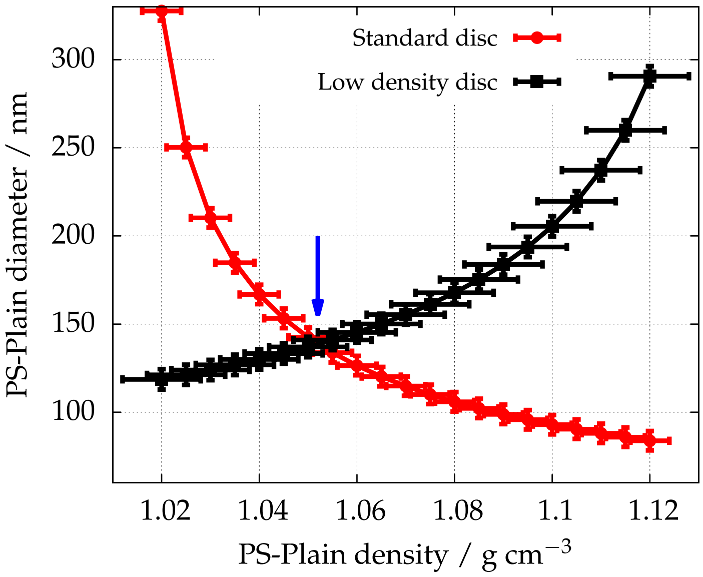

Figure 5.6 | Dependence of the intensity-based modal Stokes' diameter on the particle density for the PS-Plain particles analysed in H_2O-sucrose (black) and D_2O-sucrose (red) gradients. The arrow indicates the crossing point of the data, where the two setups measure the same diameter and density of the colloid. This occurs for a diameter of (138.8 ± 5.8) nm and a density of (1.052 ± 0.010) g cm^{-3}

	PS-Plain	PS-COOH
Core-shell fitting	147.0 ± 4.7 nm	99.4 ± 5.6 nm
Shape scattering function	146.8 ± 1.3 nm	101.4 ± 2.4 nm
First isoscattering point	142.4 ± 5.6 nm	99.8 ± 6.6 nm
Second isoscattering point	143.6 ± 4.1 nm	102.0 ± 8.8 nm

Table 5.3 | Comparison of the diameters of the PS-Plain and PS-COOH particles obtained by the different approaches described in section 5.2.

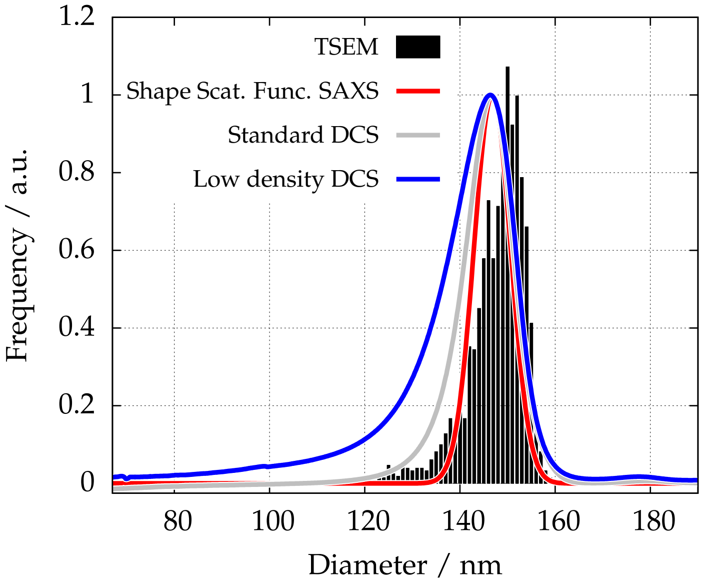

Figure 5.7 | Number-weighted size distribution of the PS-Plain particles measured by DCS, TSEM (Nicolet *et al.*, 2016) and SAXS with the shape scattering function approach.

nm. Again, the uncertainty associated to the size decreases by ~ 60 %, whilst it is still in accordance with the diameter obtained with the first two isoscattering points positions of 100.6 ± 5.6 nm. The diameters of the PS-Plain and PS-COOH particles obtained by the different approaches to contrast variation data are compared in table 5.3. In both examples, the smallest uncertainty is associated to the shape scattering function formalism, while the core-shell model and the position of the first two isoscattering points produce larger combined standard uncertainties.

The third polymeric particles used in the study are the PMMA-COOH colloids introduced in section 5.1. Due to the low polydispersity of these particles, a spherical form factor fit to the single-contrast scattering curve provides already a very accurate diameter of (186.5 ± 2.3) nm. In this case, contrast variation experiments in SAXS show no advantages because of the homogeneous composition of the particles. The application of the shape scattering function formalism or the isoscattering point approach is only feasible if the NPs possess an internal structure.

5.2.2 Particle size distribution of the PS-Plain particles

An important attribute of polymeric colloids is their polydispersity, as the suitability for specific applications depends on their spread in size. For example, colloids are known to induce different inflammatory responses depending on their size (Kusaka *et al.*, 2014).

The SAXS results determine a polydispersity degree p_d for the PS-Plain colloids of 6.1 %, which is an indicator of a very monodisperse distribution, as also suggested by the regular minima observed in figure 5.2. Particle polydispersities measured by DCS are also low as observed in figure 5.7, ranging from 7.8 % measured with the standard setup, to

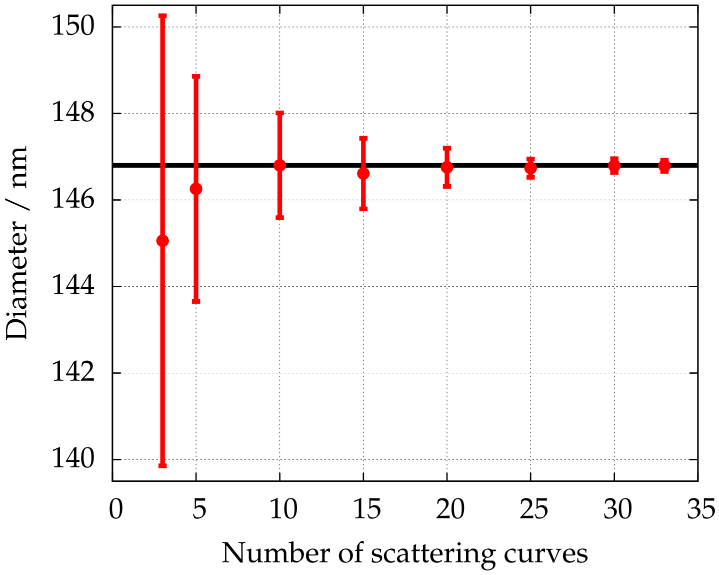

Figure 5.8 | Diameter of the PS-Plain particles as a function of the number of scattering curves used in the shape scattering function calculation. The horizontal line shows a diameter of 146.8 nm.

11.3 % measured with the low density disc setup. The standard setup appears therefore to achieve a higher resolution size distribution. The size distribution measured by TSEM with a p_d of 8.3 % shows good agreement with the ensemble techniques.

The measurements obtained by AFM provide polydispersity degrees larger than 10 % (Nicolet *et al.*, 2016) and, therefore, slightly broader size distributions than those calculated by SAXS, TSEM and standard DCS. This can be in part attributed to the low statistics that typically affect imaging methods, along with artefacts associated with the posterior analysis.

For instance, in the TSEM images (Nicolet *et al.*, 2016), smaller and larger populations with different contrasts have been observed which could affect the evaluation of the density measured by ensemble techniques in the following section 5.4, as the particle average density might vary. Indeed, when a bimodal distribution is used to analyse the SAXS shape scattering function of the PS-Plain particles, a second size population is found at 101 nm in agreement with TSEM, while the main mode maintains a p_d of ca. 5 %.

5.3 Considerations about scattering data evaluation

In the previous section, the mean diameter of polymeric nanoparticles was obtained using two different model-free approaches, i.e. the isoscattering point and the shape scattering function. The method employed to analyse the scattering curves measured with the continuous contrast variation technique in SAXS affects the size determination and its accuracy, as suggested by the results. Following, a discussion about both approaches is presented based on the scattering data shown in figure 5.3a.

5.3.1 Shape scattering function formalism

The shape scattering function obtained by density gradient contrast variation has been demonstrated as a powerful technique which can provide precise information about the size distribution and shape of the colloid by fitting a simple form factor.

However, an accurate determination of the suspending medium density for each scattering curve is required, due to the increased uncertainties (Lefebvre *et al.*, 2000) that can arise from the resolution of the system of linear equations described in section 2.3.2.

Besides, a minimum of 3 scattering curves measured at different contrasts is necessary to obtain the resonant term, although an increasing number improves the determination of the size distribution. This issue has been addressed with the experimental data of the PS-Plain colloids measured by the density gradient contrast variation. From the 40 experimental curves, only a limited number N was randomly selected to compute the shape scattering function, while this process was repeated 100 times. The mean diameter obtained from this data set and its statistical standard deviation are plotted in figure 5.8 as a function of N.

The effect of increasing the number of measured contrasts evidences that the result tends asymptotically to the value of 146.8 nm discussed in section 5.2 and the standard deviation of the 100 iterations decreases for large N, e.g. the associated uncertainty is reduced. This outcome emphasizes further the advantages of the continuous contrast variation technique due to the large number of scattering curves at different contrasts which can be easily measured.

In summary, it has been demonstrated that the possibility to determine the particle size distribution by the shape scattering function is a clear improvement to single-contrast SAXS techniques reducing relevantly the uncertainty, although an accurate determination of the contrast and a relatively high number of scattering curves are required.

5.3.2 Isoscattering point approach

The theory defines the isoscattering point $q^\star$ as a morphological parameter independent of the suspending medium density, which is a enormous practical advantage as it can be located without the proper calibration of the contrast. In cases where the composition of the buffer is unknown or the density of the solvent cannot be properly calibrated, the isoscattering point position can still be used to determine the size of the particles by calculating the relative standard deviation of all the measured scattering curves.

In order to obtain reliable results, a proper subtraction of the solvent scattering must be performed. It is clear in figure 5.3b that the correction of the solvent contribution to the scattering intensity plays an important role in the determination of the $q^\star$ values as the curve shifts to smaller q-values when subtracting the solvent background. Although this effect is larger at high q-values producing deviations up to 7.7 nm, the solvent background influences the position of all the isoscattering points as summarized in table 5.2.

It has been discussed before in this work that the polydispersity of the latex and its deviation from the spherical shape influence the position and diffuseness of $q^\star$, principally at high q-values. This can disturb the size determination for polymeric particles with broad size distributions and limit the applicability of this technique. In fact, the largest contribution to the uncertainty associated to the position of the isoscattering points originates from the diffuseness of $q^\star$ due to the deviation from ideality of the particle, as reviewed in chapter 4.

In order to prove the isoscattering point dependency on the particle polydispersity, the diameter obtained from the first isoscattering point position is simulated for three core-shell particle with different core-to-size ratios, as depicted in figure 5.9a. The deviation of the calculated size from the nominal size becomes larger for increasing particle polydispersities, reaching size deviations up to 8 % at $p_d = 30$ %. Moreover, the size

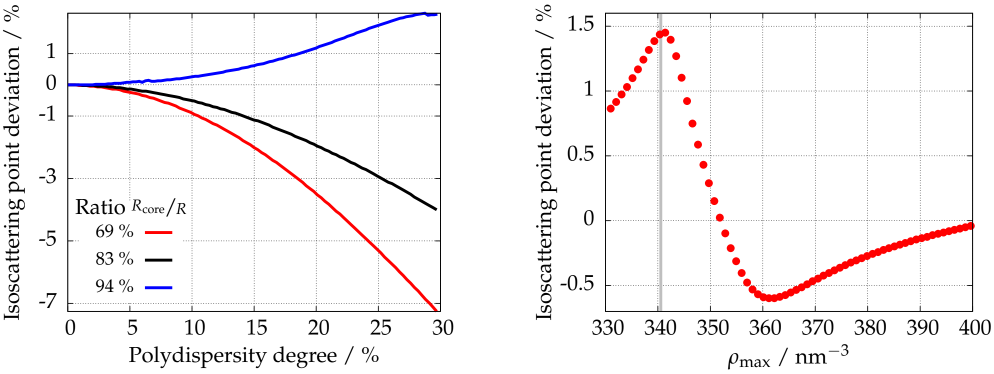

(a) Polydispersity effects

(b) Solvent electron density range

Figure 5.9 | Deviation of the size of the PS-Plain particles calculated using the $q_1^\star$ position from the nominal value depending on a) the size polydispersity of core-shell particles with different core-to-size ratios or b) the solvent electron density range employed in the experiment, where $\rho_e \in (330\ \mathrm{nm}^{-3}, \rho_{\mathrm{max}})$.

deviation behaves differently depending on the internal structure of the particle, tending to larger deviations for thicker shells and positive deviations for thinner ones.

This work demonstrates also that the $q^\star$ value determined with the previously described method depends on the range of solvent densities used in the contrast variation experiment. For this purpose, a contrast variation experiment with 10 different solvent densities was simulated for a polymeric particle with the morphology and size distribution obtained with the core-shell model in section 5.2. Using a lower bound to the contrast range close to the electron density of water ($\rho_{\mathrm{min}} = 330\ \mathrm{nm}^{-3}$) and increasing systematically the upper limit, it is shown in figure 5.9b that the calculated result deviates from the nominal value up to 1.5 %.

In this example, the largest deviations occur when the average density of the latex i.e. match point (depicted as a vertical line in figure 5.9b) is excluded from the experimental contrast range or when ρ_{max} is close to this matching density. This observation conflicts partly with the initial intuition that this technique is independent of the experimental procedure, although this problem can be avoided by selecting the solvent electron density range skillfully i.e. equidistantly distributed around the match point. This could be one explanation behind the slight size differences observed in figure 5.5 between the issocattering approach and the other SAXS results.

The isoscattering point approach to contrast variation SAXS data evaluation presents certain assets which can not be ignored. For instance, the independence of $q^\star$ from the sample contrast facilitates its easy application, although the solvent electron density range must be chosen with care and always around the average electron density of the particle to maximize its accuracy. On the other hand, the diffuseness of the isoscattering point position due to the polydispersity and ellipticity of the sample arises as an indisputable drawback and produces larger associated uncertainties than the shape scattering function approach.

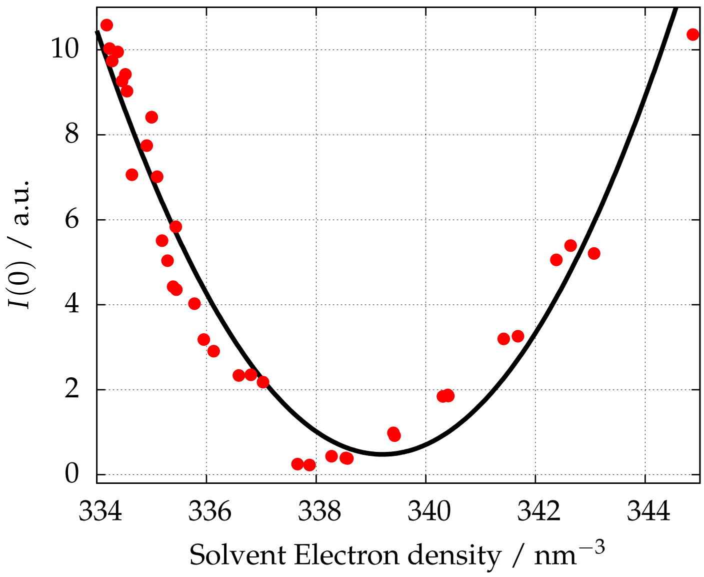

Figure 5.10 | Intensity at zero-angle of the PS-Plain particles as a function of the solvent electron density measured with continuous contrast variation in SAXS. The minimum defines the average electron density of the particle.

5.4 Determination of the particle mass density

In contrast variation SAXS, the solvent electron density which matches the average electron density of the particle ρ_0 corresponds to a minimum in the intensity of the scattering curve according to expression 2.36. In order to quantify the particle density, the scattering intensity of the PS-Plain particles at zero angle $I(0)$ is examined along the contrast range of the experiment as shown in figure 5.10. The value of $I(0)$ was determined by extrapolation to $q \to 0$ using a spherical form factor function fitted to the available range before the first minimum, as discussed in section 4.3.3. The parabolic fit to the data is plotted as a black line in figure 5.10 and results in $\rho_0 = (339.2 \pm 1.0)$ nm^{-3}, which is consistent with the tabulated value of dry bulk polystyrene 339.7 nm^{-3} (Dingenouts *et al.*, 1999).

The mass density of the particle can also be determined by this approach because the electron density is directly proportional to the mass density, as reviewed in chapter 2. A PS-Plain density of (1.043 ± 0.003) g cm^{-3} is obtained, although an assumption about the polymer (or monomer) components and their atomic structure is necessary for the calculation. Therefore, a typical value of $Z/A = 0.54$ was adopted for this conversion, where Z and A are the average atomic number and mass of the polymer respectively. This value is characteristic of polymers (or monomers) such as PS, PMMA or MMA, and very close to the Z/A ratio of MAA (0.53), polyvynil chloride (0.51) or polyethylene (0.57).

The density uncertainty is associated to the vertical size of the focused X-ray beam as discussed in 4.1.2, which typically corresponds to an associated uncertainty of 1 nm^{-1} or a relative uncertainty of around 3 %. Furthermore, the result can be affected by the polymeric composition of the colloid, and therefore, the assumption of Z/A, although an upper limit of 5 % is expected from this contribution.

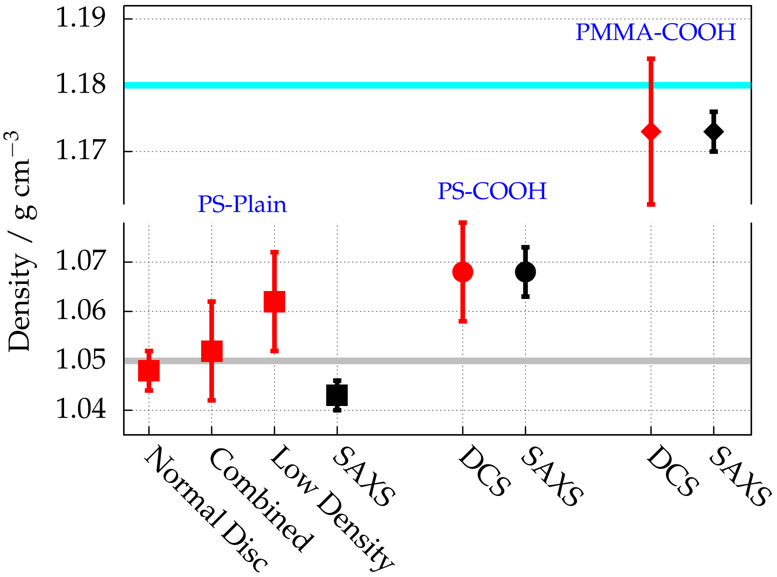

Figure 5.11 | Comparison between the mass densities of three polymeric colloids measured with SAXS using the $I(0)$ approach (black) and DCS (red): PS-Plain (squares), PS-COOH (circles) and PMMA-COOH (diamonds). The nominal densities of polystyrene (1.05 g cm^{-3}) and PMMA (1.18 g cm^{-3}) are also shown in the plot as horizontal lines (Dingenouts *et al.*, 1999).

5.4.1 Mass density of the PS-Plain particles: validation with DCS

In figure 5.11, the value measured with the $I(0)$ approach from the continuous contrast variation experiment is compared to the average density of the PS-Plain colloid measured with different DCS configurations. For the standard centrifuge setup and the low density disc configuration, the size value used for the density calculation was 147 nm, as measured by single-contrast SAXS, while combining the information from both setups allowed the measurement of the density independently of the particle diameter, as explained in section 5.2.1.

The results agree with each other within their stated measurement uncertainties, although DCS measurements exhibit slightly higher densities than SAXS. Typical causes of systematic uncertainties in DCS are the inaccuracy of the size and density of the calibration standard and the thermal variation in the centrifuge gradient during the measurements, which affect its viscosity and density (Kamiti *et al.*, 2012). A temperature variation within the gradient of about 7 °C before and after measurements was detected and a period of 30 min was considered appropriate to reach reliable thermal equilibrium. In the low density disc configuration, the determination of the average density of the D_20 sucrose gradient becomes an important source of uncertainty which might explain the larger associated uncertainty in comparison to the standard configuration. Besides, the normal disc setup shows a higher resolution size distribution as discussed in section 5.2.2 which also translates in smaller uncertainties associated to the mass density.

5.4.2 Density determination of heavier polymeric colloids

The applicability of the continuous contrast variation techniques is further discussed by comparing with DCS for higher-density polymeric colloids, as summarized in figure 5.11. The density of the PS-COOH particles derived from the $I(0)$ approach is in excellent agreement with that measured by DCS using a standard configuration and assuming a particle diameter of 99.4 nm, which was obtained by SAXS. Considering the similar electronic composition of these polymers and the average electron density of the particle $\rho_0 = (346.0 \pm 1.5)$ nm^{-3} obtained in chapter 4, an average mass density of the particles of (1.068 ± 0.005) g cm^{-3} can be calculated. These core-shell particles, more dense than polystyrene as detailed in section 4.3.1, illustrate the tendency during the emulsion polymerization to segregate polar and nonpolar components (Dingenouts *et al.*, 1994*c*).

Similarly, the density of the PMMA-COOH colloids was measured using the standard DCS setup and assuming a diameter of 186.5 nm, as measured by SAXS. This value is compared to the density of (1.173 ± 0.003) g cm^{-3} obtained by computing the intensity at zero-angle of a continuous contrast variation experiment with a minimum at (381.5 ± 1.0) nm^{-3}. Again, both techniques are in excellent agreement and reveal a mass density slightly lower than the expected PMMA density of 1.18 g cm^{-3} (Dingenouts *et al.*, 1999).

This result highlights the fact that the density of polymeric colloids in suspension may vary from that of bulk materials, for example dry particles. For instance, a volume variation can be expected when going from the MMA monomer to the polymer PMMA (Nichols & Flowers, 1950) which might reduce the colloid density.

6

Continuous contrast variation applied to relevant bio-materials

In the continuously growing world of nanotechnology, nanoscience provides understanding for biological structures at the nanometre length scale, such as lipoprotein biology, while the application of nanoparticles in medicine opens exciting new possibilities in this field (Nie *et al.*, 2007; Sahoo & Labhasetwar, 2003; Wickline & Lanza, 2003; Zhou *et al.*, 2014; Rosen & Abribat, 2005). For example, polymeric colloids and other biodegradable nanocarriers are finding many medical applications (Vicent & Duncan, 2006) and are starting to undergo clinical trials (Patel *et al.*, 2012; Beija *et al.*, 2012; Cabral & Kataoka, 2014).

In this sense, lipid vesicles, or liposomes, have an increasing importance in the emerging field of nanomedicine, due to their capacity to encapsulate hydrophilic compounds within the closed phospholipid bilayer membrane. In fact, liposomal nanocarriers are nowadays a widespread instrument for drug delivery (Pérez-Herrero & Fernández-Medarde, 2015), like the liposomal formulation of doxorubicin coated with polyethylene glycol (PEG): Caelyx® (Barenholz, 2012).

Despite SAXS being a usual method of choice for the accurate characterization of nanomaterials, the interpretation of the scattering curves, i.e. the model fitting, is frequently intricate for complex samples. Liposomal drugs or loaded polymeric nanoparticles belong to this class, as both the carrier and the incorporated biotarget contribute to the scattering intensity. These heterogenous samples require either *a priori* knowledge about their morphology or the measurement of complementary scattering curves obtained under different experimental conditions, like in solvent contrast variation in SAXS

In this chapter, the utilization of continuous contrast variation in SAXS is examined for the nano-drug Caelyx and for typical nanocarriers like lipid vesicles or polymeric colloids. In the latter case, the particle is coated with an antibody to resemble the biological conditions found upon injection in the bloodstream. Other components of the blood plasma like lipoproteins are also investigated with this technique. Parts of this chapter have been adapted from articles published previously (Minelli *et al.*, 2014; Garcia-Diez *et al.*, 2016*a*).

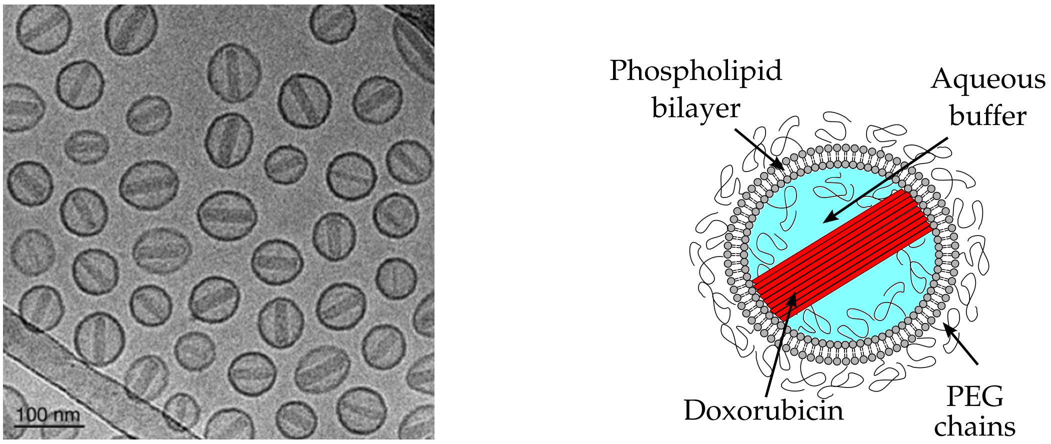

(a) Cryo-TEM **(b)** Scheme

Figure 6.1 | a) Cryo-TEM micrograph of Caelyx® (Barenholz, 2012) and b) schematic representation of the PEGylated liposomal doxorubicin morphology.

6.1 Materials

In this chapter, the continuous contrast variation method in SAXS presented in chapters 4 and 5 has been employed in a variety of samples related with nanomedicine. In this section, the different samples characterized with this technique are described and the more relevant aspects of the experiments are detailed.

The results obtained on the Caelyx nano-drug are described in detail in section 6.2 and 6.3.1, while the empty liposomes are investigated under osmotic pressure in section 6.3.2. The size measurements on the lipoproteins are presented in section 6.4 and the use of the protein-coated nanoparticles is detailed in section 6.5.

Caelyx: PEGylated liposomal doxorubicin

Caelyx® (SP Europe, Brussels, Belgium) was purchased from Hungaropharma Ltd and consists of liposomes suspended in 10 mM histidine buffered sucrose solution (pH 6.5) formed by fully hydrogenated soy phosphatydilcholine (HSPC), cholesterol, and DSPE-PEG 2000 (N-(carbonyl-methoxypolyethylene glycol 2000)-1,2-distearoyl-sn-glycero-3-phosphoethanolamine). The latter yields a steric barrier at the liposomal surface due to the PEG 2000 residues that extend the blood-circulation time, the so-called *stealth* function. Doxorubicin is encapsulated in the PEGylated liposome via an active loading procedure, which results in a crystal-like doxorubicin precipitate inside the liposomes, as observed in the micrograph 6.1a (Barenholz, 2012). A schematic depiction of the sample morphology is shown in figure 6.1b.

Lipid vesicles: PEGylated and plain liposomes

The PEGylated liposomes were prepared by the Institute of Materials and Environmental Chemistry (Hungarian Academy of Sciences, Budapest, Hungary) with the same lipid composition as the commercially available Caelyx for comparison purposes: the weight ratios of HSPC:DSPE-PEG 2000:cholesterol were 3:1:1 (corresponding to molar ratios of 0.565:0.053:0.382). The samples were extruded through polycarbonate filters (Nucleopore, Whatman Inc., Little Chalfont, UK) of five different pore sizes, from 50 to 400 nm. A more detailed description of the preparation is found elsewhere (Varga *et al.*, 2014*a*). The components of the plain liposomes are HSPC:cholesterol with a weight ratio of 3:1 (corresponding to molar ratios of 0.6:0.4). The preparation is identical to the PEGylated liposomes. All the liposome samples are suspended in a 10 mM phosphate buffered saline (PBS) pH 7.4 buffer solution.

Human lipoproteins

Native lipoproteins from human plasma were purchased from Merck Milipore (Darmstadt, Germany) and suspended in 150 mM NaCl, 0.01 % EDTA buffer with pH 7.4. The High Density Lipoprotein (HDL) has a protein concentration of 14.3 g L^{-1}, while the Low Density Lipoprotein (LDL) has a protein concentration of 5.96 g L^{-1}, considering that the weight ratio between lipids and proteins is approximately 4:1 in the LDL sample.

PS-COOH particles coated with IgG

The polystyrene nanoparticles with carboxylated surfaces (PS-COOH) described in chapter 4 are coated with the protein Immunoglobulin G (IgG). A set of four IgG-coated polystyrene nanoparticle samples was prepared by the Surface and Nanoanalysis group of NPL (Teddington, UK) by incubating 0.05 % (w/w) particles with varying concentrations of IgG from 0.5 to 4 g L^{-1} in 100 mM Tris buffer at pH 8 under continuous shaking for 2 h. Any unbound IgG was then removed from the particle samples by three cycles of centrifugation and redispersion in clean buffer.

In the continuous contrast variation experiment with sucrose as contrast agent, a protein concentration of 4 g L^{-1} IgG was physisorbed at the surface of the bare PS-COOH particles. The details of the density gradient capillary are discussed in section 6.5.1.

6.2 Traceable size determination of a liposomal drug

The first approved nano-drug, Caelyx, was rapidly followed by a few other products (Yeh *et al.*, 2011; Barenholz, 2012). Nowadays there are approximately 250 nanomedicine products that are either approved by the relevant health agencies or are under clinical trials (Etheridge *et al.*, 2013). On the other hand, there is a translational gap between the experimental work devoted to the development of new nano-drug candidates and the clinical realization of their use, which is also reflected in the high number of studies dealing with nanomedicine and the number of approved products on the market (Venditto & Szoka Jr., 2013). As highlighted in a recent review by Khorasani *et al.* (2014), one of the main reasons for this translational gap is that the current characterization techniques possess limitations and there is a need for standardization in this field.

Among many relevant physicochemical properties of nano-drugs, one of the most important to be accurately determined is the size of the nanocarriers, which directly

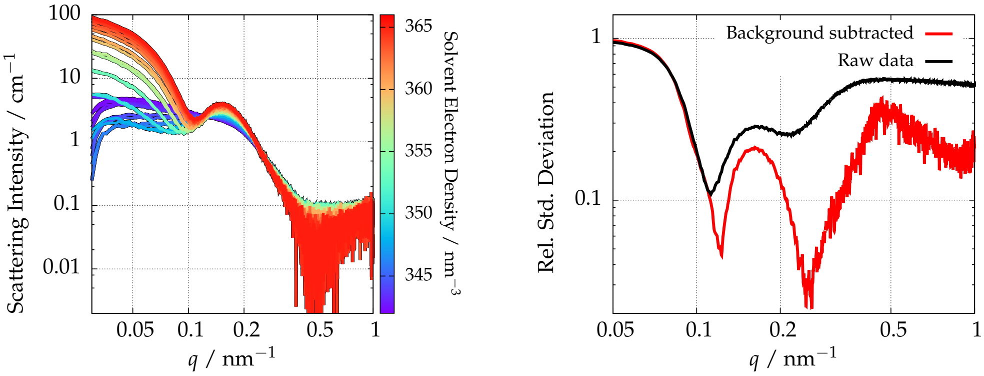

(a) Contrast variation with density gradient

(b) Isoscattering point positions

Figure 6.2 | a) Scattering curves at different suspending medium electron densities obtained with a solvent density gradient of Caelyx in aqueous iodixanol with constant buffer osmolality. Figure b) shows the precise position of the isoscattering points before and after the proper correction of the background.

relates to the *in vivo* biodistribution of the drug. The ultimate goal in this regard is to reach a traceable size determination of the nanomaterial and therefore the continuous contrast variation technique in SAXS is a suitable method to assess the size of a complex liposomal drug, such as the PEGylated liposomal formulation of doxorubicin.

Osmolality is a measure of the balance in an aqueous medium between water and the solvated chemical components. It quantifies the osmotic pressure being exerted by the solute in the studied membrane and is typically given in osmoles (Osm) of solute per kilogram of solvent. The need of an iso-osmolal suspending medium to mimic the physiological conditions of plasma and avoid osmotic effects in the vesicle membrane requires the use of Optiprep$^{\text{TM}}$ (Sigma-Aldrich, Missouri, USA) as contrast agent, an aqueous solution of iodixanol, which has an osmolality of 290 to 310 mOsm kg^{-1}. By employing Optiprep, the suspending medium osmolality can be kept constant along the density gradient capillary.

SAXS curves of the liposomal doxorubicin sample measured at different suspending medium electron densities are shown in figure 6.2a, where a maximum solvent electron density of 365.2 nm^{-3} was reached with an Optiprep mass fraction of 35 %. In the scattering curves, it is possible to observe the variation of the curve features through the increase of the suspending medium density, which indicates the complexity of the internal structure of the nanocarrier. Besides, the appearance of an isoscattering point around $q = 0.12$ nm^{-1} is a further indicator of the structural complexity of the drug-carrier.

The solvent background has been subtracted by measuring the scattering curves of a density gradient of Optiprep and buffer without nanocarriers. The low scattering power of the PEGylated liposomal doxorubicin at high q values and the contribution of the Optiprep background result in a decreased signal-to-noise ratio in the high-q range of the corrected scattering curves, although in the Fourier region below $q = 0.3$ nm^{-1} the background effect is much less dominant.

Table 6.1 | Diameter of Caelyx obtained by two different SAXS approaches, DLS and Cryo-TEM. The result from DLS was obtained by the Institute of Materials and Environmental Chemistry (Hungarian Academy of Sciences, Budapest, Hungary), whilst the Cryo-TEM diameter was extracted from Barenholz (2001).

	Diameter (nm)
Shape scattering function	65.5 ± 4.7
First isoscattering point	73 ± 9
DLS	86
Cryo-TEM	75

6.2.1 Isoscattering point approach

In the low q part of the scattering curve, an isoscattering point is clearly visible as highlighted in figure 6.2a. The isoscattering point position relates directly to the external radius of the measured particle inaccessible to the solvent, as explained in section 2.3.1. Therefore, the PEG-chains attached to the liposome surface might not be quantified in this approach due to the permeability of the polymer layer. The isoscattering point position is precisely determined by calculating the relative standard deviation of all the scattering curves at each q-value, as shown in figure 6.2b. As discussed in chapter 4, the proper subtraction of the solvent background is essential for the right interpretation of the data, specially for intense scatterers like Optiprep. A clear shift in the minima of the relative standard deviation curve is observed in figure 6.2b after correcting the background effects. Hence, the first isoscattering point $q_1^\star$ is located at $q_1^\star = (0.123 \pm 0.016)\ \mathrm{nm}^{-1}$, which corresponds to a diameter of (73 ± 9) nm. A second isoscattering point at $q_2^\star = (0.25 \pm 0.06)\ \mathrm{nm}^{-1}$ is still visible, although the large diffuseness of the isoscattering points at higher q values, related with the polydispersity of the ensemble and the possible ellipticity of the doxorubicin loaded liposomes, makes it less reliable for the determination of the outer diameter.

6.2.2 Shape scattering function calculation

In order to provide a complementary result to the diameter value obtained with the isoscattering point approach, an alternative evaluation procedure has been used, namely the calculation of the shape scattering function introduced in section 2.3.2 which extracts all contributions from the 30 measured scattering curves that change with the contrast at different solvent densities. The shape scattering function of the Caelyx sample contains essentially information only about the shape and size distribution of the space filled up by the liposomes, i.e. the contributions of the phospholipid bilayer and the encapsulated doxorubicin to the scattering intensity are cancelled. Thus, the complex interpretation of the original SAXS curve of Caelyx is avoided and enables the size determination of the liposomal carrier by fitting the analytical model for homogeneous spherical objects expressed by equation 2.24 . A model with a certain ellipticity was also attempted using the expression 2.25, due to the slight liposomal eccentricity observed in TEM images (Barenholz, 2012) though the best fit was accomplished with a spherical model.

The shape scattering function calculated from the SAXS curves and the theoretical model fitting are depicted in figure 6.3a. The diameter obtained from the spherical form factor fit is (65.5 ± 4.7) nm, smaller than the value calculated from the isoscattering point position and with a smaller associated uncertainty. Both values are in good agreement within their combined measurement uncertainties, considering that the uncertainty associated to the diffuseness of the isoscattering point arises principally from the polydispersity of

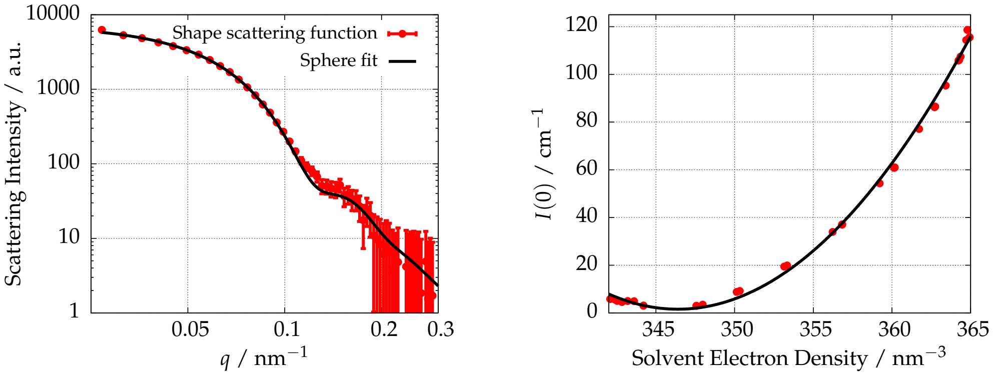

(a) Shape scattering function **(b)** Zero-angle intensity

Figure 6.3 | Evaluation of the scattering curves of Caelyx. a) The experimental shape scattering function of the liposomes is shown with symbols whilst the model fit for homogeneous spherical particles is depicted with a thick line. b) The measured intensity at zero-angle of Caelyx as a function of the electron density of the aqueous iodixanol suspending medium is shown with symbols and the function fitted to the experimental data is depicted in black: The average density is 346.4 nm^{-3} and there is an offset in $I(0)$ of 1.6 cm^{-1}.

the sample. This fact is supported by the broad size distribution determined by the shape scattering function fitting. When assuming a Gaussian size distribution, the polydispersity degree of the nanocarrier is ca. 40%. Therefore, the weighted average value of (67 ± 5) nm can be embraced as a reliable external diameter for the liposomal drug-carrier. The results of both approaches are summarized in table 6.1 together with the diameter of Caelyx obtained with other techniques.

The average diameter obtained by contrast variation in SAXS is smaller than the result obtained with DLS of ca. 86 nm, performed on a W130i apparatus (Avid Nano Ltd, High Wycombe, UK) by the Institute of Materials and Environmental Chemistry (Hungarian Academy of Sciences, Budapest, Hungary) similarly to the protocol described in Varga *et al.* (2014*a*). This deviation between both results can be attributed to the fact that the DLS measurand is the hydrodynamic size of the nanoparticles, while SAXS provides the size of the spherical volume inaccessible to the solvent. As the 2 kDa PEG-chains attached to the surface of the liposomes contribute to the hydrodynamic radius but that layer is permeable to the solvent and, therefore, invisible to contrast variation SAXS, the ca. 20 nm difference between the diameters determined by DLS and SAXS is justified.

6.2.3 Average electron density

At low q-values, the Guinier approximation can be used as explained in section 2.3.2. By fitting the spherical form factor to the q-range just below the first minimum of the scattering curves, an extrapolated value for the intensity at zero-angle $I(0)$ could be obtained as displayed in figure 6.3b. The minimum of the parabola fitted to the experimental points determines the average electron density of the drug carrier system, according to the equation 2.36.

From this calculation, a value of ρ_0 = (346.2 ± 1.2) nm^{-3} is obtained which corresponds to a combination of the electron density of the liposomal nanocarrier and the precipitated doxorubicin drug. The uncertainty of 1.2 nm^{-3} is associated with the vertical size of the focused X-ray beam. The obtained density is slightly higher than the value of 338 nm^{-3} estimated for empty PEGylated liposomes (Kučerka *et al.*, 2006) due to the presence of the

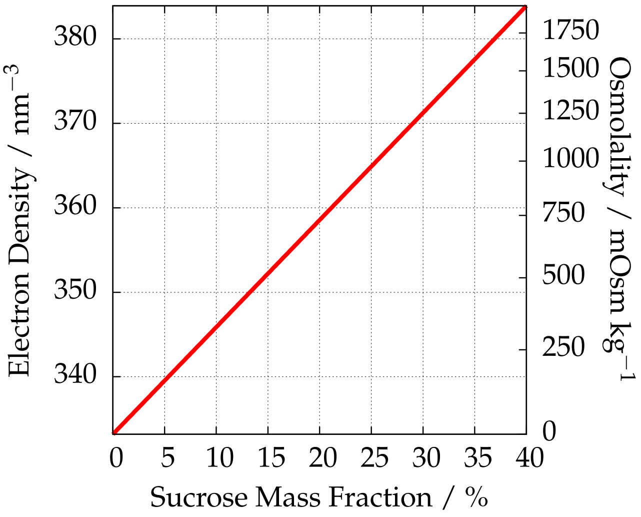

Figure 6.4 | Relationship between the solvent electron density and the solvent osmolality for an aqueous sucrose solution.

doxorubicin-sulfate aggregate in the intraliposomal volume.

6.3 Osmotic effects in liposomes

The rigidity of the nanocarriers is a relevant property directly related with its drug delivery efficacy, the particle stability or the release rate of the encapsulated drug. In fact, some of these characteristics might change upon injection into the blood vessels due to the mechanical stress applied to the nanocarriers in the process. In the case of lipid vesicles, i.e. liposomes, the permeability of water through the phospholipid bilayer is a defining aspect of their physicochemical behaviour. Although many aspects about the membrane permeability have been studied (Nagle *et al.*, 2008; Mathai *et al.*, 2008; Olbrich *et al.*, 2000), the evaluation of the liposomes rigidity and its osmotic activity is still challenging.

The osmotic behaviour of liposomes depends, basically, on their size and chemical composition. For example, the incorporation of cholesterol can vary the fluidity of the lipid bilayer. Larger liposomes tend to be osmotically active (de Gier, 1993) and behave according to the Laplace law: the osmotic pressure needed to deform them decreases for increasing sizes. In the case of liposomal nanocarriers, the intraliposomal osmolality should be equal to the buffer outside of the liposomes to enhance the particle stability.

Therefore, it is an important question whether the incorporation of a drug into the intraliposomal volume might modify its osmotic activity. For example, it is expected that the small size of Caelyx and the doxorubicin-sulfate aggregate in the intraliposomal volume increase the resistance against the buffer osmotic pressure in comparison to an empty liposomal particle. No osmotic pressure effects were observed in the size or density of the liposomal drug Caelyx in the previous section 6.2 due to the constant osmolality of the suspending medium along the whole density gradient that was achieved using Optiprep as contrast agent.

However, this effect can be studied by increasing systematically the osmolality of the suspending medium using aqueous sucrose in the buffer. As shown in figure 6.4, the sucrose molecule acts simultaneously as a contrast agent and as an instrument to increase the solvent osmolality. This enables the study of the osmotic effects in liposomes by the density gradient technique in SAXS using aqueous sucrose as suspending medium.

In this section, a thorough investigation of Caelyx under the effects of an increasing

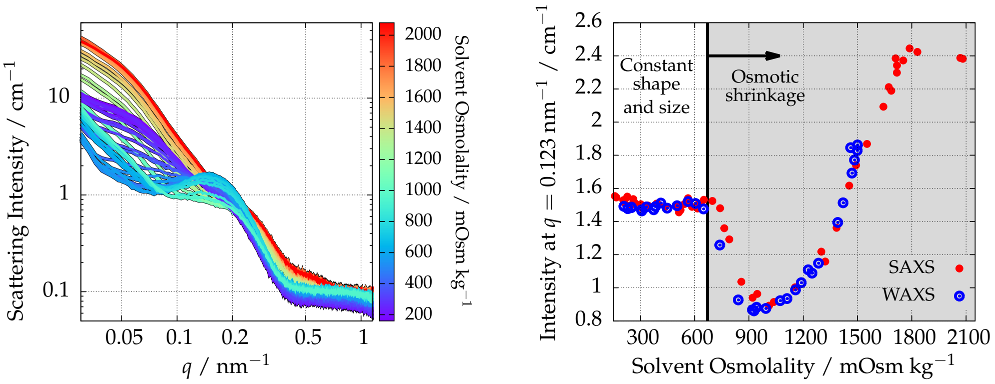

(a) Caelyx scattering curves

(b) Isoscattering point intensity

Figure 6.5 | Osmotic effects of Caelyx in an aqueous sucrose density gradient. a) Scattering curves measured at different solvent osmolalities b) Scattering intensity at $q_1^\star$ as a function on the aqueous sucrose solution osmolality. An osmotic threshold appears at 670 mOsm kg^{-1}. The experiment was measured with two different configurations with identical results.

solvent osmolality is performed, complementary to the study of the empty liposomal nanocarrier under similar conditions. Besides, the consequences of PEGylation on the liposomal structure are also studied using this technique, focusing principally in its osmotic activity.

6.3.1 Application to drug-stabilized liposomes

By means of the density gradient technique, scattering curves of the liposomal doxorubicin were recorded at different sucrose concentrations of the suspending medium, i.e. at different buffer osmolalities, as shown in figure 6.5a. A maximum osmolality preparation was achieved with a 37.8 % sucrose mass fraction, which corresponds to an electron density of 381.1 nm^{-3} and a solvent osmolality of 1776 mOsm kg^{-1}, whereas a lighter solution was produced without sucrose by adding pure water to get the same Caelyx concentration. Considering the sucrose mass fraction of the Caelyx buffer to be 10%, this latter preparation has an electron density of 339.4 nm^{-3} and an osmolality of 151 mOsm kg^{-1}. The X-ray scattering measurements were performed at two different detector-to-sample distances, in order to study a broader q-range, spanning from 0.03 to 5.55 nm^{-1}. Using the WAXS configuration described in section 3.4.2, the 1,0-diffraction peak of the doxorubicin fiber-like precipitate around $q = 2.3$ nm^{-1} (Li *et al.*, 1998) was observed, as depicted in the figure 6.6a after proper background correction. This Bragg diffraction arises from the crystalline nature of the doxorubicin aggregate in the intraliposomal volume.

As discussed in the previous section, by increasing the electron density of the suspending medium, the scattering curves of the drug carrier change drastically due to contrast variation. In the case of the aqueous sucrose gradient shown in figure 6.5a, this effect is also observed and strongly resembles the curves measured with the Optiprep density gradient depicted in figure 6.2a. Nevertheless, upon a certain sucrose concentration (corresponding to osmolalities around 900 mOsm kg^{-1} in figure 6.5a), the features of the scattering curves change abruptly, because the suspending medium osmolality is so high that it induces morphological changes in the liposomal structure and, consequently, the scattering form factor of the particles changes.

This effect can be quantified by examining the scattering intensity at the first isoscatter-

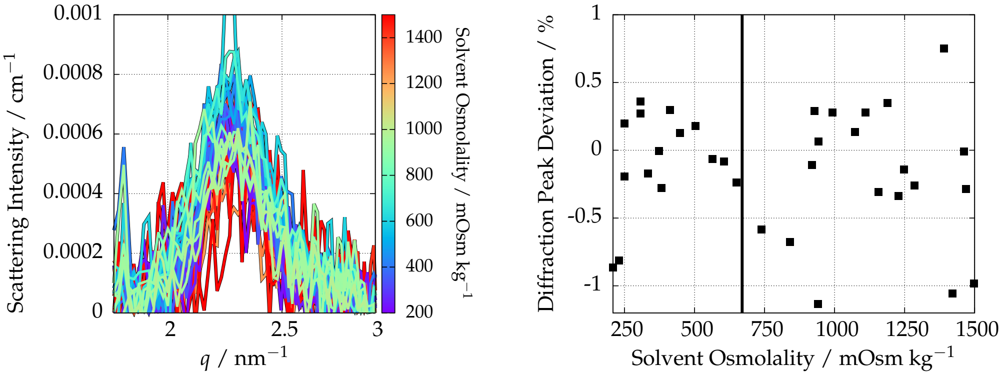

(a) DOX diffraction peak

(b) Peak position deviation

Figure 6.6 | Osmotic effects in the intraliposomal doxorubicin-precipitate by using sucrose as contrast agent: a) (1,0) diffraction peak of doxorubicin after background subtraction for increasing solvent osmolality. The mean FWHM of the peak is 0.333 nm^{-1}. b) Deviation of the doxorubicin aggregate diffraction peak position from the weighted average $q = 2.28$ nm^{-1}.

ing point position ($q_1^\star = 0.123$ nm^{-1}) as a function of the suspending medium osmolality, as shown in figure 6.5b. The intensity of the isoscattering points is independent of the electron density of the solvent as long as the size and the shape of the investigated particle remain constant. However, there is a clear osmolality threshold at 670 mOsm kg^{-1} in figure 6.5b when the intensity at $q_1^\star$ decays drastically. Above this threshold, the osmotic pressure at the liposomal bilayer is so high that the liposome starts shrinking and changes its size, structure and, consequently, scattering form factor. The increased resistance against osmotic pressure, more than double the blood plasma osmolality and much higher than the osmolality needed to shrink empty PEGylated liposomes (Varga *et al.*, 2014*a*), is explained by the encapsulation of crystal-like doxorubicin inside the liposome.

The large osmotic pressure produces a reversible shrinkage of the liposome though it is not capable of cracking it. This was proved in an additional experiment by increasing the osmolality of the buffer to 1334 mOsm kg^{-1} with a sucrose mass fraction of 31.4% and then reducing it to 565 mOsm kg^{-1} by adding distilled water, where it was observed in the scattering curves that the osmotic shrinkage process is reversible.

The behaviour of the nano-drug for an increasing solvent osmolality can be further studied by evaluating the crystal structure of the doxorubicin aggregate, represented by the diffraction peak displayed in the figure 6.6a. For this purpose, a WAXS configuration was employed which extends the available q-range until 5.55 nm^{-1} by reducing the sample-to-detector distance to $L = (569 \pm 1)$ mm. The position of the peak in the reciprocal space depending on the suspending medium osmolality is depicted in figure 6.6b and shows that its position deviates less than 1 % from the weighted average $q = 2.28$ nm^{-1} along the whole osmolality range. This proves that the fiber-like structure of the drug inside the liposome is also constant during the osmotic shrinkage of the liposomes. The measured position of the (1,0) diffraction peak matches exactly the value measured from doxorubicin-sulfate complexes in solution (Lasic *et al.*, 1992).

To conclude this section, the diameter obtained from the isoscattering position in the Optiprep solution can be compared with what is measured in an aqueous sucrose suspending medium. In the latter, if only the scattering curves below this osmolality threshold are considered, the relative standard deviation for each q value reveals a pronounced minimum for the first isoscattering point as depicted in figure 6.7. When comparing this

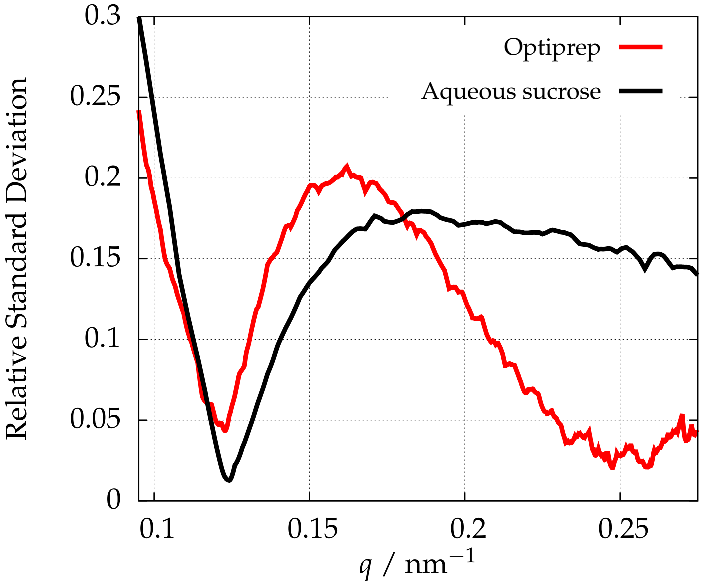

Figure 6.7 | Isoscattering point position quantified by the calculation of the relative standard deviation of the scattering curves for different solvent density gradients. In the case of the aqueous sucrose solution (black line), only the scattering curves below the osmolality threshold were employed for the calculation.

result with the relative standard deviation curve obtained from the Optiprep contrast variation measurements, both values for the size of the drug carrier agree remarkably well within 2 %. This reflects the independence of the technique from the contrast agent added to the suspending medium and shows the repeatability of the results.

6.3.2 Does PEGylation affect the osmotic activity of liposomes?

Typically, unilamellar liposomes present a very narrow size distribution and spherical shape, whose diameter ranges from 50 nm to some hundreds of nanometres. The covalent attachment of biocompatible polymers can improve the liposome stability. For example, PEG polymer chains show very low toxicity (Yamaoka *et al.*, 1994) and are widely used as stabilizer (Sou *et al.*, 2000). PEGylated liposomal formulations, also called sterically stabilized liposomes (SSL) or *stealth* liposomes, show longer blood circulation times *in vivo* (Barenholz, 2001) and exhibit a slow drug release rate. PEG-modified liposomes have become of importance lately due to their increased drug pharmakinetics, decreased plasma clearance and improved patient convenience (Gabizon & Martin, 1997; Harris & Chess, 2003). Therefore, the self-assembly of lipid structures in the presence of PEG moieties has been studied for different lipids (Lee & Pastor, 2011).

The incorporation of biocompatible polymers increases the phospholipid bilayer strength and enhances the vesicle rigidity, which relates to the increase of the bending modulus (Liang *et al.*, 2005; Sou *et al.*, 2000). The higher membrane stiffness of SSLs has been extensively characterized with methods such as AFM (Spyratou *et al.*, 2009) though other techniques such as light scattering have found a higher osmotic activity in SSLs in comparison to their non-PEGylated counterparts when incubated in serum (Wolfram *et al.*, 2014). Further investigations about the relationship between PEGylation and the liposomal osmotic behaviour in suspension are essential. In the following work, the different response of SSLs and plain liposomes to osmotic pressure is studied by SAXS.

For this purpose, five PEGylated and three plain liposomes were extruded with different pore sizes, as explained in section 6.1. To simplify the following discussion, the liposomes are named after the hydrodynamic diameter measured by DLS. It is apparent from these measurements that the size of the pore and the polydispersity degree of the liposome

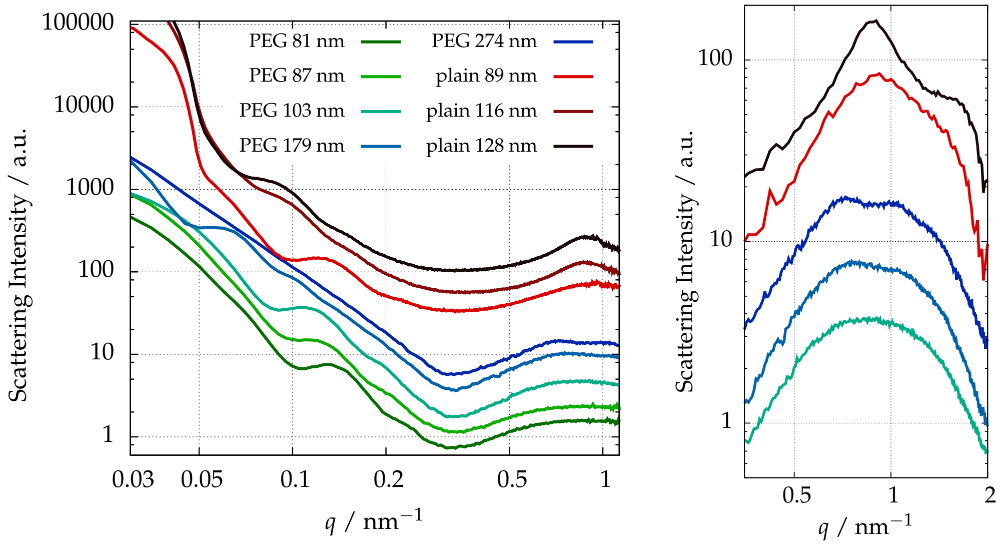

(a) Scattering curves of the liposomes in buffer

(b) Bilayer scattering feature

Figure 6.8 | a) Scattering curves of the different liposomes in buffer. The curves are intensity shifted for clarity. The five SSLs are presented in the lower part of the plot. The diameters in the legend are extracted from DLS measurements. b) The phospholipid bilayer scattering feature of the liposomes in buffer: High q-region of the scattering curves of two plain liposomes and the three largest SSLs in buffer. The color code of the scattering curves is shared with figure a).

sample are directly related.

The SAXS measurements of the eight liposomes are shown in figure 6.8a, where the first minimum q-value ranges from $\sim$0.1 nm^{-1} in the 81 nm SSL to $\sim$0.05 nm^{-1} for larger sizes. For high polydispersities this scattering minimum gets smeared out, as it can be observed for the 274 nm SSL. It can be stated from these measurements and the DLS results that the polydispersity degree rises for increasing liposomal sizes. Besides, non-PEGylated liposomes show slightly broader size distributions than SSLs.

Focusing on the high q-region of the single-contrast SAXS curves as displayed in figure 6.8b, the scattering feature related to the phospholipid bilayer structure is observed. For Unilamellar Vesicles (ULV), the feature shape is typically round with a maximum around $q = 0.86$ nm^{-1} (Varga *et al.*, 2012), related to a distance ($d = {}^{2\pi}/_{q}$) of 7.3 nm, as it can be seen in the case of small PEGylated liposomes. For SSLs extruded with larger pores, the bilayer shape shows incipient Bragg peaks which suggest the simultaneous presence of Multilamellar Vesicles (MLV) with a lamellar repeat distance of 7.3 nm and unilamellar SSLs. These *quasi Bragg peaks* arise from the periodic structure of the phospholipid bilayer and the water layers, which interact through a combination of the electrostatic potential, the Van der Wals attraction and other hydration terms. Nevertheless, the MLV population cannot exceed the total number of unilamellar liposomes because the scattering contribution from ULV is still clearly dominant (Sakuragi *et al.*, 2011). The schematic representation of the different types of liposomes and the graphical definition of the lamellar repeat distance are depicted in figure 6.9.

The bilayer feature of the plain liposomes differs completely from the round shape visible in unilamellar vesicles. The diffraction peaks appearing at $q_1 = 0.88$ and $q_2 = 1.9 \simeq 2q_1$ nm^{-1} correspond to a slightly smaller lamellar repeat distance of 7.1 nm and are related to a more pronounced presence of MLVs, possibly of Oligolamellar Vesicles

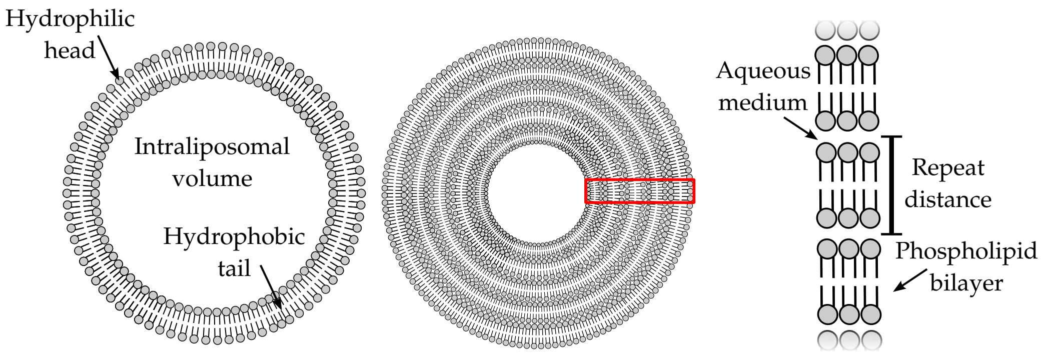

(a) ULV **(b)** MLV **(c)** Bilayer in a stack

Figure 6.9 | Schematic representation of the different types of liposomes: a) Unilamellar vesicle (ULV) and the different components of a phospholipid bilayer. b) Multilamellar vesicle (MLV) composed of concentric lipid bilayers. While an oligolamellar vesicle (OLV) is a MLV with only a few lamellae, a bilamellar liposome consists of only two concentric phospolipid bilayers. A stack of phospholipid bilayers is highlighted with a red box and depicted in more detail in c) with the graphical definition of the lamellar repeat distance.

(OLV) with only a few lamellae. This tendency is emphasized for larger plain vesicles, as observed for the 128 nm plain liposome, where the round shape of the scattering feature practically disappears. This observation suggests that the plain liposomes distribution consists of bi-, oligo- and multilamellar liposomes in a much higher ratio than the SSLs.

The effect of PEGylation induces a higher ratio of ULVs due to the increased negative charge of the phospholipid bilayer in comparison to plain liposomes, which hinders the creation of periodic lamellar structures. Nevertheless, small populations of OLVs and MLVs coexisting with unilamellar liposomes can be observed for large extrusion pore sizes in SSLs as well. In conclusion, the size and composition of the liposomes affect remarkably the formation of unilamellar vesicles and the shape of the phospholipid bilayer.

The behaviour of the different liposomal structures to osmotic stress can be examined with a continuous contrast variation experiment using sucrose as contrast agent, similarly to the measurements with the Caelyx sample in section 6.3.1. The scattering curves measured for a PEGylated liposome with diameter 81 nm are displayed in figure 6.10a, where the solvent osmolality has been increased until 1409 mOsm kg^{-1} using a maximum sucrose mass fraction of 27.3 %. From the low q-region of these scattering curves some facts can be extracted which reveal preliminary the structural changes of the liposome induced by the osmotic pressure.

The curves do not intersect clearly in one point, even for low sucrose concentrations as occured in the Caelyx case. The absence of an evident isoscattering point can be related with the shape variation of the liposome already at small osmotic pressures. However, a diffuse intersection point, or pseudo isoscattering point (Kawaguchi, 2004), is visible at $q = 0.18\,\mathrm{nm}^{-1}$. A very similar behaviour can be observed for the plain 89 nm liposome in figure 6.10b, where the suspending medium osmolality is increased until 1885 mOsm kg^{-1} by a 35 % sucrose mass fraction. In analogy to figure 6.5b, the intensity at the pseudo $q^\star$ as a function of the solvent osmolality is depicted in figure 6.11, as the deviation from the original intensity for a plain and a PEGylated liposome of similar diameters.

The intensity at $q^\star$ starts diverging from the original value already at very low solvent osmolalitites and reflects the continuous change in shape or size of the liposome when increasing the osmotic pressure. This behaviour occurs for both SSLs and plain liposomes and suggest that a sharp osmotic threshold, like in the Caelyx case, does not exist. Thus,

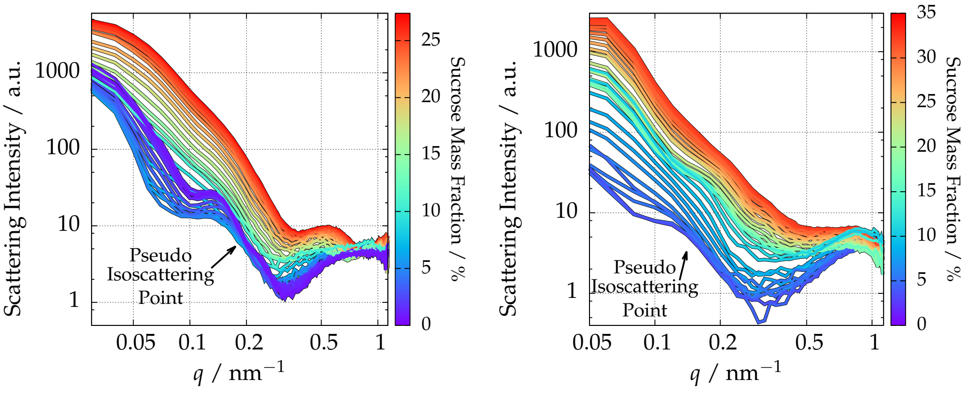

(a) SSL 81 nm **(b)** Plain 89 nm

Figure 6.10 | Scattering curves of the 81 nm SSL and the 89 nm plain liposomes measured at different solvent osmolalities with an aqueous sucrose density gradient. The positions of the pseudo isoscattering points at $q = 0.18$ nm^{-1} and $q = 0.16$ nm^{-1} are marked for the PEGylated and plain liposomes respectively.

the response of liposomes to osmotic pressure is steady and is already apparent at low osmolalities.

Besides, an evident variation of the scattering curves below $q \leq 0.3$ nm^{-1} is observed in figure 6.10a when increasing the solvent osmolality. For example, the minimum originally appearing at 0.1 nm^{-1} shifts slightly to larger q-values and disappears almost completely for high sucrose concentrations. This variation of the form factor can be caused by the flattening of the liposomal shape observed with Freeze-fracture TEM (Varga *et al.*, 2014*a*). Due to the increased osmotic activity, the original spherical liposome shrinks into an oblate spheroid. This hypothesis can be further explored by focusing on the scattering feature related to the phospholipid bilayer at the high q-region.

For this purpose, the bilayer feature of the 179 nm PEGylated liposome is shown in figure 6.12a for increasing solvent osmolalities. As observed in figure 6.10a for sucrose concentrations above 15 %, the bilayer scattering feature shifts abruptly to smaller q-values. This large contrast effect occurs at solvent densities close to the average electron density of the phospholipid bilayer (ca. 348 nm^{-3}), which corresponds to a sucrose mass fraction of $\sim$ 12 %. The convolution of the contrast-related effects with the variations induced by the osmotic pressure demands a more challenging evaluation, can prevent the right interpretation of the data and is, thus, unwanted. Therefore, the scattering curves shown here were measured with sucrose concentrations $\leq$ 10 %.

The original double-peak structure of the SSL at 0 % sucrose concentration observed in figure 6.12a transforms upon increasing the solvent osmolality and splits into three peaks of decreasing intensity at $q_1 = 0.48$ nm^{-1}, $q_2 = 0.86$ nm^{-1} and $q_3 = 1.28$ nm^{-1}. These Bragg peaks superimposed on the bilayer form factor reveal a periodic structure which can be related with a partial oligolamellar structure in the liposome system (Fernandez *et al.*, 2008). The three mentioned diffraction peaks translate into a lamellar repeat distance of ca. 13 nm, approximately doubling the thickness of the single phospholipid bilayer (Kenworthy *et al.*, 1995) and suggesting the appearance of a bilamellar structure (Demé *et al.*, 2002).

The transition between a single bilayer phase and a bilamellar phase at 10 % sucrose concentration supports the hypothesis presented above that the liposome shrinks into lens-shaped vesicles due to the osmotic pressure. The bilamellar structure might arise

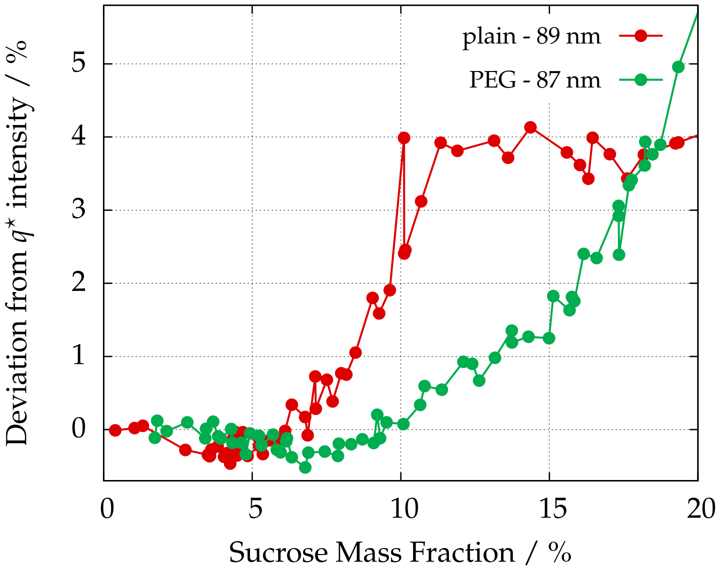

Figure 6.11 | Isoscattering point intensity of the liposomes: Deviation from the initial intensity at $q^\star$ at different solvent osmolalities measured for a PEGylated and plain liposome of similar diameters. A clear osmotic threshold can not be observed.

from the close bilayer contacts at the outest part of the elliptical liposomes, while the single bilayer conformation still remains dominant in the midsection of the liposomes. A similar morphology has been observed after the osmotic shrinkage of DPPC/DSPE-PEG$_{2000}$ vesicles (Terreno *et al.*, 2009). In fact, this behaviour was identical for all five studied PEGylated liposomes, independent of their size.

Besides, the changes of the phospholipid bilayer form factor are smooth upon increasing the osmotic pressure as shown in figure 6.12a, where the bilayer scattering feature starts varying at very low sucrose concentrations. This validates the observation from figure 6.11 and confirms that the increasing solvent osmolality affects continuously the structure of the liposomes and not as abruptly as in the case of Caelyx.

Contrarily, the phospholipid bilayer of the plain liposomes remains unchanged upon increasing the solvent osmolality until 1285 mOsm kg^{-1}, as displayed in figure 6.12b. This suggests that the MLV structure of the non-PEGylated vesicles increase their resilience and the multiple phospholipid bilayers strengthen the elastic modulus of the liposome membrane.

The fact that the incorporation of PEG moieties influences already the preparation and formation of the liposomes prevents a proper comparison of the osmotic effects between SSLs and plain liposomes of similar diameters. The existence of MLVs for non-PEGylated liposomes acts as a limiting factor for the osmotic activity and contrasts with the osmotic effects observed in unilamellar SSLs already at low sucrose concentrations, which shrinks the PEGylated liposomes into oblated ellipsoids.

The chemical effect of sucrose on the SSL membrane is a subject of discussion, because it can be argued that the disaccharide molecule penetrates the lipid membrane or creates a solvation shell around the liposomes. However, previous studies in this subject (Kiselev *et al.*, 2001*a*,*b*, 2003), the large size of the sucrose molecule and similar results with other experiments performed with salt (Varga *et al.*, 2014*a*) suggest otherwise. Therefore, it can be concluded that the study of the osmotic activity of liposomes can be performed successfully using aqueous sucrose and shows very distinguishable effects for ULVs (PEGylated liposomes) and MLVs (plain liposomes).

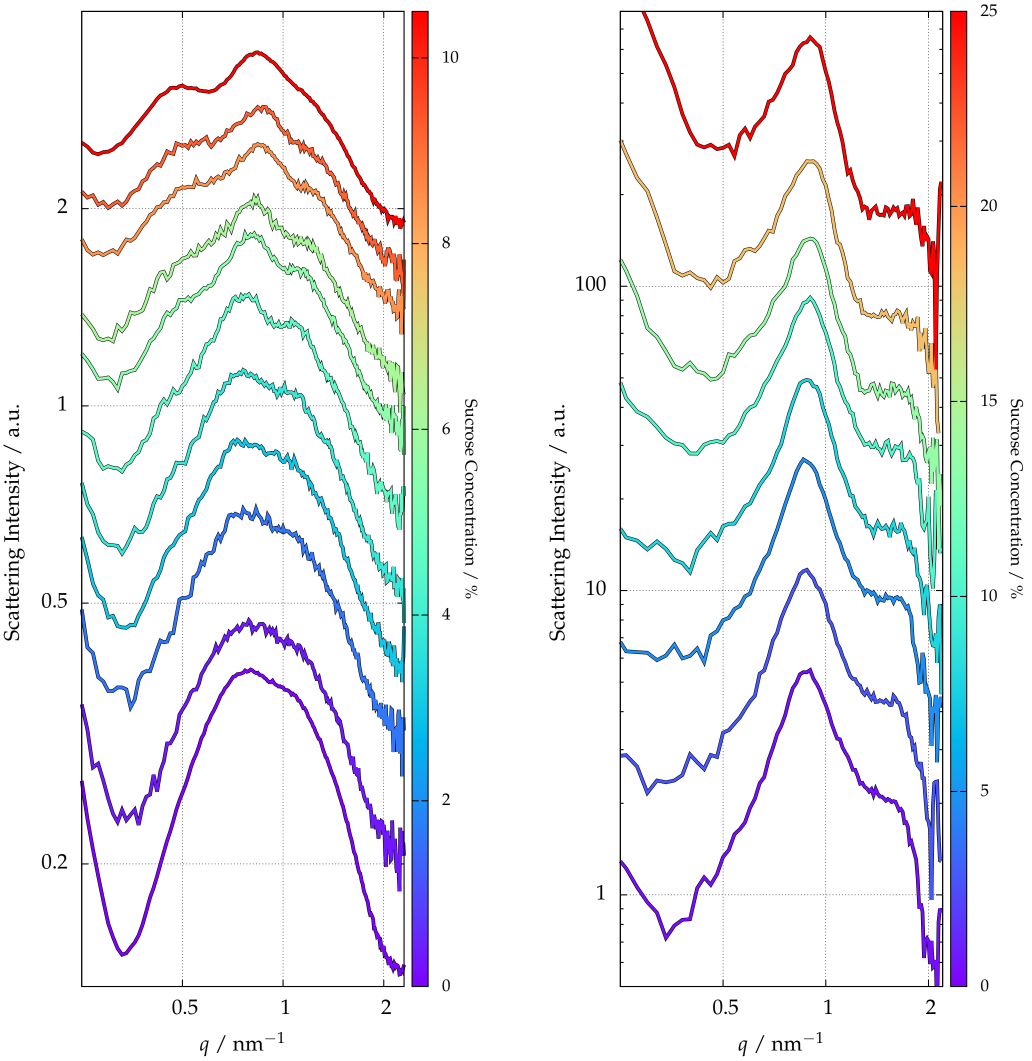

(a) PEG 179 nm

(b) Plain 128 nm

Figure 6.12 | Osmotic effects in the phospholipid bilayer of the liposomes: Scattering curves measured at different solvent osmolalities for a 179 nm SSL and a 128 nm plain liposome. The appearance of Bragg peaks in the SSL membrane contrasts with the unaltered shape of the bilayer in the plain liposome.

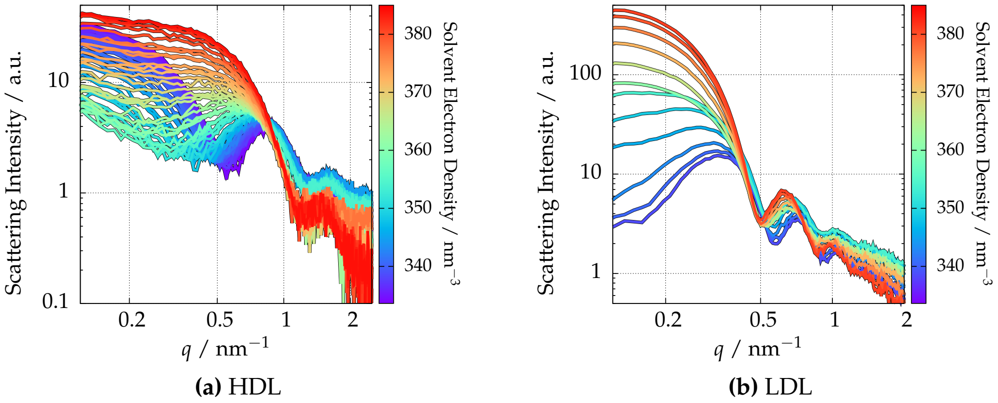

(a) HDL **(b)** LDL

Figure 6.13 | Scattering curves of HDL and LDL measured at different solvent densities by using an aqueous sucrose density gradient.

6.4 Sizing of blood plasma componenents

From a nanoscience point of view, human blood can be seen as a suspension of particles with different physiological roles, where important components are in the nanorange. Serum lipoproteins are the colloidal particles involved in the transport and metabolism of insoluble lipids and are among the most studied biological particles. The interest in their activity is understandable due to their direct relationship with very extended diseases in the Western world population, such as obesity or atherogenesis, e.g. obturation of the arterial walls. For example, the dysregulation of cholesterol in plasma, primarily carried within lipoproteins, is responsible of atherosclerosis (Munro & Cotran, 1988). Besides, they are a convenient model for lipid-protein interactions (Assmann & Brewer, 1974) due to their lipid core and the hydrated proteins isometrically situated on its surface.

Lipoproteins are isolated from blood plasma by ultracentrifugation (Havel *et al.*, 1955) and are normally classified by their density range, showing different chemical composition, size and pathological condition for each class (German *et al.*, 2006). Indeed, the size of lipoproteins is critically connected with disease risk (Gardner *et al.*, 1996) and Low Density Lipoproteins (LDL) are suggested to be more or less atherogenic depending on their size (Dreon *et al.*, 1994). The effect of diabetes on the lipoprotein size is also of great interest, especially the sex-dependency of the High Density Lipoprotein (HDL) size (Colhoun *et al.*, 2002).

Therefore, precise sizing techniques are a crucial tool to understand the physiological processes of lipoproteins (German *et al.*, 2006). The naturally narrow size distributions of LDL and HDL suggest small-angle scattering as a well-suited method and their heterogeneous morphology advises the use of a contrast variation approach. For instance, the first characterization attempts date back to the late 1970s with neutron scattering (Stuhrmann *et al.*, 1975), using salt (Tardieu *et al.*, 1976) and sucrose (Müller *et al.*, 1978) as SAXS contrast agents or modifying the sample temperature (Laggner *et al.*, 1977; Luzzati *et al.*, 1979).

The complicated inner structure of the lipoproteins revealed in more recent studies (Baumstark *et al.*, 1990; Schnitzer & Lichtenberg, 1994) encourages the use of parameter-independent and model-free analysis of the scattering data. With this objective, LDL and HDL samples were measured with continuous contrast variation in SAXS using 40

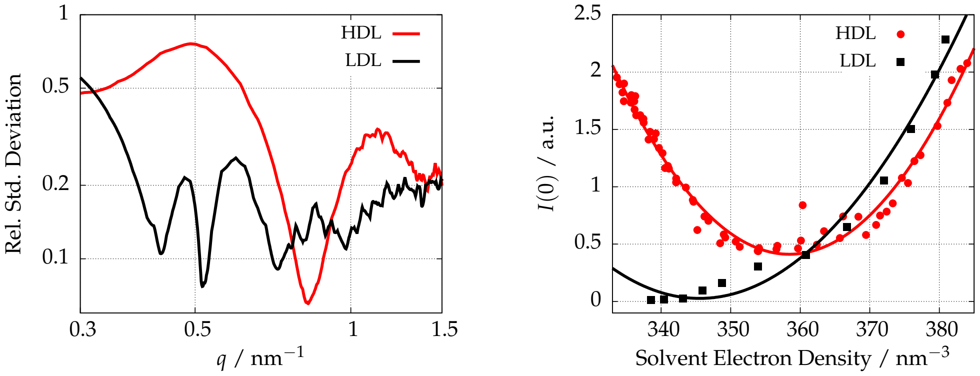

(a) Isoscattering point position **(b)** Average electron density

Figure 6.14 | Comparison of the model free approaches for HDL (red) and LDL (black)

% sucrose mass fraction to increase the solvent electron density until 384 nm^{-3}. The scattering curves obtained for HDL and LDL are presented in figures 6.13a and 6.13b respectively.

In the case of HDL in buffer, the first minimum appears at $q \approx 0.5$ nm^{-1}. By increasing the solvent density, this minimum shifts to smaller q-values hinting the denser composition of the protein shell in comparison to the lighter lipid and cholesterol core. A lighter core morphology is also expected for LDL (Luzzati *et al.*, 1979) and it agrees with the contrast effect observed in the scattering curves displayed in figure 6.13b.

The large number of observable minima indicates the narrow size distributions of both samples, providing ideal conditions to use the isoscattering point $q^\star$ approach. The relative standard deviation as a function of q calculated for both lipoproteins is shown in figure 6.14a, where the minima correspond to the position of $q_i^\star$. The clear minimum for HDL is located at $q^\star = (0.83 \pm 0.14)$ nm^{-1}, corresponding to an impenetrable diameter for the solvent of (11 ± 2) nm. The position of the first $q^\star$ in LDL is shifted to smaller q, $q^\star = (0.42 \pm 0.08)$ nm^{-1}, which translates into a solvent-excluded diameter of (21 ± 4) nm.

Considering that the lipoproteins are quasi-spherical (Stuhrmann *et al.*, 1975), these results can be compared to those extracted from literature. The different cholesterol tranport necessities reflect into a large variety of HDL subclasses with a diameter range between 7 and 13 nm (German *et al.*, 2006). For example, a diameter of 13 nm was observed for the subclass type HDL3 (Tardieu *et al.*, 1976), which deviates only 15 % from the result measured in our study. Difficulties to know the measured subclass of the commercially purchased HDL hinders a more thorough comparison.

In the case of LDL, several studies provide diameters between 21 and 28 nm (Tardieu *et al.*, 1976; Colhoun *et al.*, 2002; German *et al.*, 2006), though the most repeated values lay around 22 to 23 nm (Müller *et al.*, 1978; Luzzati *et al.*, 1979), less than 10 % deviation from our result. Nevertheless, the possible solvent penetration into the outer layers of LDL (Stuhrmann *et al.*, 1975; Tardieu *et al.*, 1976) calls for caution as the diameter obtained from the $q^\star$ position considers an impenetrable particle.

The effects of permeability and protein hydration might be related to the density of the lipoprotein, which is the most characteristic feature of each lipoprotein class. As described previously, the intensity at zero-angle is related to the average electron density by the expression 2.36 and can be measured. The experimental $I(q = 0)$ values are depicted in

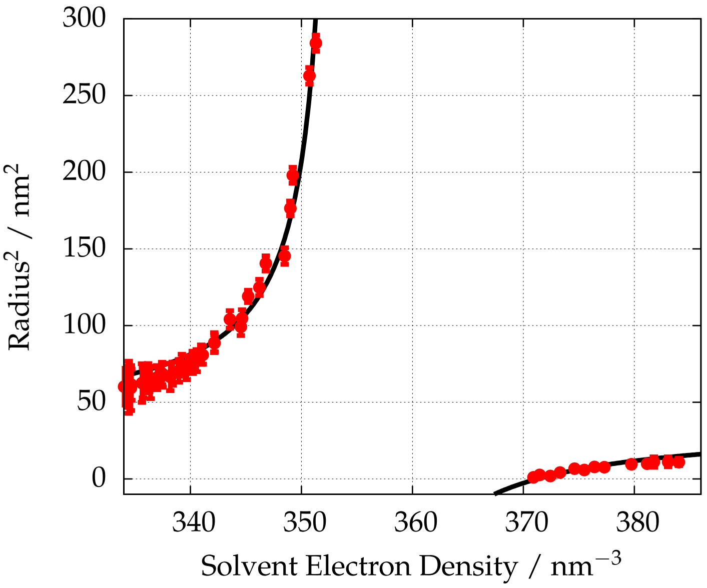

Figure 6.15 | Squared radius of the HDL scattering data. The analytical fit results in an average density of (353.6 ± 1.5) nm^{-3} and an external diameter of (12 ± 2) nm.

figure 6.14b, where the fits of the previous equation are shown as solid lines.

According to the analytical fit, the average density of HDL is (358.4 ± 1.5) nm^{-3} and the density measured in the LDL case is (345 ± 2) nm^{-3}. In the latter, the low number of points measured below the average density of LDL due to the limited range given by the water electron density (333 nm^{-3}) increases the uncertainty of the result, although the value is still in pretty good agreement with other SAXS studies (Tardieu *et al.*, 1976; Luzzati *et al.*, 1979). The protein-rich ($\sim$ 50 %) structure of HDL explains its higher density in comparison to LDL, composed mainly of lipids ($\sim$ 80 %).

Another model-free interpretation of the HDL scattering data is presented in figure 6.15, where the the squared radius of the Guinier region is presented as a function of the solvent electron density. As previously shown, the analytical expression 2.34 can be fitted to the experimental data, resulting in an average electron density $\rho_0 = (353.6 \pm 1.5)$ nm^{-3} and a particle shape radius of $R_c = (6 \pm 1)$ nm. The diameter obtained with this approach, (12 ± 2) nm, is consistent with the previous result. Probably due to the absence of relevant experimental points around the match point, the average density differs by almost 5 nm^{-3} from the $I(0)$ result.

The continuous contrast variation technique and the subsequent model-free analysis are easy and effective tools to measure the size and density of lipoproteins, very important attributes to understand the biological processes related to cholesterol and lipid transport. A more detailed analysis and modelling of the scattering data could have addressed some issues such as the hydration and distribution of the proteins on the surface, the permeability of the steric and lipid core or the radial distribution of cholesterol and triglycerides in the lipoprotein.

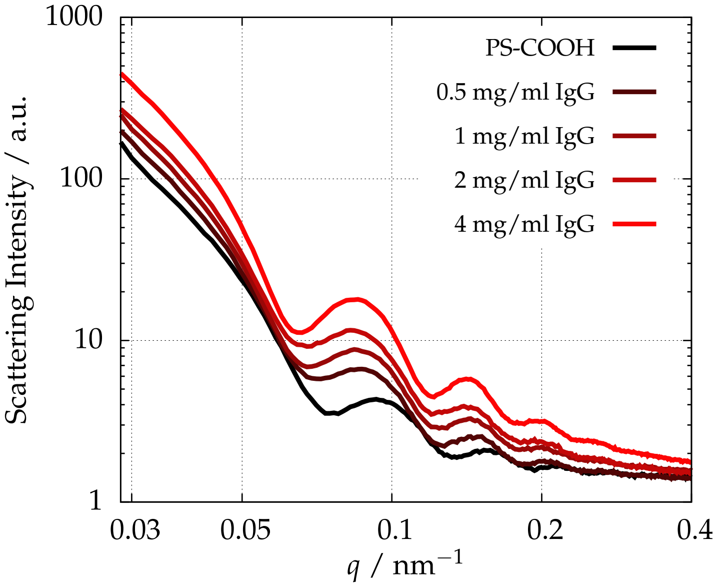

Figure 6.16 | SAXS curves at a single contrast of the PS-COOH particles coated with IgG at different concentrations.

6.5 Protein-coated low-density nanoparticles

The most recent efforts in nanomedicine aim for a high control of the characteristics of the nanocarrier surface, as the surface's properties are a defining element of its efficiency as drug carrier. Besides, nanoparticles interact with proteins when introduced into biological media, leading to the formation of the so-called *protein corona* surrounding the nanocarrier (Cedervall *et al.*, 2007; Monopoli *et al.*, 2011; Casals *et al.*, 2010). The identity of the biomolecule coating depends on the particle size, surface functionalization and charge (Lundqvist *et al.*, 2008; Tenzer *et al.*, 2013; Gessner *et al.*, 2003) and its detailed description is challenging. Yet, the ability to quantitatively characterise this interface is important in understanding particle behaviour in these complex environments and improving their surface engineering for enhanced functionality.

IgG is the most common type of antibody found in human serum and, therefore, a logical candidate to coat the studied nanoparticles with. In this case, we used commercially available PS-COOH particles, because polystyrene NPs are commonly used in the development of nanoparticle-based strategies for medicine, thanks to the low cost of their material and the versatility of their surface functionalization. The carboxylated surface prevents the agglomeration of the particles and also provides a chemical anchor for the protein binding. The use of SAXS to obtain a quantitative description of the protein corona is examined for different IgG concentrations, e.g. shell thicknesses, and compared with DLS and DCS (Minelli *et al.*, 2014).

The bare PS-COOH particles are highly charged, translating into a high ζ-potential, i.e. strong repulsive electrostatic potential on the particle surface. A ζ-potential of (-49 ± 1) mV was measured, which is drastically reduced to around -10 mV following the binding of the positively charged IgG. The SAXS measurements of the IgG-coated particles with different protein concentrations are shown in figure 6.16, where a clear shift to smaller q-values is observed for increasing concentration of IgG. This effect is clearly related with the increase in size for higher IgG concentration, although a quantitative description is complicated.

Due to the core-shell morphology of the polymeric bare particle observed in chapter

Table 6.2 | Concentration of IgG incubated with PS-COOH particles and IgG shell thickness as measured by single-contrast SAXS, DCS and DLS (Minelli *et al.*, 2014). A double-shell model with sharp interfaces was used for the SAXS results. The uncertainties are the standard deviations of repeated measurements.

ρ_{IgG} / mg mL^{-1}	ζ-potential / mV	T$_{DLS}$ / nm	T$_{DCS}$ / nm	T$_{SAXS}$ / nm
0.5	-10.8 ± 0.9	10 ± 1	3.7 ± 0.6	7.7 ± 1.4
1	-10.7 ± 0.6	11 ± 2	5.9 ± 0.5	8.4 ± 1.4
2	-9.6 ± 0.5	12 ± 2	7.6 ± 0.4	9.6 ± 1.5
4	-9.7 ± 0.5	15 ± 2	8.3 ± 0.4	9.6 ± 1.5

4, SAXS curves were analysed using a double-shell model based in the form factor 2.26, considering a sharp interface between the different components and a constant thickness and density of the IgG corona. In order to focus on the total diameter instead of the details of the internal structure, the limits of the inner and outer radii of the polymer shell are not fixed and are treated as fitting parameters together with the outer radius and the contrast difference of each shell with the polystyrene core.

The IgG shell thickness obtained for IgG-coated particles with different protein concentrations is shown in table 6.2 and compared to the size measurements performed with other techniques by the Surface and Nanoanalysis group of NPL (Teddington, UK). All techniques (DLS, DCS and SAXS) show an increase in the IgG-shell thickness with increasing concentration of the protein in solution during incubation. As expected, DLS provides higher values than the other techniques, as the measured thickness is related to the hydrodynamic properties of the system.

Although all techniques show an increase of the IgG shell thickness with increasing concentration of the protein, full consistency among them requires the calculation of a combined measurement uncertainty and further refinements of the SAXS and DCS modelling. For instance, the SAXS evaluation has neglected the possible spatial heterogeneity and hydration of the IgG corona and the model employed for the core particle overestimates the diameter by almost 10 % (chapter 4 and Minelli *et al.* (2014)).

6.5.1 Hard protein corona characterization with contrast variation

The possible inaccuracies arising from the previous modelling approach might be prevented by using continuous contrast variation and a model-free evaluation. For this purpose, the protein-coated particle with 4 mg mL^{-1} IgG was introduced in a density gradient with sucrose as contrast agent, resulting in an increase of the solvent electron density until 350.8 nm^{-3} at the maximum sucrose concentration of 14.7 %. The isoscattering point position is quantified by calculating the relative standard deviation of the 20 measured curves at each q, as depicted in figure 6.17. This value becomes minimal at $q = (0.080 \pm 0.011)$ nm^{-1}.

By comparing in figure 6.17 the relative standard deviation curves of the bare PS-COOH particle obtained in chapter 4 and the IgG-coated sample, it is noticeable that the position of the minimum is shifted to smaller q-values after the adsorption of proteins to the surface as a consequence of the increase in size. The diameter increase t is quantified by inserting in equation 2.30 the isoscattering positions before and after the target attachment, $q^\star = (0.090 \pm 0.006)$ nm^{-1} and $q^\star_{IgG} = (0.080 \pm 0.011)$ nm^{-1} respectively. Combining both results, t is expressed by:

$$t = R_{\mathrm{IgG}} - R = \frac{\kappa}{q^\star_{\mathrm{IgG}}} - \frac{\kappa}{q^\star}, \tag{6.1}$$

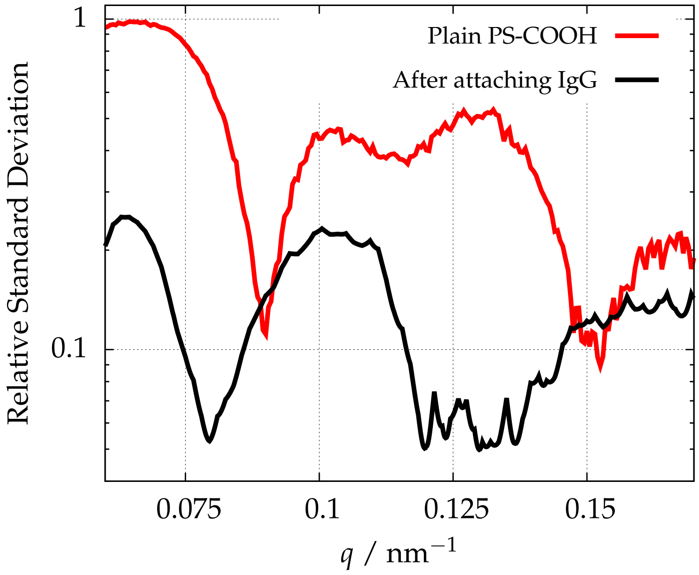

Figure 6.17 | Isoscattering point position before and after attaching IgG (4 mg mL^{-1}) to the PS-COOH particles. A shift of the first minimum to lower q-values is observed after attaching the biotarget to the nanoparticle.

where $\kappa = 4.493$, t is the IgG-shell thickness and R and R_{IgG} are the particle radii before and after IgG incubation. This results in a shell thickness of (7 ± 8) nm, where the uncertainty associated to the thickness (δt) is derived from the expression 6.1 as:

$$\delta t^2 = \left(\frac{\kappa}{\left(q^{\star}_{\mathrm{IgG}}\right)^2} \cdot \delta q^{\star}_{\mathrm{IgG}} \right)^2 + \left(\frac{\kappa}{\left(q^{\star}\right)^2} \cdot \delta q^{\star} \right)^2 \tag{6.2}$$

where $\delta q^{\star}_{\mathrm{IgG}} = 0.011\ \mathrm{nm}^{-1}$ and $\delta q^{\star} = 0.006\ \mathrm{nm}^{-1}$ arise from the diffuseness of the isoscattering point position. This large uncertainty is mainly explained by the low concentration of coated particles in suspension due to the IgG-incubation process. The decreased scattering contribution of the particles in comparison to the medium limits the signal-to-noise ratio and thus the accuracy of the isoscattering point determination. Besides, the use of sucrose in the solution might disturb the solvation shell around the particles and vary the hydration properties of the protein-corona. Such an effect is difficult to detect though it can affect strongly the scattering curves when the electron density of the medium and the probed particle are similar.

Although the relative uncertainty associated to the shell thickness is > 100 %, it is important to highlight that t corresponds to the volume inaccessible for the solvent and, thus, it can be identified with the hard protein corona surrounding the polymeric nanoparticle, i.e. the impermeable part of the IgG shell. Nevertheless, the large associated uncertainty suggests that this technique is inappropriate for the accurate determination of the thickness of a hard protein corona.

7

Summary

This thesis demonstrates how continuous contrast variation in small-angle X-ray scattering (SAXS) by means of a density gradient capillary emerges as a powerful characterization technique for low-density nanoparticles. The technique has proven efficient on a great variety of systems relevant to nanomedicine such as polymeric nanocarriers, the PEGylated liposomal nano-drug Caelyx, empty liposomal nanocarriers and human lipoproteins. The possibility to collect an extensive data set of scattering curves in a short timespan and the ability to tune the contrast range during the experiment arise as clear advantages of the method. The scattering data acquired with this newly introduced technique has been analysed with complementary approaches to reveal a consistent insight into the size distribution and the inner structure of the suspended nanoparticles, resulting in the determination of the size and density of the nanoparticles in a traceable way.

The application of the continuous contrast variation technique in SAXS to characterize low-density polymeric nanoparticles has been thoroughly reviewed in chapter 4. Up to three different evaluation approaches were employed to determine the size of the PS-COOH nanoparticles. By using a model-free analysis of the experimental data based on the isoscattering point theory, an average particle diameter of (100.6 ± 5.6) nm was obtained, which was in very good agreement with the value obtained from a core-shell model fit of (99.4 ± 5.6) nm.

The scope of the continuous contrast variation method as a sizing technique was revealed in chapter 5 by the consistency of the results of the PS-Plain particles obtained with different evaluation approaches and techniques, like atomic force microscopy (AFM), differential centrifugal sedimentation (DCS) and transmission scanning electron microscopy (TSEM). Furthermore, different evaluation approaches to contrast variation SAXS data are examined in detail. The model-free isoscattering point framework is found to be of easy use and very appropriate for the size determination of spherical and quite monodisperse colloids. On the other hand, the calculation of the shape scattering function arises as a precise sizing technique which can additionally provide an insight into the particle shape, although a high number of measurements with different contrasts and an accurate calibration of the system are required.

Due to the high sensitivity of SAXS to small electron density differences in the colloid morphology, information about the heterogeneous composition of the particles can be retrieved. For instance, the analysis of the Guinier region of the scattering curves performed in section 4.3.3 showed that the radial inner structure of the PS-COOH particles consisted of a thin, more dense layer coating the polystyrene core. Complementing these results, the form factor fit presented in section 4.3.1 revealed that the core component of the particle had exactly the same electron density expected for polystyrene and the shell was composed of a compound with a density below that of PMMA. This observation is of paramount importance in polymeric particle characterization because the direct observation by imaging techniques is inadequate for this purpose. In fact, the detection of core-shell structures in polymeric colloids appears as essential for understanding the possible processes occurring during the formation of the particle, e.g. the consequences of emulsion polymerization synthesis or the segregation of components due to their different hydrophobicity.

Besides, a high accuracy in the density information is achieved with the density gradient technique and extends along a rather large density range of polymers as shown in chapter 5. For instance, SAXS measurements of the density of three different polymeric colloids are in excellent agreement with those performed by DCS, a technique extensively used in nanoparticle characterization. As reviewed in section 4.3, the determination of the average electron density of the particle by different evaluation approaches proves the continuous contrast variation technique as a useful tool and an alternative to other techniques like analytical ultracentrifugation, isopycnic centrifugation or field-flow fractionation.

At this point, the performance of the continuous contrast variation in SAXS for the simultaneous size and density determination of low-density polymeric nanoparticles has been successfully proven. The technique has evident advantages in comparison to other contrast variation techniques in small-angle scattering like deuterated small-angle neutron scattering (SANS) or anomalous SAXS (ASAXS), but certain limitations do also arise, namely its restriction to low-density nanomaterials due to the relatively low electron densities achievable with standard contrast agents. Nevertheless, the importance of the technique has been justified with its application to multiple nanomaterials relevant to research fields like medicine or biology in chapter 6.

In the case of the nano-drug Caelyx, a liposomal formulation of doxorubicin coated with polyethylene glycol (PEG), the position of the isoscattering point was measured by means of an iso-osmolal density gradient whereby the size of the liposomal drug was determined with this model-free approach. Supplemented by the model fitting of the shape scattering function of the liposomes, the size was also obtained from an independent evaluation procedure and an average diameter of (67 ± 5) nm was determined. This size is smaller than the value measured by dynamic light scattering (DLS), which can be attributed to the fact that the contrast variation SAXS determines the size of the liposomes impermeable to the contrast agent, i.e. the outer PEG layer of the liposomes is not probed. This demonstrates that the combination of SAXS with DLS can reveal the difference between the hydrodynamic diameter and the "core" size of the nanocarrier, which is related to the thickness of the PEG-layer in case of the stealth liposomes. Moreover it is shown that by means of the shape scattering function fitting, complementary information about the shape of the nanocarrier can be obtained. Additionally, it was found that the average electron density of the liposomal doxorubicin was higher than that of the empty PEGylated liposomes.

Using an aqueous sucrose density gradient, it was possible to study the behaviour of the liposomal drug carrier under different osmotic conditions. It was shown that an increasing osmolality of the buffer produces an osmotic shrinkage of the liposomal structure, although this structural deformation is reversible and does not affect the crystalline structure of the intraliposomal doxorubicin. For comparison purposes with the liposomal doxorubicin system, the osmotic activity of empty liposomes was also investigated using aqueous sucrose. The distinguishable osmotic effects observed in PEGylated and plain liposomes arise from the different formation of the liposomes, which is influenced by the presence of PEG moieties in the preparation. The creation of multilamellar domains in the phospholipid layer was evaluated and the role of the PEG moieties in the membrane resilience was also investigated. The multilamellar structure of the plain liposomes shows higher resilience against osmotic pressure than the unilamellar membrane of the PEGylated vesicles. In the latter, the unilamellar vesicle shrinks due to the osmotic pressure and deforms the liposomes into obloid ellipsoids, creating a bilamellar structure at the outest part of the vesicles.

The continuous contrast variation technique was also used to determine the most distinctive traits of human lipoproteins: size and density, while the application of the technique on nanoparticles incubated in different concentrations of Immunoglobulin G (IgG) revealed that the large uncertainty associated to the diffuseness of the isoscattering points makes the contrast variation approach inappropriate for the accurate and traceable determination of the protein-shell thickness. Nevertheless, the use of complementary techniques such as SAXS, DLS and DCS shows an increase of the protein-corona thickness with increasing concentration of the proteins during incubation as expected.

The work presented in this thesis proves that the recently developed continuous contrast variation technique in SAXS extends the possibilities of the classic solvent contrast variation approach to unexpected new heights. The use of a density gradient capillary results in a virtually continuous range of available solvent electron densities and opens up new perspectives in the characterization of low-density nanoparticles in suspension.

Bibliography

ALS-NIELSEN, J. & MCMORROW, D. 2011 *Elements of Modern X-Ray Physics*, 2nd edn. Hoboken, New Jersey: Wiley.

AMENITSCH, H., BERNSTORFF, S., KRIECHBAUM, M., LOMBARDO, D., MIO, H., RAPPOLT, M. & LAGGNER, P. 1997 Performance and first results of the ELETTRA high-flux beamline for small-angle X-ray scattering. *J Appl Crystallogr* **30**, 872–876.

ARAKI, T., ADE, H., STUBBS, J. M., SUNDBERG, D. C., MITCHELL, G. E., KORTRIGHT, J. B. & KILCOYNE, A. L. D. 2006 Resonant soft x-ray scattering from structured polymer nanoparticles. *Appl Phys Lett* **89**, 124106.

ASSMANN, G. & BREWER, H. B. 1974 Lipid-protein interactions in high density lipoproteins. *PNAS* **71**, 989–993.

AVDEEV, M. V. 2007 Contrast variation in small-angle scattering experiments on polydisperse and superparamagnetic systems: Basic functions approach. *J Appl Crystallogr* **40**, 56–70.

BAKKER, R. 1999 Status and commissioning-results of BESSY II. In *Proceedings of the 1999 Particle Accelerator Conference*, pp. 197–199. IEEE.

BAKKER, R., KRÄMER, D., KUSKE, B., KUSKE, P., MÜLLER, R. & WEIHRETER, E. 1998 Orbit response measurements in the commissioning of the BESSY II booster synchrotron and storage ring. In *Proceedings of the 6th European Particle Accelerator Conference*, pp. 900–902. IOP.

BALLAUFF, M. 2001 SAXS and SANS studies of polymer colloids. *Curr Opin Colloid Interface Sci* **6**, 132–139.

BALLAUFF, M. 2011 Analysis of polymer colloids by small-angle X-ray and neutron scattering: Contrast variation. *Adv Eng Mater* **13**, 793–802.

BALLAUFF, M., BOLZE, J., DINGENOUTS, N., HICKL, P. & PÖTSCHKE, D. 1996 Small-angle X-ray scattering on latexes. *Macromol Chem Phys* **197**, 3043–3066.

BARBER, P. W. & WANG, D.-S. 1978 Rayleigh-Gans-Debye applicability to scattering by nonspherical particles. *Appl Optics* **17**, 797–803.

BARENHOLZ, Y. C. 2001 Liposome application: Problems and prospects. *Curr Opin Colloid Interface Sci* **6**, 66–77.

BARENHOLZ, Y. C. 2012 Doxil®-The first FDA-approved nano-drug: Lessons learned. *J Control Release* **160**, 117–134.

BAUMSTARK, M. W., KREUTZ, W., BERG, A., FREY, I. & KEUL, J. 1990 Structure of human low-density lipoprotein subfractions determined by X-ray small-angle scattering. *BBA-Protein Struct M* **1037**, 48–57.

BEIJA, M., SALVAYRE, R., LAUTH-DE VIGUERIE, N. & MARTY, J.-D. 2012 Colloidal systems for drug delivery: From design to therapy. *Trends Biotechnol* **30**, 485–496.

BELL, N. C., MINELLI, C., TOMPKINS, J., STEVENS, M. M. & SHARD, A. G. 2012 Emerging techniques for submicrometer particle sizing applied to Stöber silica. *Langmuir* **28**, 10860–10872.

BERBERAN-SANTOS, M. N., BODUNOV, E. N. & POGLIANI, L. 1997 On the barometric formula. *Am J Phys* **65**, 404–412.

VAN BEURTEN, P. & VRIJ, A. 1981 Polydispersity effects in the small-angle scattering of concentrated solutions of colloidal spheres. *J Chem Phys* **74**, 2744–2748.

BEYER, D., LEBEK, W., HERGETH, W.-D. & SCHMUTZLER, K. 1990 SAXS study of core-shell colloids. *Colloid Polym Sci* **268**, 744–748.

BLANTON, T. N., HUANG, T. C., TORAYA, H., HUBBARD, C. R., ROBIE, S. B., LOUËR, D., GÖBEL, H. E., WILL, G., GILLES, R. & RAFTERY, T. 1995 JCPDS—International Centre for Diffraction Data round robin study of silver behenate. A possible low-angle X-ray diffraction calibration standard. *Powder Diffr* **10**, 91–95.

BLUMENTHAL, G. R. & GOULD, R. J. 1970 Bremsstrahlung, synchrotron radiation, and Compton scattering of high-energy electrons traversing dilute gases. *Rev Mod Phys* **42**, 237–270.

BOLZE, J., BALLAUFF, M., KIJLSTRA, J. & RUDHARDT, D. 2003 Application of small-angle X-ray scattering as a tool for the structural analysis of industrial polymer dispersions. *Macromol Mater Eng* **288**, 495–502.

BOLZE, J., BALLAUFF, M., RISCHE, T., RUDHARDT, D. & MEIXNER, J. 2004 In situ structural characterization of semi-crystalline polymer latex particles by small-angle X-ray scattering. *Macromol Chem Phys* **205**, 165–172.

BOLZE, J., HÖRNER, K. D. & BALLAUFF, M. 1997 Small-angle X-ray scattering analysis of the radial structure of latex particles swollen by a nonpolar monomer. *Langmuir* **13**, 2960–2964.

BOUWSTRA, J. A., GOORIS, G. S., BRAS, W. & TALSMA, H. 1993 Small angle X-ray scattering: Possibilities and limitations in characterization of vesicles. *Chem Phys Lipids* **64**, 83–98.

BRZUSTOWICZ, M. R. & BRUNGER, A. T. 2005 X-ray scattering from unilamellar lipid vesicles. *J Appl Crystallogr* **38**, 126–131.

CABRAL, H. & KATAOKA, K. 2014 Progress of drug-loaded polymeric micelles into clinical studies. *J Control Release* **190**, 465–476.

CALDWELL, K. D., JONES, H. K. & GIDDINGS, J. C. 1986 Measurement of the size and density of colloidal particles by combining sedimentation field-flow fractionation and quasi-elastic light scattering. *Colloid Surface* **18**, 123–131.

CANELAS, D. A., HERLIHY, K. P. & DESIMONE, J. M. 2009 Top-down particle fabrication: Control of size and shape for diagnostic imaging and drug delivery. *Wiley Interdiscip Rev Nanomed Nanobiotechnol* **1**, 391–404.

CARNEY, R. P., KIM, J. Y., QIAN, H., JIN, R., MEHENNI, H., STELLACCI, F. & BAKR, O. M. 2011 Determination of nanoparticle size distribution together with density or molecular weight by 2D analytical ultracentrifugation. *Nat Commun* **2**, 335.

CASALS, E., PFALLER, T., DUSCHL, A., OOSTINGH, G. J. & PUNTES, V. 2010 Time evolution of the nanoparticle protein corona. *ACS Nano* **4**, 3623–3632.

CASTORPH, S., RIEDEL, D., ARLETH, L., SZTUCKI, M., JAHN, R., HOLT, M. & SALDITT, T. 2010 Structure parameters of synaptic vesicles quantified by small-angle x-ray scattering. *Biophys J* **98**, 1200–1208.

CEDERVALL, T., LYNCH, I., LINDMAN, S., BERGGÅRD, T., THULIN, E., NILSSON, H., DAWSON, K. A. & LINSE, S. 2007 Understanding the nanoparticle–protein corona using methods to quantify exchange rates and affinities of proteins for nanoparticles. *PNAS* **104**, 2050–2055.

CHU, B. & HSIAO, B. S. 2001 Small-angle X-ray scattering of polymers. *Chem Rev* **101**, 1727–1762.

COLHOUN, H. M., OTVOS, J. D., RUBENS, M. B., TASKINEN, M. R., UNDERWOOD, S. R. & FULLER, J. H. 2002 Lipoprotein subclasses and particle sizes and their relationship with coronary artery calcification in men and women with and without type 1 diabetes. *Diabetes* **51**, 1949–1956.

COOMBS, S. H. 1981 A density-gradient column for determining the specific gravity of fish eggs, with particular reference to eggs of the mackerel Scomber scombrus. *Mar Biol* **63**, 101–106.

COUPRIE, M.-E. & FILHOL, J.-M. 2008 X radiation sources based on accelerators. *C R Physique* **9**, 487–506.

COWLEY, J. M. 1995 *Diffraction Physics*, 3rd edn. Amsterdam: North-Holland.

DE GIER, J. 1993 Osmotic behaviour and permeability properties of liposomes. *Chem Phys Lipids* **64**, 187–196.

DE L. KRONIG, R. 1926 On the theory of dispersion of X-rays. *J Opt Soc Am* **12**, 547–557.

DEBYE, P. & BUECHE, A. M. 1949 Scattering by an inhomogeneous solid. *J Appl Phys* **20**, 518–525.

DEMÉ, B., DUBOIS, M., GULIK-KRZYWICKI, T. & ZEMB, T. 2002 Giant collective fluctuations of charged membranes at the lamellar-to-vesicle unbinding transition. 1. Characterization of a new lipid morphology by SANS, SAXS, and electron microscopy. *Langmuir* **18**, 997–1004.

DINGENOUTS, N., BOLZE, J., PÖTSCHKE, D. & BALLAUFF, M. 1999 Analysis of polymer latexes by small-angle X-ray scattering. In *Polymer Latexes-Epoxide Resins-Polyampholytes*, pp. 1–47. Berlin: Springer Verlag.

DINGENOUTS, N., KIM, Y. S. & BALLAUFF, M. 1994*a* The interface between immiscible polymers in composite latexes: A small-angle X-ray scattering study employing contrast variation. *Colloid Polym Sci* **272**, 1380–1387.

DINGENOUTS, N., KIM, Y.-S. & BALLAUFF, M. 1994*b* Radial density distribution in core-shell latexes as revealed by small-angle X-ray scattering. *Macromol Rapid Comm* **15**, 613–617.

DINGENOUTS, N., PULINA, T. & BALLAUFF, M. 1994*c* Structure of carboxylated latices as revealed by small-angle X-ray scattering. *Macromolecules* **27**, 6133–6136.

DOSHI, N. & MITRAGOTRI, S. 2009 Designer biomaterials for nanomedicine. *Adv Funct Mater* **19**, 3843–3854.

DREON, D. M., FERNSTROM, H. A., MILLER, B. & KRAUSS, R. M. 1994 Low-density lipoprotein subclass patterns and lipoprotein response to a reduced-fat diet in men. *FASEB J* **8**, 121–126.

EGELHAAF, S. U., WEHRLI, E., MULLER, M., ADRIAN, M. & SCHURTENBERGER, P. 1996 Determination of the size distribution of lecithin liposomes: A comparative study using freeze fracture, cryoelectron microscopy and dynamic light scattering. *J Microsc* **184**, 214–228.

EINSTEIN, A. 1905 Über die von der molekularkinetischen Theorie der Wärme geforderte Bewegung von in ruhenden Flüssigkeiten suspendierten Teilchen. *Ann Phys* **322**, 549–560.

ETHERIDGE, M. L., CAMPBELL, S. A., ERDMAN, A. G., HAYNES, C. L., WOLF, S. M. & MCCULLOUGH, J. 2013 The big picture on nanomedicine: The state of investigational and approved nanomedicine products. *Nanomedicine: NBM* **9**, 1–14.

EULISS, L. E., DUPONT, J. A., GRATTON, S. & DESIMONE, J. 2006 Imparting size, shape, and composition control of materials for nanomedicine. *Chem Soc Rev* **35**, 1095–1104.

FEIGIN, L. A. & SVERGUN, D. I. 1987 *Structure Analysis by Small-Angle X-Ray and Neutron Scattering*. New York: Plenum Press.

FERNANDEZ, R. M., RISKE, K. A., AMARAL, L. Q., ITRI, R. & LAMY, M. T. 2008 Influence of salt on the structure of DMPG studied by SAXS and optical microscopy. *BBA-Biomembranes* **1778**, 907–916.

FIELDING, L. A., MYKHAYLYK, O. O., ARMES, S. P., FOWLER, P. W., MITTAL, V. & FITZPATRICK, S. 2012 Correcting for a density distribution: Particle size analysis of core–shell nanocomposite particles using disk centrifuge photosedimentometry. *Langmuir* **28**, 2536–2544.

FITZPATRICK, S. T. 1998 Structure and method for centrifugal sedimentation particle size analysis of particles of lower density than their suspension medium (US5786898 A).

GABIZON, A. & MARTIN, F. 1997 Polyethylene glycol-coated (pegylated) liposomal doxorubicin. Rationale for use in solid tumours. *Drugs* **54 Suppl 4**, 15–21.

GARCIA-DIEZ, R., GOLLWITZER, C. & KRUMREY, M. 2015 Nanoparticle characterization by continuous contrast variation in small-angle X-ray scattering with a solvent density gradient. *J Appl Crystallogr* **48**, 20–28.

GARCIA-DIEZ, R., GOLLWITZER, C., KRUMREY, M. & VARGA, Z. 2016*a* Size determination of a liposomal drug by small-angle X-ray scattering using continuous contrast variation. *Langmuir* **32**, 772–778.

GARCIA-DIEZ, R., SIKORA, A., GOLLWITZER, C., MINELLI, C. & KRUMREY, M. 2016*b* Simultaneous size and density determination of polymeric colloids by continuous contrast variation in small angle X-ray scattering. *Eur Polym J* **81**, 641–649.

GARDNER, C., FORTMANN, S. & KRAUSS, R. 1996 Association of small low-density lipoprotein particles with the incidence of coronary artery disease in men and women. *JAMA* **276**, 875–881.

GERMAN, J. B., SMILOWITZ, J. T. & ZIVKOVIC, A. M. 2006 Lipoproteins: When size really matters. *Curr Opin Colloid Interface Sci* **11**, 171–183.

GESSNER, A., LIESKE, A., PAULKE, B.-R. & MÜLLER, R. H. 2003 Functional groups on polystyrene model nanoparticles: Influence on protein adsorption. *J Biomed Mater Res* **65**, 319–326.

GIDDINGS, J. C., KARAISKAKIS, G. & CALDWELL, K. D. 1981 Density and particle size of colloidal materials measured by carrier density variations in sedimentation of Field-Flow Fractionation. *Separ Sci Technol* **16**, 607–618.

GLATTER, O. & KRATKY, O. 1982 *Small Angle x-Ray Scattering*. London: Academic Press.

GLEBER, G., CIBIK, L., HAAS, S., HOELL, A., MÜLLER, P. & KRUMREY, M. 2010 Traceable size determination of PMMA nanoparticles based on Small Angle X-ray Scattering (SAXS). *J Phys Conf Ser* **247**, 012027.

GOERIGK, G., HAUBOLD, H.-G., LYON, O. & SIMON, J.-P. 2003 Anomalous small-angle X-ray scattering in materials science. *J Appl Crystallogr* **36**, 425–429.

GOLLWITZER, C. & KRUMREY, M. 2014 A diffraction effect in X-ray area detectors. *J Appl Crystallogr* **47**, 378–383.

GRUNDER, R., KIM, Y. S., BALLAUFF, M., KRANZ, D. & MÜLLER, H.-G. 1991 Analysis of polymer latices by small-angle X-ray scattering. *Angew Chem Int Edit* **30**, 1650–1652.

GRUNDER, R., URBAN, G. & BALLAUFF, M. 1993 Small-angle x-ray analysis of latex particles with core-shell morphology. *Colloid Polym Sci* **271**, 563–572.

GUINIER, A. 1937 Dispositif permettant d'obtenir des diagrammes de diffraction de poudres cristallines tres intenses avec un rayonnement monochromatique. *Compt Rend Hebd Seances Acad Sciences* **204**, 1115–1116.

GUINIER, A. 1939 Diffraction of X-rays of very small angles-application to the study of ultramicroscopic phenomena. *Ann Phys (Paris)* **12**, 161–237.

GUINIER, A. 1950 Study of catalysts by scattering of X-rays at small angles. *Discuss Faraday Soc* **8**, 344–347.

GUINIER, A. & FOURNET, G. 1955 *Small-Angle Scattering of X-Rays*. New York: Wiley.

GUTERRES, S. S., ALVES, M. P. & POHLMANN, A. R. 2007 Polymeric nanoparticles, nanospheres and nanocapsules for cutaneous applications. *Drug Target Insights* **2**, 147–157.

HALLETT, F. R., WATTON, J. & KRYGSMAN, P. 1991 Vesicle sizing. *Biophys J* **59**, 357–362.

HARRIS, J. M. & CHESS, R. B. 2003 Effect of pegylation on pharmaceuticals. *Nat Rev Drug Discov* **2**, 214–221.

HAVEL, R. J., EDER, H. A. & BRAGDON, J. H. 1955 The distribution and chemical composition of ultracentrifugally separated lipoproteins in serum. *J Clin Invest* **34**, 1345–1353.

HAYNES, W. M. 2012 *CRC Handbook of Chemistry and Physics*, 93rd edn. Philadelphia: Taylor & Francis Ltd.

HELLSING, M. S., RENNIE, A. R., HEENAN, R. K. & ROGERS, S. E. 2012 Structure of a large colloidal crystal–controlling orientation and three-dimensional order. *RSC Adv* **2**, 7091–7098.

HENKE, B., GULLIKSON, E. & DAVIS, J. 1993 X-ray interactions: Photoabsorption, scattering, transmission and reflection at E = 50-30000 eV, Z = 1-92. *Atom Data Nucl Data* **54**, 181–342.

HINTON, R. J. & DOBROTA, M. 1978 *Density Gradient Centrifugation*, *Laboratory techniques in biochemistry and molecular biology*, vol. 1. Amsterdam: North-Holland.

HIRAI, M., IWASE, H., HAYAKAWA, T., KOIZUMI, M. & TAKAHASHI, H. 2003 Determination of asymmetric structure of ganglioside-DPPC mixed vesicle using SANS, SAXS, and DLS. *Biophys J* **85**, 1600–1610.

HOO, C. M., STAROSTIN, N., WEST, P. & MECARTNEY, M. L. 2008 A comparison of AFM and DLS methods to characterize nanoparticle size distributions. *J Nanopart Res* **10**, 89–96.

HUANG, T. C., TORAYA, H., BLANTON, T. N. & WU, Y. 1993 X-ray powder diffraction analysis of silver behenate, a possible low-angle diffraction standard. *J Appl Crystallogr* **26**, 180–184.

HUBBELL, J. H., SELTZER, S. M. & NIST 1996 Tables of X-ray mass attenuation coefficients and mass energy-absorption coefficients 1 keV to 20 MeV for elements Z=1 to 92 and 48 additional substances of dosimetric interest. *Tech. Rep.*. National Institute of Standards and Technology, Gaithersburg.

VAN DE HULST, H. C. 1957 *Light Scattering by Small Particles*. New York: Wiley.

JANS, H., LIU, X., AUSTIN, L., MAES, G. & HUO, Q. 2009 Dynamic light scattering as a powerful tool for gold nanoparticle bioconjugation and biomolecular binding studies. *Anal Chem* **81**, 9425–9432.

JOENSSON, J. E. L., HASSANDER, H., JANSSON, L. H. & TOERNELL, B. 1991 Morphology of two-phase polystyrene/poly(methyl methacrylate) latex particles prepared under different polymerization conditions. *Macromolecules* **24**, 126–131.

JOUSMA, H., TALSMA, H., SPIES, F., JOOSTEN, J. G. H., JUNGINGER, H. E. & CROMMELIN, D. J. A. 1987 Characterization of liposomes. The influence of extrusion of multilamellar vesicles through polycarbonate membranes on particle size, particle size distribution and number of bilayers. *Int J Pharm* **35**, 263–274.

KAMITI, M., BOLDRIDGE, D., NDOPING, L. M. & REMSEN, E. E. 2012 Simultaneous absolute determination of particle size and effective density of submicron colloids by disc centrifuge photosedimentometry. *Anal Chem* **84**, 10526–10530.

KATTAN, J., DROZ, J.-P., COUVREUR, P., MARINO, J.-P., BOUTAN-LAROZE, A., ROUGIER, P., BRAULT, P., VRANCKX, H., GROGNET, J.-M., MORGE, X. & SANCHO-GARNIER, H. 1992 Phase I clinical trial and pharmacokinetic evaluation of doxorubicin carried by polyisohexylcyanoacrylate nanoparticles. *Invest New Drugs* **10**, 191–199.

KAWAGUCHI, T. 1993 The isoscattering point in X-ray scattering curves of globular solute particles measured by the contrast-variation method: The influence of additive penetration into the solute particles. *J Appl Crystallogr* **26**, 214–218.

KAWAGUCHI, T. 2004 Application of isoscattering points to the analysis of globular solute structures. *Crystallogr Rev* **10**, 233–246.

KAWAGUCHI, T. & HAMANAKA, T. 1992 The isoscattering point in X-ray scattering curves of globular solute particles measured by the contrast-variation method. *J Appl Crystallogr* **25**, 778–784.

KAWAGUCHI, T., HAMANAKA, T. & MITSUI, T. 1983 X-ray structural studies of some nonionic detergent micelles. *J Colloid Interf Sci* **96**, 437–453.

KENWORTHY, A. K., HRISTOVA, K., NEEDHAM, D. & MCINTOSH, T. J. 1995 Range and magnitude of the steric pressure between bilayers containing phospholipids with covalently attached poly(ethylene glycol). *Biophys J* **68**, 1921–1936.

KHORASANI, A. A., WEAVER, J. L. & SALVADOR-MORALES, C. 2014 Closing the gap: Accelerating the translational process in nanomedicine by proposing standardized characterization techniques. *Int J Nanomedicine* **9**, 5729–5751.

KISELEV, M. A., LESIEUR, P., KISSELEV, A. M., LOMBARDO, D., KILLANY, M. & LESIEUR, S. 2001*a* Sucrose solutions as prospective medium to study the vesicle structure: SAXS and SANS study. *J Alloy Compd* **328**, 71–76.

KISELEV, M. A., LESIEUR, P., KISSELEV, A. M., LOMBARDO, D., KILLANY, M., LESIEUR, S. & OLLIVON, M. 2001*b* A sucrose solutions application to the study of model biological membranes. *Nucl Instrum Meth A* **470**, 409–416.

KISELEV, M. A., WARTEWIG, S., JANICH, M., LESIEUR, P., KISELEV, A. M., OLLIVON, M. & NEUBERT, R. 2003 Does sucrose influence the properties of DMPC vesicles? *Chem Phys Lipids* **123**, 31–44.

KITTEL, C. 2004 *Introduction to Solid State Physics*, 8th edn. Hoboken, NJ: John Wiley and Sons Ltd.

KLEIN, R., THORNAGEL, R. & ULM, G. 2014 Die Elektronenspeicherringe MLS und BESSY II als primäre Strahlernormale. *PTB-Mitteilungen* **124**, 7–15.

KRAMERS, H. A. 1927 La diffusion de la lumiere par les atomes. *Atti Congr Intern Fisici* **2**, 545–557.

KRATKY, O. 1938 Die Berechnung der Mizelldimensionen von Faserstoffen aus den unter kleinsten Winkeln abgebeugten Interferenzen. *Naturwissenschaften* **26**, 94–94.

KRATKY, O., PILZ, I. & SCHMITZ, P. J. 1966 Absolute intensity measurement of small angle x-ray scattering by means of a standard sample. *J Colloid Interf Sci* **21**, 24–34.

KRATKY, O. & POROD, G. 1949 Diffuse small-angle scattering of X-rays in colloid systems. *J Colloid Sci* **4**, 35–70.

KRATKY, O. & SEKORA, A. 1943 Bestimmung von Form und Größe gelöster Teilchen aus den unter kleinsten Winkeln diffus abgebeugten Röntgenstrahlen. *Naturwissenschaften* **31**, 46–47.

KRISHNAMURTI, P. 1930*a* Studies in X-ray diffraction-Part I: The structure of amorphous carbon. *Indian J Phys* **5**, 473–488.

KRISHNAMURTI, P. 1930*b* Studies in X-ray diffraction-Part II: Some colloidal solutions and liquid mixtures. *Indian J Phys* **5**, 489–499.

KRUMREY, M. 1998 Design of a Four-Crystal Monochromator beamline for radiometry at BESSY II. *J Synchrotron Radiat* **5**, 6–9.

KRUMREY, M., GLEBER, G., SCHOLZE, F. & WERNECKE, J. 2011 Synchrotron radiation-based x-ray reflection and scattering techniques for dimensional nanometrology. *Meas Sci Technol* **22**, 094032.

KRUMREY, M. & ULM, G. 2001 High-accuracy detector calibration at the PTB four-crystal monochromator beamline. *Nucl Instrum Meth A* **467–468**, 1175–1178.

KUČERKA, N., TRISTRAM-NAGLE, S. & NAGLE, J. F. 2006 Structure of fully hydrated fluid phase lipid bilayers with monounsaturated chains. *J Membrane Biol* **208**, 193–202.

KUSAKA, T., NAKAYAMA, M., NAKAMURA, K., ISHIMIYA, M., FURUSAWA, E. & OGASAWARA, K. 2014 Effect of silica particle size on macrophage inflammatory responses. *PLoS ONE* **9**, e92634.

LAGES, S., GOERIGK, G. & HUBER, K. 2013 SAXS and ASAXS on dilute sodium polyacrylate chains decorated with lead ions. *Macromolecules* **46**, 3570–3580.

LAGGNER, P., DEGOVICS, G., MÜLLER, K. W., GLATTER, O., KRATKY, O., KOSTNER, G. & HOLASEK, A. 1977 Molecular packing and fluidity of lipids in human serum low density lipoproteins. *Hoppe-Seyler's Z Physiol Chem* **358**, 771–778.

LASIC, D. D., FREDERIK, P. M., STUART, M. C. A., BARENHOLZ, Y. & MCINTOSH, T. J. 1992 Gelation of liposome interior A novel method for drug encapsulation. *FEBS Lett* **312**, 255–258.

LEE, H. & PASTOR, R. W. 2011 Coarse-grained model for PEGylated lipids: Effect of PEGylation on the size and shape of self-assembled structures. *J Phys Chem B* **115**, 7830–7837.

LEFEBVRE, M., KEELER, R. K., SOBIE, R. & WHITE, J. 2000 Propagation of errors for matrix inversion. *Nucl Instrum Meth A* **451**, 520–528.

LEONARD JR, B. R., ANDEREGG, J. W., KAESBERG, P. & BEEMAN, W. W. 1952 The size of latex particles by X-ray scattering. *J Appl Phys* **23**, 152–152.

LI, X., HIRSH, D. J., CABRAL-LILLY, D., ZIRKEL, A., GRUNER, S. M., JANOFF, A. S. & PERKINS, W. R. 1998 Doxorubicin physical state in solution and inside liposomes loaded via a pH gradient. *BBA-Biomembranes* **1415**, 23–40.

LIANG, X., MAO, G. & NG, K. Y. S. 2005 Effect of chain lengths of PEO–PPO–PEO on small unilamellar liposome morphology and stability: An AFM investigation. *J Colloid Interf Sci* **285**, 360–372.

LIU, X., LU, S., ZHANG, J. & CAO, W. 2006 Thermal decomposition process of silver behenate. *Thermochim Acta* **440**, 1–6.

LUNDQVIST, M., STIGLER, J., ELIA, G., LYNCH, I., CEDERVALL, T. & DAWSON, K. A. 2008 Nanoparticle size and surface properties determine the protein corona with possible implications for biological impacts. *PNAS* **105**, 14265–14270.

LUZZATI, V., TARDIEU, A. & AGGERBECK, L. P. 1979 Structure of serum low-density lipoprotein. *J Mol Biol* **131**, 435–473.

MARR, G. V. 1987 *Handbook on Synchrotron Radiation Vol. 2*. Amsterdam: North-Holland.

MATHAI, J. C., TRISTRAM-NAGLE, S., NAGLE, J. F. & ZEIDEL, M. L. 2008 Structural determinants of water permeability through the lipid membrane. *J Gen Physiol* **131**, 69–76.

MELI, F., KLEIN, T., BUHR, E., FRASE, C. G., GLEBER, G., KRUMREY, M., DUTA, A., DUTA, S., KORPELAINEN, V., BELLOTTI, R., PICOTTO, G. B., BOYD, R. D. & CUENAT, A. 2012 Traceable size determination of nanoparticles, a comparison among European metrology institutes. *Meas Sci Technol* **23**, 125005.

MERTENS, H. D. & SVERGUN, D. I. 2010 Structural characterization of proteins and complexes using small-angle X-ray solution scattering. *J Struc Biol* **172**, 128–141.

MINELLI, C., GARCIA-DIEZ, R., SIKORA, A. E., GOLLWITZER, C., KRUMREY, M. & SHARD, A. G. 2014 Characterization of IgG-protein-coated polymeric nanoparticles using complementary particle sizing techniques. *Surf Interface Anal* **46**, 663–667.

MITCHELL, G. E., LANDES, B. G., LYONS, J., KERN, B. J., DEVON, M. J., KOPRINAROV, I., GULLIKSON, E. M. & KORTRIGHT, J. B. 2006 Molecular bond selective X-ray scattering for nanoscale analysis of soft matter. *Appl Phys Lett* **89**, 044101.

MITCHELL, J. S. & HECKERT, A. B. 2010 The setup, use and efficacy of sodium polytungstate separation methodology with respect to microvertebrate remains. *J Paleontol Techniques* **7**, 1–12.

MITRAGOTRI, S. & LAHANN, J. 2009 Physical approaches to biomaterial design. *Nat Mater* **8**, 15–23.

MONOPOLI, M. P., WALCZYK, D., CAMPBELL, A., ELIA, G., LYNCH, I., BALDELLI BOMBELLI, F. & DAWSON, K. A. 2011 Physical-chemical aspects of protein corona: Relevance to in vitro and in vivo biological impacts of nanoparticles. *J Am Chem Soc* **133**, 2525–2534.

MOTZKUS, F. 1959 Untersuchung kolloider Systeme auf Partikelgrösse und Polydisperität mit Hilfe der Röntgenkleinwinkelstreuung. *Acta Crystallogr* **12**, 773–786.

MÜLLER, K., LAGGNER, P., GLATTER, O. & KOSTNER, G. 1978 The structure of human-plasma Low-Density Lipoprotein B. *Eur J Biochem* **82**, 73–90.

MUNRO, J. M. & COTRAN, R. S. 1988 The pathogenesis of atherosclerosis: Atherogenesis and inflammation. *Lab Invest* **58**, 249–261.

MURPHY, R. M. 1997 Static and dynamic light scattering of biological macromolecules: What can we learn? *Curr Opin Biotech* **8**, 25–30.

MYKHAYLYK, O. O. 2012 Structural characterization of colloidal core-shell polymer-based nanoparticles using small-angle X-ray scattering. In *Proceedings of the International Conference Nanomaterials: Applications and Properties*, p. 01PCN04. Sumy State University.

MYKHAYLYK, O. O., RYAN, A. J., TZOKOVA, N. & WILLIAMS, N. 2007 The application of distance distribution functions to structural analysis of core-shell particles. *J Appl Crystallogr* **40**, s506–s511.

NAGLE, J. F., MATHAI, J. C., ZEIDEL, M. L. & TRISTRAM-NAGLE, S. 2008 Theory of passive permeability through lipid bilayers. *J Gen Physiol* **131**, 77–85.

NEUMANN, A., HOYER, W., WOLFF, M. W., REICHL, U., PFITZNER, A. & ROTH, B. 2013 New method for density determination of nanoparticles using a CPS disc centrifuge. *Colloid Surface B* **104**, 27–31.

NICHOLS, F. S. & FLOWERS, R. G. 1950 Prediction of shrinkage in addition polymerizations. *Ind Eng Chem* **42**, 292–295.

NICOLAS, J., MURA, S., BRAMBILLA, D., MACKIEWICZ, N. & COUVREUR, P. 2013 Design, functionalization strategies and biomedical applications of targeted biodegradable/biocompatible polymer-based nanocarriers for drug delivery. *Chem Soc Rev* **42**, 1147–1235.

NICOLET, A., MELI, F., VAN DER POL, E., YUANA, Y., GOLLWITZER, C., KRUMREY, M., CIZMAR, P., BUHR, E., PÉTRY, J., SEBAIHI, N., DE BOECK, B., FOKKEMA, V., BERGMANS, R. & NIEUWLAND, R. 2016 Inter-laboratory comparison on the size and stability of monodisperse and bimodal synthetic reference particles for standardization of extracellular vesicle measurements. *Meas Sci Technol* **27**, 035701.

NIE, S., XING, Y., KIM, G. J. & SIMONS, J. W. 2007 Nanotechnology applications in cancer. *Annu Rev Biomed Eng* **9**, 257–288.

OLBRICH, K., RAWICZ, W., NEEDHAM, D. & EVANS, E. 2000 Water permeability and mechanical strength of polyunsaturated lipid bilayers. *Biophys J* **79**, 321–327.

OTTEWILL, R. H., COLE, S. J. & WATERS, J. A. 1995 Characterization of particle morphology by scattering techniques. *Macromol Symp* **92**, 97–107.

PABST, G., KUČERKA, N., NIEH, M.-P., RHEINSTÄDTER, M. C. & KATSARAS, J. 2010 Applications of neutron and X-ray scattering to the study of biologically relevant model membranes. *Chem Phys Lipids* **163**, 460–479.

PATEL, T., ZHOU, J., PIEPMEIER, J. M. & SALTZMAN, W. M. 2012 Polymeric nanoparticles for drug delivery to the central nervous system. *Adv Drug Deliver Rev* **64**, 701–705.

PAUW, B. R. 2013 Everything SAXS: Small-angle scattering pattern collection and correction. *J Phys-Condens Mat* **25**, 383201.

PAUW, B. R., PEDERSEN, J. S., TARDIF, S., TAKATA, M. & IVERSEN, B. B. 2013 Improvements and considerations for size distribution retrieval from small-angle scattering data by Monte Carlo methods. *J Appl Crystallogr* **46**, 365–371.

PEDERSEN, J. S. 1994 Determination of size distribution from small-angle scattering data for systems with effective hard-sphere interactions. *J Appl Crystallogr* **27**, 595–608.

PEDERSEN, J. S. 1997 Analysis of small-angle scattering data from colloids and polymer solutions: Modeling and least-squares fitting. *Adv Colloid Interfac* **70**, 171–210.

PÉREZ-HERRERO, E. & FERNÁNDEZ-MEDARDE, A. 2015 Advanced targeted therapies in cancer: Drug nanocarriers, the future of chemotherapy. *Eur J Pharm Biopharm* **93**, 52–79.

PERRET, R. & RULAND, W. 1972 Glassy carbon as standard for the normalization of small-angle scattering intensities. *J Appl Crystallogr* **5**, 116–119.

PETROS, R. A. & DESIMONE, J. M. 2010 Strategies in the design of nanoparticles for therapeutic applications. *Nat Rev Drug Discov* **9**, 615–627.

POWERS, K. W., BROWN, S. C., KRISHNA, V. B., WASDO, S. C., MOUDGIL, B. M. & ROBERTS, S. M. 2006 Research strategies for safety evaluation of nanomaterials Part VI: Characterization of nanoscale particles for toxicological evaluation. *Toxicol Sci* **90**, 296–303.

RHODES, D. & MILES, N. J. 1991 Fine coal characterization. *Miner Eng* **4**, 503–510.

RIBEIRO, A. C. F., ORTONA, O., SIMÕES, S. M. N., SANTOS, C. I. A. V., PRAZERES, P. M. R. A., VALENTE, A. J. M., LOBO, V. M. M. & BURROWS, H. D. 2006 Binary mutual diffusion coefficients of aqueous solutions of sucrose, lactose, glucose and fructose in the temperature range from (298.15 to 328.15) K. *J Chem Eng Data* **51**, 1836–1840.

ROBINSON, A. L. 2015 History of synchrotron radiation. *Synchrotron Radiat News* **28**, 4–9.

ROSEN, H. & ABRIBAT, T. 2005 The rise and rise of drug delivery. *Nat Rev Drug Discov* **4**, 381–385.

ROSENFELDT, S., DINGENOUTS, N., BALLAUFF, M., WERNER, N., VÖGTLE, F. & LINDNER, P. 2002 Distribution of end groups within a dendritic structure: A SANS study including contrast variation. *Macromolecules* **35**, 8098–8105.

SAHOO, S. K. & LABHASETWAR, V. 2003 Nanotech approaches to drug delivery and imaging. *Drug Discov Today* **8**, 1112–1120.

SAKURAGI, M., KOIWAI, K., NAKAMURA, K., MASUNAGA, H., OGAWA, H. & SAKURAI, K. 2011 Transformation from multilamellar to unilamellar vesicles by addition of a cationic lipid to PEGylated liposomes explored with synchrotron small angle X-ray scattering. *J Phys Conf Ser* **272**, 012011.

SCHNABLEGGER, H. & SINGH, Y. 2006 *A Practical Guide to SAXS*. Graz: Anton Paar.

SCHNITZER, E. & LICHTENBERG, D. 1994 Re-evaluation of the structure of low density lipoproteins. *Chem Phys Lipids* **70**, 63–74.

SCHWINGER, J. 1949 On the classical radiation of accelerated electrons. *Phys Rev* **75**, 1912–1925.

SHAFFER, L. B. & HENDRICKS, R. W. 1974 Calibration of polyethylene (lupolen) as a wavelength-independent absolute intensity standard. *J Appl Crystallogr* **7**, 159–163.

SILVERSTEIN, M. S., TALMON, Y. & NARKIS, M. 1989 Microstructure of polyacrylate/polystyrene two-stage latices. *Polymer* **30**, 416–424.

SIM, A. Y. L., LIPFERT, J., HERSCHLAG, D. & DONIACH, S. 2012 Salt dependence of the radius of gyration and flexibility of single-stranded DNA in solution probed by small-angle x-ray scattering. *Phys Rev E* **86**, 021901.

SOU, K., ENDO, T., TAKEOKA, S. & TSUCHIDA, E. 2000 Poly(ethylene glycol)-modification of the phospholipid vesicles by using the spontaneous incorporation of poly(ethylene glycol)-lipid into the vesicles. *Bioconjugate Chem* **11**, 372–379.

SPYRATOU, E., MOURELATOU, E. A., MAKROPOULOU, M. & DEMETZOS, C. 2009 Atomic force microscopy: A tool to study the structure, dynamics and stability of liposomal drug delivery systems. *Expert Opin Drug Deliv* **6**, 305–317.

STUHRMANN, H. B. 1985 Resonance scattering in macromolecular structure research. In *Characterization of Polymers in the Solid State II: Synchrotron Radiation, X-Ray Scattering and Electron Microscopy*, pp. 123–163. Berlin: Springer Verlag.

STUHRMANN, H. B. 2007 Contrast variation in X-ray and neutron scattering. *J Appl Crystallogr* **40**, s23–s27.

STUHRMANN, H. B. 2008 Small-angle scattering and its interplay with crystallography, contrast variation in SAXS and SANS. *Acta Crystallogr A* **64**, 181–191.

STUHRMANN, H. B. & KIRSTE, R. G. 1965 Elimination der intrapartikulären Untergrundstreuung bei der Röntgenkleinwinkelstreuung an kompakten Teilchen (Proteinen). *Z Phys Chem* **46**, 247–250.

STUHRMANN, H. B. & KIRSTE, R. G. 1967 Elimination der intrapartikulären Untergrundstreuung bei der Röntgenkleinwinkelstreuung an kompakten Teilchen. II. *Z Phys Chem* **56**, 334–337.

STUHRMANN, H. B., TARDIEU, A., MATEU, L., SARDET, C., LUZZATI, V., AGGERBECK, L. & SCANU, A. M. 1975 Neutron scattering study of human serum low density lipoprotein. *PNAS* **72**, 2270–2273.

TAKAHASHI, K., KATO, H., SAITO, T., MATSUYAMA, S. & KINUGASA, S. 2008 Precise measurement of the size of nanoparticles by dynamic light scattering with uncertainty analysis. *Part Part Syst Char* **25**, 31–38.

TAO, L., HU, W., LIU, Y., HUANG, G., SUMER, B. D. & GAO, J. 2011 Shape-specific polymeric nanomedicine: Emerging opportunities and challenges. *Exp Biol Med* **236**, 20–29.

TARDIEU, A., MATEU, L., SARDET, C., WEISS, B., LUZZATI, V., AGGERBECK, L. & SCANU, A. M. 1976 Structure of human serum lipoproteins in solution. *J Mol Biol* **101**, 129–153.

TENZER, S., DOCTER, D., KUHAREV, J., MUSYANOVYCH, A., FETZ, V., HECHT, R., SCHLENK, F., FISCHER, D., KIOUPTSI, K., REINHARDT, C., LANDFESTER, K., SCHILD, H., MASKOS, M., KNAUER, S. K. & STAUBER, R. H. 2013 Rapid formation of plasma protein corona critically affects nanoparticle pathophysiology. *Nat Nano* **8**, 772–781.

TERRENO, E., DELLI CASTELLI, D., VIOLANTE, E., SANDERS, H. M., SOMMERDIJK, N. A. & AIME, S. 2009 Osmotically shrunken LIPOCEST agents: An innovative class of magnetic resonance imaging contrast media based on chemical exchange saturation transfer. *Chem Eur J* **15**, 1440–1448.

THORNAGEL, R., KLEIN, R. & ULM, G. 2001 The electron storage ring BESSY II as a primary source standard from the visible to the the X-ray range. *Metrologia* **38**, 385–389.

UEDAIRA, H. & UEDAIRA, H. 1985 Sugar-water interaction from diffusion measurements. *J Solution Chem* **14**, 27–34.

VARGA, Z., BERÉNYI, S., SZOKOL, B., ŐRFI, L., KÉRI, G., PETÁK, I., HOELL, A. & BÓTA, A. 2010 A closer look at the structure of sterically stabilized liposomes: A small-angle X-ray scattering study. *J Phys Chem B* **114**, 6850–6854.

VARGA, Z., WACHA, A. & BÓTA, A. 2014*a* Osmotic shrinkage of sterically stabilized liposomes as revealed by time-resolved small-angle X-ray scattering. *J Appl Crystallogr* **47**, 35–40.

VARGA, Z., WACHA, A., VAINIO, U., GUMMEL, J. & BÓTA, A. 2012 Characterization of the PEG layer of sterically stabilized liposomes: A SAXS study. *Chem Phys Lipids* **165**, 387–392.

VARGA, Z., YUANA, Y., GROOTEMAAT, A. E., VAN DER POL, E., GOLLWITZER, C., KRUMREY, M. & NIEUWLAND, R. 2014*b* Towards traceable size determination of extracellular vesicles. *J Extracell Vesicles* **3**, 23298.

VAUTHIER, C., SCHMIDT, C. & COUVREUR, P. 1999 Measurement of the density of polymeric nanoparticulate drug carriers by isopycnic centrifugation. *J Nanopart Res* **1**, 411–418.

VENDITTO, V. J. & SZOKA JR., F. C. 2013 Cancer nanomedicines: So many papers and so few drugs! *Adv Drug Deliver Rev* **65**, 80–88.

VICENT, M. J. & DUNCAN, R. 2006 Polymer conjugates: Nanosized medicines for treating cancer. *Trends Biotechnol* **24**, 39–47.

VITTAZ, M., BAZILE, D., SPENLEHAUER, G., VERRECCHIA, T., VEILLARD, M., PUISIEUX, F. & LABARRE, D. 1996 Effect of PEO surface density on long-circulating PLA-PEO nanoparticles which are very low complement activators. *Biomaterials* **17**, 1575–1581.

WANG, A. Z., LANGER, R. & FAROKHZAD, O. C. 2012 Nanoparticle delivery of cancer drugs. *Annu Rev Med* **63**, 185–198.

WARREN, B. E. 1934 X-Ray diffraction study of carbon black. *J Chem Phys* **2**, 551–555.

WARREN, B. E. 1969 *X-Ray Diffraction*. New York: Addison-Wesley.

WERNECKE, J., GOLLWITZER, C., MÜLLER, P. & KRUMREY, M. 2014 Characterization of an in-vacuum PILATUS 1M detector. *J Synchrotron Radiat* **21**, 529–536.

WICKLINE, S. A. & LANZA, G. M. 2003 Nanotechnology for molecular imaging and targeted therapy. *Circulation* **107**, 1092–1095.

WOLFRAM, J., SURI, K., YANG, Y., SHEN, J., CELIA, C., FRESTA, M., ZHAO, Y., SHEN, H. & FERRARI, M. 2014 Shrinkage of pegylated and non-pegylated liposomes in serum. *Colloid Surface B* **114**, 294–300.

WU, C.-L., FARKAS, N., DAGATA, J. A., HE, B.-C. & FU, W.-E. 2014 Particle deformation induced by AFM tapping under different setpoint voltages. In *Proceedings SPIE, Scanning Microscopies*, vol. 9236, p. 92360W. SPIE.

YAMAOKA, T., TABATA, Y. & IKADA, Y. 1994 Distribution and tissue uptake of poly(ethylene glycol) with different molecular weights after intravenous administration to mice. *J Pharm Sci* **83**, 601–606.

YANG, F.-S., CALDWELL, K. D. & GIDDINGS, J. C. 1983 Colloid characterization by sedimentation field-flow fractionation: II. Particle-size distribution. *J Colloid Interf Sci* **92**, 81–91.

YANG, Z., HUCK, W. T. S., CLARKE, S. M., TAJBAKHSH, A. R. & TERENTJEV, E. M. 2005 Shape-memory nanoparticles from inherently non-spherical polymer colloids. *Nat Mater* **4**, 486–490.

YEH, M.-K., HSIN-I CHANG & MING-YEN CHENG 2011 Clinical development of liposome based drugs: Formulation, characterization, and therapeutic efficacy. *Int J Nanomedicine* **7**, 49–60.

ZHAO, D., FENG, J., HUO, Q., MELOSH, N., FREDRICKSON, G. H., CHMELKA, B. F. & STUCKY, G. D. 1998 Triblock copolymer syntheses of mesoporous silica with periodic 50 to 300 Angstrom pores. *Science* **279**, 548–552.

ZHOU, X., PORTER, A. L., ROBINSON, D. K. R., SHIM, M. S. & GUO, Y. 2014 Nano-enabled drug delivery: A research profile. *Nanomedicine: NBM* **10**, 889–896.

Acknowledgments

I would like to use this opportunity to thank all the people that have assisted me during these years to reach my goals and have contributed to the conclusion of this thesis. Though I tried to avoid any verbose language during the main text, it will be extremely challenging to remain synthetic when acknowledging the contributions of the following people.

First of all, I would like to thank *Dr. Michael Krumrey*, the leader of the working group Röntgenradiometrie of the Physikalisch-Technische Bundesanstalt (PTB) and the person who provided me the proper human and scientific environment to perform successful experiments and pursue my research interests. Under his leadership, I could concentrate in the relevant aspects of my investigations and focus all my energy into my research.

I am very grateful also to *Prof. Dr. Mathias Richter* for giving me the opportunity to participate on the activity of the PTB in BESSY II and encourage me to chase my scientific goals. His motivation and constructive advices during these years have been really helpful and are highly appreciated.

Prof. Dr. Stefan Eisebitt and *Prof. Dr. Simone Raoux* are also kindly acknowledged for the precious advice given to complete my research work and for the concern to read and prove this written thesis. Their many research interests inspired me to find new alternatives to old scientific problems.

I am greatly indebted to my mentor *Dr. Christian Gollwitzer* for his supervision and honest interest throughout these last 4 years. The valuable scientific expertise he provided me with cannot overshadow the great moments we spent together in the laboratory. Without his support and expert advise, the completion of this thesis would have been virtually impossible.

And also my most sincerely acknowledgement to the whole Arbeitsgruppe 7.11 of PTB, whose individuals have contributed to my work both technically and personally. I am especially thankful to all the engineers who have provided the technical support to perform SAXS experiments in an outstanding way. During these years, the group line-up included *Levent Cibik, Ulf Knoll, Stefanie Langner, Swenja Schreiber, Layla Riemann* and *Peter Müller*.

I don't want to forget the many graduate students and postdocs with whom I have crossed paths in PTB and who have influenced and enhanced my research like *Dr. Jan Wernecke, Analía Fernández Herrero, Anton Haase, Mika Pflüger, Oleksey Mariasov* and *Dr. Victor Soltwisch*.

I am glad to acknowledge also the excellent job that all the members of the Laboratory of the PTB in BESSY II perform day after day as well as the Helmholtz-Zentrum Berlin (HZB) scientists who operate the synchrotron facility. Without the continuous and stable performance of BESSY II, most of the experimental data shown in this thesis could not have been collected.

I am in debt both personally and scientifically with *Dr. Zoltan Varga* from the Institute of Materials and Environmental Chemistry (Research Centre for Natural Sciences, Budapest, Hungary). His expertise in SAXS and liposomal structures is unparalleled and some of the

ideas presented in this thesis derive directly from fruitful discussions with him. Besides he prepared the empty liposomes described in chapter 6 and encouraged me to give Caelyx® a chance.

I want to acknowledge the long-term and rewarding collaboration established with the Surface and Nanoanalysis group of the National Physical Laboratory (Teddington, UK) led by *Dr. Alex Shard*. I want to thank especially *Dr. Caterina Minelli* for sharing her extensive knowledge about polymeric colloids and bio-surfaces and for the preparation of the protein-coated nanoparticles employed in chapter 6 as well as I want to highlight our common interest in characterization techniques for low-density nanoparticles as observed throughout this thesis. I am also very grateful to *Dr. Aneta Sikora* for her predisposition and competence on the DCS measurements presented in chapter 5.

I would like to thank sincerely *Dr. Armin Hoell* from HZB for the continuous collaboration with the HZB SAXS setup, which was used in the majority of experiments presented here. His expertise in (A)SAXS has been inspiring and his knowledge of the SAXS apparatus has proven very beneficial for my research.

I am grateful to *Eike Gericke* from Humboldt Universität Berlin for his interest in new calibration standard materials for SAXS, who brought me in contact with other alternatives to AgBehe. I would like to thank also *Roman Schmack* from Technische Universität Berlin for the synthesis of the SBA-15 sample used in the study of chapter 3.

It is important for me to mention the personal and scientific support given by other HZB colleagues like *Dr. Kaan Atak* and *Dr. Wilson Quevedo*, whose scientific comments shaped this thesis in subtle but vital ways. The proofreading job of Dr. Atak is also very valuable and it is only comparable to the proofreading effort provided by *Dr. Marc Cano-Bret* from the Department of Physics and Astronomy of the Shanghai Jiao Tong University (China), whose long-lasting friendship and motivation pushed me through some difficult moments.

A very special "thank you" to all my physics and non-physics friends in Berlin, *Markus, Alexander, Alessandro, Alisio, Alberto, Fede, Mattia, Donal*, the *Colonos* in Dosrius and the *Margon's 12* crew in Barcelona, who make a good day out of a bad one.

And of course, a warm and honest thanks to my family in general and to my parents and Marta in particular. They have been all the strength that I needed in the darkest moments in Berlin. *Muchas gracias por ser la luz que me ha guíado en los momentos más oscuros*.

Eidesstattliche Versicherung

Hiermit versichere ich an Eides statt, dass ich die vorliegende Arbeit selbstständig verfasst und keine anderen als die in der Dissertation angegebenen Quellen und Hilfsmittel benutzt habe. Alle Ausführungen, die anderen veröffentlichten oder nicht veröffentlichten Schriften wörtlich oder sinngemäß entnommen wurden, habe ich kenntlich gemacht. Die Darstellung des Eigenanteils an bereits publizierten Inhalten in meiner beigefügten Erklärung ist zutreffend.

Es gab keine Zusammenarbeit mit anderen wissenschaftlichen Mitarbeitern, die ein Promotionsverfahren anstreben.

Berlin, November 2017 Raül García Diez

Declaration

The dissertation or parts of it were **previously published**. I attach information on previous publications according to §2 (4) of the *Promotionsordnung* of TU Berlin and regulations of Faculty II.

This is a list of the peer-reviewed publications containing parts of the dissertation and the detailed contributions of the co-authors to each publication:

1. C. MINELLI, R. GARCIA-DIEZ, A. SIKORA, C. GOLLWITZER, M. KRUMREY, A. SHARD, Characterization of IgG-protein-coated polymeric nanoparticles using complementary particle sizing techniques, *Surface and Interface Analysis* **46** 663-667 (2014)

   AS and MK conceived the study in the framework of the BioSurf project. CM and AS collected and analysed the DCS and DLS data. RGD and CG performed the SAXS measurements and RGD evaluated the experimental data. CM drafted the manuscript. All authors read, approved and contributed to the final manuscript.

2. R. GARCIA-DIEZ, C. GOLLWITZER, M. KRUMREY, Nanoparticle characterization by continuous contrast variation in small-angle X-ray scattering with a solvent density gradient, *Journal of Applied Crystallography* **48**, 20-28 (2015)

   RGD, CG and MK designed the study and developed the methodology. RGD and CG performed the measurements. RGD analysed the data and drafted the manuscript. All authors read, approved and contributed to the final manuscript.

3. R. GARCIA-DIEZ, C. GOLLWITZER, M. KRUMREY, Z. VARGA, Size determination of a liposomal drug by small-angle X-ray scattering using continuous contrast variation, *Langmuir* **32 (3)**, 772-778 (2016)

   RGD and ZV designed the study and developed the methodology. RGD, ZV and CG performed the measurements. RGD analysed the data. RGD and ZV drafted the manuscript. All authors read, approved and contributed to the final manuscript.

4. R. GARCIA-DIEZ, A. SIKORA, C. GOLLWITZER, C. MINELLI, M. KRUMREY, Simultaneous size and density determination of polymeric colloids by continuous contrast variation in small angle X-ray scattering, *European Polymer Journal* **81** 641–649 (2016)

   RGD and CM designed the study and developed the methodology. RGD and CG performed the SAXS measurements. CM and AS collected and evaluated the DCS data. RGD analysed the SAXS data and drafted the manuscript. All authors read, approved and contributed to the final manuscript.

Berlin, November 2017 Raül García Diez